The background of the cover is a complex, interconnected network of light blue channels on a grey background, resembling a porous medium or a microfluidic chip. The channels vary in width and form, creating a dense, maze-like pattern.

Bachelor End Project

A New Definition for Capillary Numbers in Microfluidic Models

M. W. Smit

Technische Universiteit Delft

Bachelor End Project

A New Definition for Capillary Numbers in Microfluidic Models

by

M. W. Smit

This report presents the findings of the research into a new definition for capillary numbers in order to better describe the mobilization and desaturation of trapped nonwetting phase in microfluidic models. This report is part of the end project of the bachelor's program of

Applied Earth Sciences

at Delft University of Technology.

To be defended publicly on friday November 3rd, 2017 at 3:00 PM.

Supervisors:	Prof. W. R. Rossen	TU Delft
	Dr. S. Vincent-Bonnieu	Shell TU Delft
	MSc. J. Tang	TU Delft
Thesis Committee:	Dr. K. H. A. A. Wolf	TU Delft

Preface

In this Report, I (Michiel Smit) present the findings of my literature study into the derivation of a new definition for the capillary number to describe the mobilization of residual trapped oil inside microfluidic devices. This research was done as part of my Bachelor's End Project for the Bachelor program Applied Earth Sciences at the Delft University of Technology between September and November 2017. Supervising the progress of my research were Prof. W. R. Rossen, Dr. S. Vincent-Bonnieu and MSc. J. Tang.

Enhanced oil recovery will play an important role in the future, as oil reserves will reduce over time. It then becomes important to mobilize the trapped residual oil inside reservoirs, which can sometimes make up 30 percent of the total reserves in a reservoir. Microfluidic devices play an important role in the research into enhanced oil recovery as they allow visualization of two phase transport inside porous media. The capillary number is an useful tool to analyze the mobilization as it allows to estimate the residual oil saturation. However, until now, there was no equation to visualize the capillary desaturation of a micromodel by a single curve.

This report will present background information on the theory of capillary transport, trapping and mobilization. The new capillary number will be derived based on a force balance on a trapped ganglion inside a pore body of a microfluidic device. Once the equation for the capillary number has been derived, the equation will be tested on a number of microfluidic geometries obtained from published papers. No experiments have been conducted by me; all desaturation data was obtained from literature. The data will be analyzed and conclusions will be made on the functionality of the newly derived capillary number. Also, necessary future experiments will be discussed that need to be performed in order to test the functionality and improve the capillary number.

Early preparations for the project started back in June 2017, when I came into contact with Dr. Vincent-Bonnieu via D. Boersma. I was very interested in finding a subject for my Bachelor's Thesis that would cover real world problems. Enhanced oil recovery fitted the picture perfectly since future oil shortages are inevitable. Dr. Vincent-Bonnieu then introduced me to Prof W. R. Rossen to discuss a fitting subject for my thesis. The subject became the Capillary Numbers For microfluidic devices. Work on the research began in the beginning of September, when Mr. Rossen introduced me to MSc. Jinyu Tang, PhD student at the faculty of Civil Engineering and Geosciences, who helped me in the process of my thesis.

The first two weeks of the eight week period were used by to get myself acquainted with the subjects of capillary transport and trapping as well as the capillary numbers and desaturation. The next step was to derive an equation for the capillary number for microfluidic slits that would allow for a better visualization of the desaturation of nonwetting phases. Answers for this problem were found in the work on model fractures presented by Al Quaimi and Rossen (2017) who used a similar approach. The main difficulty was to test the functionality of the equation. Due to time shortages, it was not possible for me to conduct my own experiments. Instead, existing micromodel data was analyzed. In the end, 9 different models were analyzed, and positive results were obtained, suggesting that the new capillary number actually is better for approximating the desaturation of nonwetting fluids inside microfluidic models. The last week of the eight week period was used to finalize the analysis of the obtained results and finish the report. The final report was submitted to my supervisors and the second corrector of my thesis on October 30th, 2017. A public presentation and defense was held on Friday the 3rd of November, 2017.

*M. W. Smit
Delft, October 2017*

Acknowledgements

This report is written as part of my end project of the Bachelor's program Applied Earth Sciences at the Delft University of Technology. For making this project possible, I wish to especially thank Prof. W. R. (Bill) Rossen, my first supervisor. He proposed the subject to me and along the way came with suggestions to help overcome complicated problems. Also, I would like to thank him for always having time to help me with my project when I came by his office without notice. Secondly, I wish to thank PhD. Jinyu Tang, who became my first contact person to help me with carrying out this research. He always made time for me if I had encountered problems. And thirdly, my thanks to Dr. S. Vincent-Bonnieu. Despite being at the faculty only once per week, we met most of the Fridays to discuss my progress. He helped me by giving good suggestions in order to improve the content of the report. Also, he was the first person that I came in contact with during my search for a subject for my thesis, and he was kind enough to help me out, despite never having met before the start of the project.

Abstract

The mobilization of the trapped residual oil is an important part of Enhanced Oil Recovery. The desaturation of nonwetting fluids from porous media is often described using capillary numbers which are a ratio of viscous forces over the capillary forces between the wetting and the nonwetting fluids. Two-dimensional microfluidic devices (micromodels) play an important role as they allow for the visualization of the two phase flow in porous media. Even though the existing definitions for capillary numbers work fine for describing the mobilization of the trapped nonwetting phase in geological rock, problems arise when applying these definitions for capillary numbers on micromodels. The conventional definition of the capillary numbers do not allow to visualize the desaturation of nonwetting phases in different micromodels on a single trend.

This research presents the derivation of a new definition of a capillary number that can be used to better analyze the mobilization of trapped nonwetting ganglions inside micromodels. The new capillary number is based on a force balance on a trapped ganglion and the corresponding mobilization criteria of the trapped nonwetting phase. The new definition of the capillary number consists of the conventional definition of the capillary number and a geometric term that accounts for the geometry of the micromodel, including the sizes of the pore bodies and throats as well as the ganglion length. The functionality of similar definitions of the capillary number for roughened fractures has previously been published by Al Quaimi and Rossen (2017).

The functionality of the new capillary number has been tested by analyzing published desaturation data for various micromodels, each using different wetting and nonwetting phase combinations using both the conventional and the new definition of the capillary number. It is found that the new definition allows for better analysis of the mobilization of the trapped nonwetting fluid inside micromodels, as the desaturation curves for different models can now be visualized by a single trend. Also, it is suggested that the geometrical parameters of the new equation are more significant for describing the mobilization of the trapped nonwetting phase than the permeability of the medium and the interfacial properties of the wetting and nonwetting phases.

*M. W. Smit
Delft, October 2017*

Contents

List of Figures	xi
List of Tables	xiii
1 Introduction	1
1.1 Scope of Report	2
1.2 Outline of Report	2
2 Capillarity, Trapping and Mobilization	3
2.1 Wettability and Two Phase Flow	3
2.2 Capillary Pressure and Transport	6
2.2.1 Definition of Capillary Pressure	6
2.2.2 Capillary Pressure Curves	7
2.2.3 Hysteresis	10
2.3 Capillary Trapping	11
2.3.1 Pore-Doublet Model	11
2.3.2 Snap-Off Model	13
2.4 Mobilization of the Trapped Nonwetting Phase	14
3 Capillary numbers and capillary desaturation curves	17
3.1 Capillary Numbers	17
3.2 Residual Saturations and Capillary Desaturation Curves	18
4 New Capillary Number for Fractures	21
4.1 Conventional Capillary Number in Fractures	21
4.2 Derivation of New Capillary Number	21
4.3 Experiments and Results	23
4.4 Relationship Between Permeability and Hydraulic Aperture	24
5 Derivation of New Capillary Number in Micromodels	27
5.1 Force Balance on a Trapped Ganglion	27
5.2 Definition of Tortuosity	29
6 Description of Various Micromodels	31
6.1 Simple Geometries by Kawale (2017)	32
6.1.1 Squares, Aligned	33
6.1.2 Squares, Staggered.	33
6.1.3 Circles, Aligned	33
6.1.4 Circles, Staggered	34
6.2 Hexagonal Geometry by Jones (2016).	34
6.3 Geometries by Jeong et al. (2003).	36
6.4 Ibrahim et al. (2008).	38
6.5 Yeganeh et al. (2016)	40
7 Analysis of Microfluidic Flow Data	45
7.1 Artificial Pressure Gradient for models by Kawale and Jones.	45
7.2 Desaturation Data for Conventional Capillary Number	46
7.3 Desaturation for New Definition of Capillary Number	47
7.3.1 Fluid Properties and the New Capillary Number	48
7.4 Relationship Between Permeability and the Geometric Term	49

8 Conclusion	51
9 Discussion	53
10 Recommendations for Future Study	55
Bibliography	57
A Results for Alquaimi and Rossen (2017)	59
B Additional Figures for Micromodels	61
B.1 Simple Geometries by Kawale	61
B.2 Hexagonal Geometry by Jones (2016).	64
B.3 Micromodels of Jeong and Corapcioglu (2003)	65
B.4 Ibrahim et al. (2008).	66
B.5 Yeganeh et al. (2016)	70
C Additional Figures for the Analysis of the Microfluidic Data	71
C.1 Pressure gradient and Residual Saturation	71
C.2 Changing Contact Angle Between Crude Oil and Brine	72
C.3 Permeability and Geometric Terms	73

List of Figures

2.1	Interfacial tensions in a water-oil-solid system (Peters, 2012).	4
2.2	Equilibrium contact angles for four different wettabilities (Peters, 2012).	5
2.3	Fluid distribution as a function of wettability (Peters, 2012).	6
2.4	Immiscible displacement of fluids as a function of wettability on the pore scale, for a strongly water wet medium (above) and a strongly oil wet medium (below) (Peters, 2012).	7
2.5	A capillary tube experiment shows us that if the radius decreases, the capillary pressure increases, causing the interface to raise higher.	8
2.6	Schematic overview of a capillary pressure curve.	9
2.7	Schematic overview for capillary pressure curves for drainage processes in rocks with different pore sizes. curve 1 represents a rock with the largest pore size, and 4 with the smallest.	9
2.8	Sketch of a basic hysteresis curve.	10
2.9	Capillary pressure hysteresis in an idealized pore structure with (a) the structure of the idealized pores and (b) the corresponding capillary pressure curve. Blue is the direction of drainage and red is the direction of imbibition.	11
2.10	Illustration of a pore-doublet model on the left (Lake, 1989), and a schematic overview on how it works in geological rock Peters (2012).	12
2.11	Snap-off model for capillary trapping showing 3 different aspect ratios (Chatzis and Dullien, 1983).	13
2.12	Illustration showing the mobilization of a trapped ganglion of nonwetting fluid in an idealized pore model. The red arrow shows the direction of flow.	14
2.13	Sketches of low number trapping mechanisms and configuration of residual oil in doublets (Chatzis and Dullien, 1983). E is a pore with out trapping, T stands for trapping by Snap-off. S is for a stable interface downstream (no trapping). F means that a downstream node fills. subscript O means that a certain node traps first.	15
3.1	Typical capillary desaturation curve for both wetting and nonwetting residual phase saturations (Lake, 1989).	18
3.2	Capillary pressure curves for different geological rock types. Notice how the range between $N_{ca,c}$ and $N_{ca,t}$ increases as the pore sizes increase (Lake, 1989).	19
4.1	illustration of a fracture and a trapped nonwetting ganglion, greatly exaggerated in the vertical direction. d_t is the throat aperture and d_b is the body aperture (Al Quaimi and Rossen, 2017).	22
4.2	Illustration of a parallel plate model. On the left side, the dimensions and parameters of the model are shown. On the right, the parabolic velocity profile is shown (Zimmermann and Bodvarsson, 1996).	24
5.1	Model of a Microfluidic Device. On the left, the overview and the coordinate system. On the right, the parameters needed for the equation.	28
5.2	Illustration of a trapped ganglion in a simple geometry consisting of four circular, aligned pillars.	29
6.1	Typical set up of a micromodel (Kawale, 2017), the direction of depth is in the vertical direction.	31
6.2	Geometries of the four models used by Kawale (2017), including a) aligned squares, b) staggered squares, c) aligned circles and d) staggered circles.	33

6.3	Micromodel used By Jones <i>et al.</i> (2016); Getrouw (2016). On the left, it shows the model as seen under a microscope. The figure on the right is the altered model for porosity characterization.	35
6.4	Enlarged image of Model A used by Jeong and Corapcioglu (2003). Note the example dimension of the ganglion length (L_g).	37
6.5	Capillary Desaturation Curves for the data obtained from Jeong and Corapcioglu (2003).	38
6.6	Sample from the SRC-1 model used by Ibrahim <i>et al.</i> (2008).	39
6.7	Capillary Desaturation Curves for Ibrahim <i>et al.</i> (2008) for both the conventional and the new capillary number.	41
6.8	Micromodel used by Yeganeh <i>et al.</i> (2016). Dimensions of the three different throat widths are given. The dimensions of the pore bodies and ganglion lengths are given in red.	42
6.9	Desaturation curves for the data provided by Yeganeh <i>et al.</i> (2016).	42
7.1	Pressure gradient against both the conventional and the new capillary number for each of the four models by Kawale (2017).	46
7.2	Capillary desaturation curves using the conventional capillary number for the five analyzed desaturation experiments by (Jeong and Corapcioglu, 2003; Ibrahim <i>et al.</i> , 2008; Yeganeh <i>et al.</i> , 2016).	47
7.3	Capillary Desaturation curves for the newly defined capillary number for the models by (Jeong and Corapcioglu, 2003; Ibrahim <i>et al.</i> , 2008; Yeganeh <i>et al.</i> , 2016).	48
A.1	Graph showing the relationship between pressure gradient and residual air saturation for the five models used in the research by Al Quaimi and Rossen (2017).	59
A.2	capillary desaturation curves using the conventional capillary number (equation 3.3) for the five fracture models used by Al Quaimi and Rossen (2017). Notice how the curves do not follow a single trend (Al Quaimi and Rossen, 2017).	60
A.3	Capillary desaturation curves for the newly defined capillary number based on a force balance across a trapped ganglion. Notice how the curves now follow a single trend (Al Quaimi and Rossen, 2017).	60
B.1	Parameters of the Aligned Squares model.	61
B.2	Parameters of the Staggered Squares model.	62
B.3	Parameters of the Aligned Squares Model.	62
B.4	Parameters of the Staggered Circles Model.	63
B.5	Desaturation data by Jones <i>et al.</i> (2016). Above shows the measured desaturation, and below shows the viscosity as a function of the superficial velocity.	64
B.6	Distribution graphs showing the pore throat and pore body sizes for the models provided by Jeong and Corapcioglu (2003).	65
B.7	Desaturation curves presented by Jeong and Corapcioglu (2003)	65
B.8	Model of the measurements of the sizes of the throats and bodies.	68
B.9	Image used for determining the porosity of the model.	69
B.10	Capillary Desaturation Curves for the two experiments carried out by Yeganeh <i>et al.</i> (2016). The top model is for experiment 1 (hexadecane/water). The bottom figure is for experiment 2 (crude oil/water).	70
C.1	Pressure gradient and residual saturation data for the models by (Jeong and Corapcioglu, 2003; Ibrahim <i>et al.</i> , 2008).	71
C.2	Capillary Desaturation curves for Yeganeh Experiment 2 if the contact angle between the Brine and the Crude oil is increased from 47 to 70 degrees.	72
C.3	The geometric terms plotted against the permeability for the 9 analyzed models.	73

List of Tables

6.1	Parameters of the microfluidic devices given by Kawale (2017).	33
6.2	The most important geometrical parameters used for the models of Kawale (2017). . .	34
6.3	Most important parameters for the model provided by Jones <i>et al.</i> (2016).	35
6.4	Parameters of the microfluidic devices used by (Jeong and Corapcioglu, 2003).	36
6.5	Properties of chemicals used by Jeong and Corapcioglu (2003). IFT is interfacial tension. The contact angle is only measured for the TCE and is measured through the wetting phase. If the box is empty, the value is not given by Jeong and Corapcioglu (2003). . .	37
6.6	Most important parameters for the model provided by Ibrahim <i>et al.</i> (2008).	40
6.7	Properties of the micromodel used by Yeganeh <i>et al.</i> (2016).	41
6.8	An overview of all the properties of the micromodels presented in chapter 6. Author refer- ences are shortened in order to fit on the page (Kawale, 2017; Jeong and Corapcioglu, 2003; Jones <i>et al.</i> , 2016; Ibrahim <i>et al.</i> , 2008; Yeganeh <i>et al.</i> , 2016).	44
7.1	Aspect ratios of the different micromodels.	45
7.2	Tortuosity and the geometric (G) term for each micromodel.	49
B.1	Desaturation data for the data of model A from Jeong and Corapcioglu (2003), both original and converted data for proper use.	66
B.2	Desaturation data for the data of model B from Jeong and Corapcioglu (2003), both original and converted data for proper use.	66
B.3	Measurements for the pore body sizes of the model SRC-1 by Ibrahim <i>et al.</i> (2008) . .	66
B.4	Measurements for the pore throat sizes of the model SRC-1 by Ibrahim <i>et al.</i> (2008) . .	67
B.5	Ganglion length measurements for the model by Ibrahim <i>et al.</i> (2008).	67

Nomenclature

β	Heterogeneity factor
η	Aspect Ratio
λ	Velocity ratio between two parallel capillary tubes (Pore-Doublet Model)
μ	Viscosity
∇P	Pressure Gradient
ϕ	Porosity
ρ	Density
σ	Interfacial tension between two phases
τ	Tortuosity
θ	Contact angle between two phases. Measured through the water phase
A	Cross-sectional area perpendicular to flow direction
d	Aperture of a fracture
d_b	Aperture of a pore body in a fracture
d_h	Hydraulic Aperture of a Fracture
d_t	Aperture of a pore throat in a fracture
$F(\xi)$	Correctional factor for capillary transport through rectangular tubes
F_c	Capillary Forces
F_v	Viscous forces
H	Height/depth of a slit
K	Permeability
L	Length of a pore-doublet model
L_g	Length of a nonwetting trapped ganglion
$N_{ca,c}$	Critical Capillary Number
$N_{ca,t}$	Total capillary number
N_{ca}	Capillary Number
$N_{v,cap}$	Capillary trapping number
P_c	Capillary Pressure
P_w	Pressure acted by the wetting phase
P_{nw}	Pressure acted by the nonwetting phase
Q	Flow rate through a porous medium

q	Flow rate through pore-doublet model
R	Radius of a cylindrical capillary tube
r_f	Radius of pore body (geological rock)
r_i	Principal radii of an interface. Perpendicular to each other
r_n	Radius of a pore neck (geological rock)
r_t	Radius of a grain (geological rock)
t	Time
u	Darcy velocity through a porous medium
v	Flow Velocity, used in pore-doublet model
W	Width of a smooth slit, or width of a micromodel
w	Width
w_b	Width of a pore body in a micromodel
w_t	Width of a pore throat in a micromodel
Z	Depth of a Micromodel
z	Depth

1

Introduction

The oil recovery process is usually subdivided into three categories. Primary oil recovery is when an oil field is first used in production processes and the recovery is the result of a pressure difference between the high pressure of the fluids present in the reservoir and the low pressure inside the wellbore. Primary oil recovery is responsible for the recovery of about 10 to 25 percent of the total reservoir potential (Lake, 1989). Secondary recovery is the process where external fluids are injected into the reservoir in order to “push” the oil towards the extraction well. This is often referred to as water-flooding (Ibrahim *et al.*, 2008). Secondary oil recovery can produce an additional 10 to 20 percent of the reservoir potential (Lake, 1989). However, the majority of the oil remains trapped in the reservoir. Tertiary oil recovery (often referred to as enhanced oil recovery (EOR)) is the process in which this substantial amount of oil is recovered (Yeganeh *et al.*, 2016). Different methods of Enhanced Oil Recovery include the addition of chemicals such as surfactants, polymers and Alkaline.

Because of reducing oil availability in the future, the process of enhanced oil recovery will in the future become increasingly relevant as more oil companies will revisit older oil fields to mobilize and extract the residual oil (Ibrahim *et al.*, 2008). One of the main problems that arises during enhanced oil recovery is that after the water-flooding processes, the residual oil is often left trapped inside the pores of the reservoir. This process is often referred to as capillary trapping (Peters, 2012). The amount of trapped oil in a reservoir strongly depends on the geometry of the porous medium, the chemistry of the medium as well as the characteristics of the displacing fluid (Yeganeh *et al.*, 2016). One of the ways to analyze the mobilization of the trapped oil is by making use of capillary numbers, which is a ratio of the viscous forces of the displacing fluid over the capillary forces of the trapped oil (Sheng, 2011). In the past, numerous equations for the capillary number have been developed in order to describe the process of mobilization of the trapped oil. Moore and Slobod (1954) developed a capillary number where the displacing fluid is characterized by its viscosity and the Darcy velocity inside the porous medium. Reed and Healy (1977) developed a capillary number where the displacing fluid is described by the pressure gradient and the permeability of the medium. Hughes and Blunt (2001) developed a capillary number to describe the mobilization of trapped fluid inside fractures.

Over the last 30 to 40 years, microfluidic devices have proven to be a useful tool in analyzing fluid transport inside porous media. Micromodels are artificial 2D networks consisting of pore bodies and interconnecting pore throats. They are usually transparent so that flow behaviour can be analyzed (Jeong and Corapcioglu, 2003). Reservoir flooding at high capillary numbers can help to recover the residual oil (Ibrahim *et al.*, 2008). For a long time capillary numbers were calculated using only the viscous and capillary forces, ignoring the geometry of the porous medium. This works well for describing the mobilization of trapped residual oil in geological rock. However, these equations do not translate very well when they are applied to microfluidic models. The main problem is that it is not possible to describe capillary desaturation in different micromodels by a single curve. Over the past two years, a number of papers have been presented where an equation for the capillary number is developed that accounts for the geometry of the medium. Al Quaimi and Rossen (2017) developed a capillary number based on a force balance on a trapped ganglion of nonwetting fluid inside a fracture. Yeganeh *et al.*

(2016) used a similar method to derive a new capillary number for fluid flow inside rock matrix. No new capillary number has been derived yet for fluid transport inside 2D microfluidic devices. It would therefore be beneficial to have an equation for the capillary number that can be used for analyzing microfluidic devices.

The research presented in this report will focus on the derivation of a new capillary number that can be used to better analyze the mobilization of trapped nonwetting fluids inside microfluidic devices. The equation for the capillary number will be based on a force balance across a trapped ganglion in a pore body. The derivation will be analogous to the derivation performed by Al Quaimi and Rossen (2017) for mobilization inside fractures. The most important objective of the report is that the new equation for the capillary number can be used to describe the desaturation of microfluidic devices by a single curve.

1.1. Scope of Report

The research performed for this project will focus on deriving a new equation for the capillary number for microfluidic devices. Desaturation data of micromodels will be analyzed using both the conventional and the newly defined capillary number in order to test the validity of the newly derived capillary number. However, the research was limited by a number of factors. First of all, there is the limited time available for the research. This meant that there was no time to test desaturation on self-made micromodels. This means that the desaturation data used for testing the new capillary number had to be obtained elsewhere. It was decided to analyze desaturation data obtained from literature available on the matter. This posed another problem. As mentioned before, the conventional capillary numbers that are used to analyze desaturation of micromodels did not take the geometry of the medium into account. Due to the complex nature of the newly defined capillary number, often critical parameters such as pore body and throat width were not reported. This means that useful data is difficult to come by. In order to obtain enough useful data, the decision was made to not only analyze oil desaturation, but also take other Non-Aqueous Phase Liquids (NAPL) as well as gas (air) into account. The benefit of this is that analyzing for different types of wetting and nonwetting combinations makes it possible to analyze the effects that different fluid characteristics have on the new definition of the capillary number.

1.2. Outline of Report

The report will begin with a part on the background information that is needed to understand the problem of capillary trapping inside porous medium. Chapter 2 will explain the principals of wettability of porous media, capillarity, capillary trapping and mobilization. This will be used further in the report in the derivation of the new capillary number. Next, chapter 3 will explain the methods of research into capillary desaturation done in the past. The nature and background of conventional capillary numbers is described. Also, the use of capillary desaturation curves (CDC) is described. The next part (Chapter 4) will talk about the new capillary number derived for fractures as performed by Al Quaimi and Rossen (2017). This is done in order to gain an understanding in how a capillary number based on a force balance on a trapped ganglion can be derived. Also, the background of the relationship between permeability (K) and the aperture of the fracture is given. This relationship is important because it will again be used in the derivation of the capillary number for microfluidic slits. The derivation of the new definition of the capillary number for microfluidic slits is given in chapter 5. In this chapter, the concept of tortuosity is also introduced to get a better relationship between permeability and the depth of the system. A number of micromodels and their data was used from published papers. The model parameters and their desaturation data are described in chapter 6. The obtained results of the data are analyzed in chapter 7 in order to find the functionality of the new capillary number. The conclusions of the report are given in chapter 8. Discussions regarding the obtained results and any points that should be noted for further study are given in chapters 9 and 10.

2

Capillarity, Trapping and Mobilization

The displacement of a non-wetting fluid through porous media with the use of an immiscible wetting fluid is a crucial aspect of enhanced oil recovery (EOR). The pore space within the medium is highly disordered, meaning that the transport of through the reservoir is highly complicated. One of the main obstacles that has to be overcome is the trapping of discrete ganglia of the non-wetting fluid within the porous medium (Datta *et al.*, 2014).

In enhanced oil recovery, injection wells are often used to inject displacement fluids (such as water), gasses or foams (foams are a dispersion of gas in water, stabilized by surfactants (Lake, 1989)) in order to mobilize the oil droplets and migrate them through the pore spaces in the porous medium. However, the migration of oil within a porous medium is limited by capillarity and relative permeability (Lake, 1989). Especially capillarity plays an important role in the residual oil saturation. As a result of capillarity, oil ganglions may snap off and get trapped within the pore bodies. In order to mobilize the trapped ganglions, the pressure needs to be increased until the pressure gradient across the trapped ganglion is greater than the capillary pressure difference within the ganglion (Peters, 2012; Lake, 1989; Datta *et al.*, 2014).

This chapter will describe the trapping and the mobilization of non-wetting fluids within porous media. In the first part of the chapter, wettability will be analyzed. I will then explain how capillarity work. Next, the theory behind the trapping will be analyzed. In the last part of the chapter, mobilization will be analyzed.

2.1. Wettability and Two Phase Flow

In this report, the mobilization of a residual nonwetting fluid (oil) driven by a wetting fluid will be described. Wettability describes the "preference" of a solid (in our case the microfluidic model) to be in contact with one fluid rather than another (Abdallah *et al.*, 2007). The solid can either be water-wet or oil-wet. Strongly water-wet means that the solid prefers contact with water. Strongly oil-wet on the other hand means that the solid prefers contact with oil. If the preference is uncertain, the solid is either referred to as intermediate-wetting or neutral wetting (Abdallah *et al.*, 2007).

A drop of wetting fluid coming into contact with a water-wet solid that is covered by another wetting fluid will do one of the following. Most likely it will displace the nonwetting fluid. At the extreme, it will spread out over the entire surface of the solid. Conversely, if a nonwetting fluid is dropped on the same surface, the fluid will contract, minimizing the contact area between both the solid as well as the wetting fluid (Abdallah *et al.*, 2007).

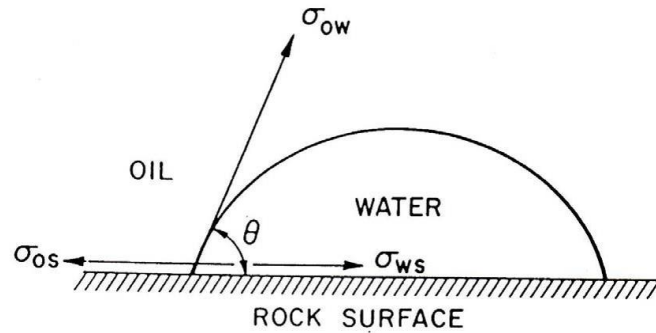


Figure 2.1: Interfacial tensions in a water-oil-solid system (Peters, 2012).

Consider a simple water-oil-solid system as shown in figure 2.1. It can be seen that three interfacial tensions occur in a multiphase system (Peters, 2012). These tensions are given by the symbol σ :

- σ_{os} is the oil-solid interfacial tension;
- σ_{ow} is the oil-water interfacial tension;
- σ_{ws} is the water-solid interfacial tension.

One of the main characteristics of wetting and nonwetting fluids is the contact angle between the oil-water interface and the rock surface. The contact angle is given by θ and is measured through the water. See figure 2.2. A perfectly wetting fluid on a perfectly water-wet rock will have a theoretical contact angle of 0 degrees. Conversely, a perfectly nonwetting fluid will have a contact angle of 180 degrees (Abdallah *et al.*, 2007; Peters, 2012). At equilibrium, the interfacial tensions are related by the Young-Dupre equation (equation 2.1) obtained by considering horizontal equilibrium of the point of contact of the interfacial tensions (Peters, 2012).

$$\sigma_{os} - \sigma_{ws} = \sigma_{ow} \cos(\theta) \quad (2.1)$$

It is important to know that the interfacial tensions between the oil-solid and water-solid surfaces cannot be directly measured. However, by using the Young-Dupre equation, the difference between the two can be calculated if the oil-water interfacial tension and the contact angle are measured (Peters, 2012). Knowing the contact angle and the difference between the oil-solid and water-solid interfacial tensions is important because it tells a lot about the wettability of the rock. Peters (2012) describes four possible scenarios:

1. σ_{os} and σ_{ws} are equal. This means that the left side of equation 2.1 is zero. Since the oil-water interfacial tension (σ_{ow}) is non-zero, only the $\cos(\theta)$ term can be zero. θ therefore is 90 degrees. This means that the rock surface has no preference for oil-wetting or water-wetting and therefore either is neutral-wetting or intermediate-wetting. See figure 2.2b.
2. If $\sigma_{ws} < \sigma_{os}$, it means that the left side of equation 2.1 is positive. This means that the contact angle is less than 90 degrees, resulting in a preferably water-wet rock. See figure 2.2c.
3. Conversely, if $\sigma_{ws} > \sigma_{os}$, it means that the contact angle is larger than 90 degrees, resulting in a preferably oil-wet rock. See figure 2.2a.
4. Complete spreading of oil over the rock surface will occur if the contact angle is 180 degrees and complete spreading of water will occur if the contact angle is zero. However, this has never been observed within reservoir fluids (Peters, 2012). see figure 2.2d.

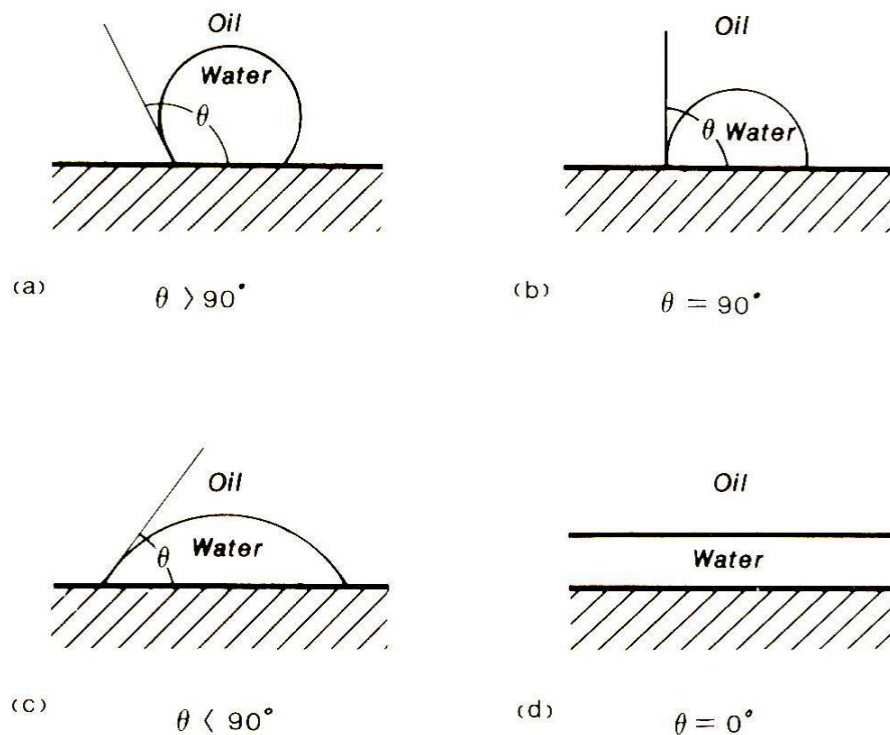


Figure 2.2: Equilibrium contact angles for four different wettabilities (Peters, 2012).

Wettability has a significant effect on multiphase rock-fluid interactions and therefore is important for this study. The wettability of a porous medium affects

- The microscopic fluid distribution at the pore scale in the porous medium;
- The magnitude of irreducible water saturation;
- Efficiency of multiphase displacement with the medium;
- Residual oil saturation;
- Capillary pressure and the Capillary-Pressure Curve (CPC) (Peters, 2012).

Wettability determines the microscopic fluid distribution at the pore scale. The wetting fluid will occupy the small pores, form a coating around the grains and occupying corners of the grain contacts. The wetting phase will occupy the small pores in order to minimize the effective free surface energy of the system. The nonwetting fluids occupy the larger pores and are located as "bubbles" in the centre of the pores (Peters, 2012). This is illustrated in figure 2.3.

Irreducible water saturation (IWS) is the maximum water saturation that a reservoir can have without allowing water to flow. That is the fraction of the pore volume that is occupied by water at maximum hydrocarbon saturation (El Gendy, 2016). This water has not been displaced by hydrocarbons, and it adheres to rock surfaces and occupies small pores (El Gendy, 2016). The IWS for oil-wet reservoir tends to be lower than for water-wet reservoirs, namely 20-25 percent for water-wet reservoirs and lower than 15 percent for oil-wet reservoirs, respectively (Peters, 2012).

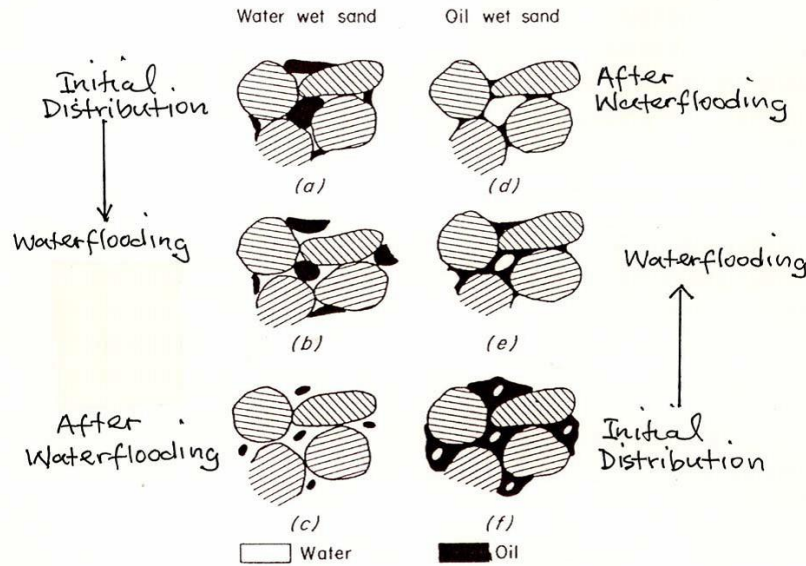


Figure 2.3: Fluid distribution as a function of wettability (Peters, 2012).

Wettability has a major effect on the efficiency of immiscible displacement. See figure 2.4. In a water-wet reservoir, the water tends to adhere to the grains, thereby increasing the efficiency of the oil displacement. Residual oil is trapped in the centre of the larger pores. In an oil-wet reservoir on the other hand, injected water tends to channel through the pores, leaving a considerable amount of residual oil. The oil adheres to the grains and occupies the small pore spaces between the grains. The efficiency of oil recovery is considerably less than for water-wet reservoirs (Peters, 2012).

2.2. Capillary Pressure and Transport

2.2.1. Definition of Capillary Pressure

Analogous to single phase flow, where porosity and permeability are the most basic properties of describing the flow, capillary pressure is the most basic rock-fluid characteristic in multiphase flow. This is because interfacial forces, such as capillary pressures, are easily the strongest forces within multiphase flow at typical velocities (Lake, 1989). Capillary pressure arises when two immiscible fluids are in contact with each other and share the same pore space. When two fluids are in contact with each other, a pressure discontinuity arises that depends on the curvature of the interfacial boundary (Peters, 2012). The pressure on the concave side (usually the non-wetting phase) of the interface is higher than on the convex side. The capillary pressure is given by the Laplace equation:

$$P_c = P_2 - P_1 = \sigma \left(\frac{1}{r_1} + \frac{1}{r_2} \right) = \frac{2\sigma \cos(\theta)}{R} \quad (2.2)$$

In this formula, P_2 is the pressure from the concave side of the interface, P_1 is the pressure exerted by the convex side. σ is the interfacial tension between the wetting and the nonwetting fluid. The curvature is given by r_1 and r_2 , which are referred to as the principal radii of the curvature of the interface. They are mutually perpendicular. The right hand side of equation 2.2 is the equation for capillary pressure in a tube. R is the radius of the tube, which is inversely related to the curvature (Lake, 1989; Peters, 2012).

Equation 2.2 suggests that a capillary pressure is zero when there is a flat interface between the two fluids. This means that the the principal radii become infinite (Peters, 2012). Also, the contact angle would become 90 degrees, resulting in the fact that $\cos(\theta)$ will be zero on a flat surface. In more complicated geometries, the curvature is made up of different and multiple curvatures. If this is the case, the $1/R$ term in equation 2.2 is replaced by the mean curvature (Lake, 1989).

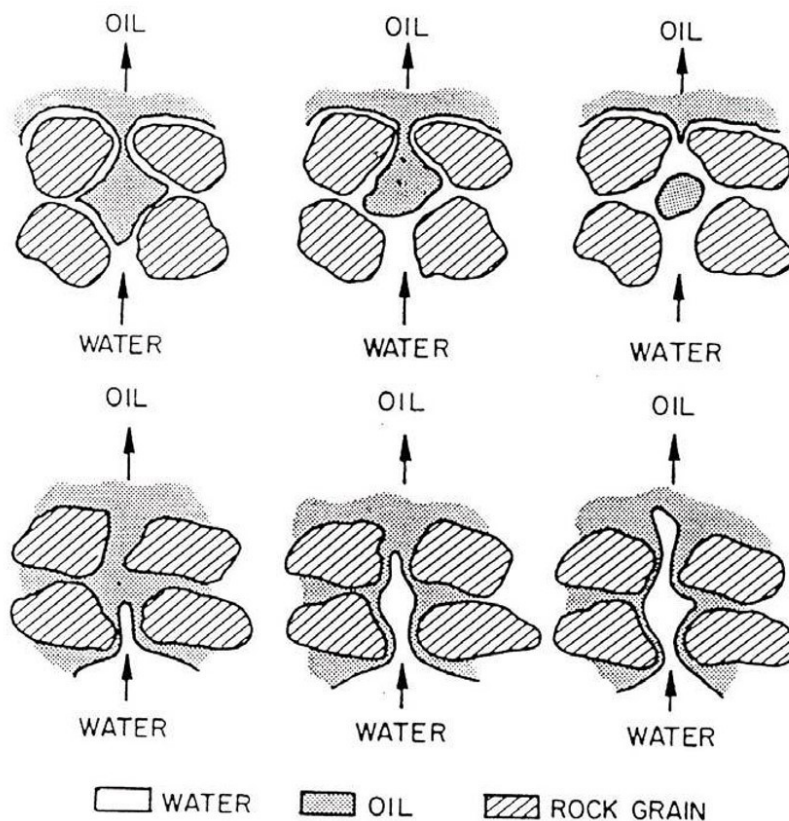


Figure 2.4: Immiscible displacement of fluids as a function of wettability on the pore scale, for a strongly water wet medium (above) and a strongly oil wet medium (below) (Peters, 2012).

From equation 2.2, it becomes apparent that the capillary pressure is inversely proportional to the radius. Consider a basic test involving a number of test tubes, each having a different radius. See figure 2.5. It can be seen that the water rises higher as the radius of the test tube decreases. This corresponds to a higher capillary pressure (Lake, 1989; Peters, 2012).

2.2.2. Capillary Pressure Curves

It is impossible to use the Laplace equation to calculate the capillary pressure within actual porous media. This is mainly due to the complex structure of the pores (Peters, 2012). Instead, the relationship between the capillary pressure and the wetting saturation is measured experimentally. During the experiments, the porous media are either subjected to drainage (a wetting fluid is displaced by a non-wetting fluid) or imbibition (a nonwetting fluid is displaced by a wetting fluid). A drainage experiment is carried out as follows: A porous medium is initially completely filled with a wetting fluid (saturation of 100 percent). The medium is then subjected to a nonwetting fluid. The pressure of the nonwetting fluid is then increased causing it to displace the wetting fluid. The volume of the drained wetting fluid is measured in order to calculate the total saturation. The pressure required to drain the medium and the saturation can then be plotted on a capillary pressure curve (CPC). See figure 2.6 (Peters, 2012).

A capillary pressure curve has a number of characteristic features. First of all, there is the threshold pressure, or drainage pressure (P_d). This is the minimum pressure that must be applied in order to initiate the drainage. It is determined by the size of the largest pores connected to the surface of the medium. If the pores are larger, the threshold pressure will be lower, because of lower capillary pressure due to a larger pore radius. Wettability also plays an effect. If the medium has no strong preference for the initially present wetting fluid, P_d is zero, and the drainage initiates automatically.

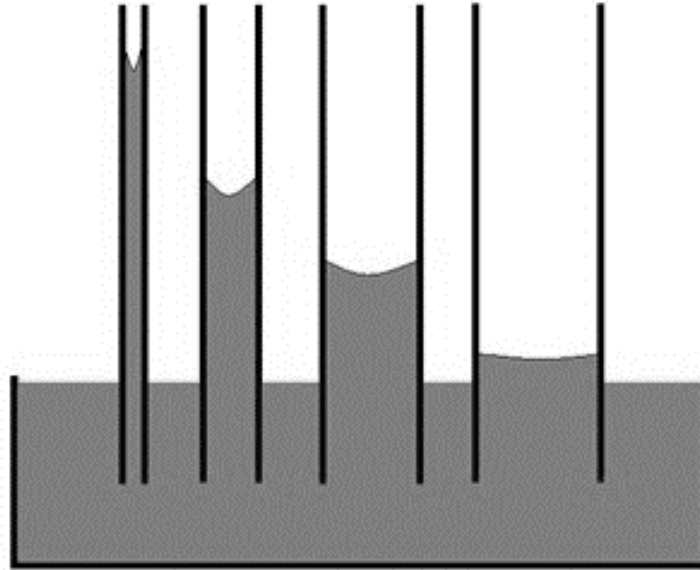


Figure 2.5: A capillary tube experiment shows us that if the radius decreases, the capillary pressure increases, causing the interface to raise higher.

As the pressure of the nonwetting fluid is further increased, the smaller pores are also invaded by the displacing fluid and the saturation of the wetting fluid decreases further. Eventually, the wetting phase becomes discontinuous and the saturation cannot be further reduced. This point is known as the irreducible wetting phase saturation (S_{wir}) (Peters, 2012). The threshold pressure and the irreducible wetting phase saturation is dependent on grain size. A smaller grain size means a smaller pore size and therefore a higher threshold pressure and irreducible phase saturation. This is because in a water-wet environment, the water tends to adhere to the grains. A smaller pore size means that a relatively larger fraction of the pore space will remain filled with wetting fluid that adheres to the grains. Also, smaller grains means smaller pore radii. This results in larger capillary pressures, and therefore a larger threshold pressure. See figure 2.7 (Peters, 2012).

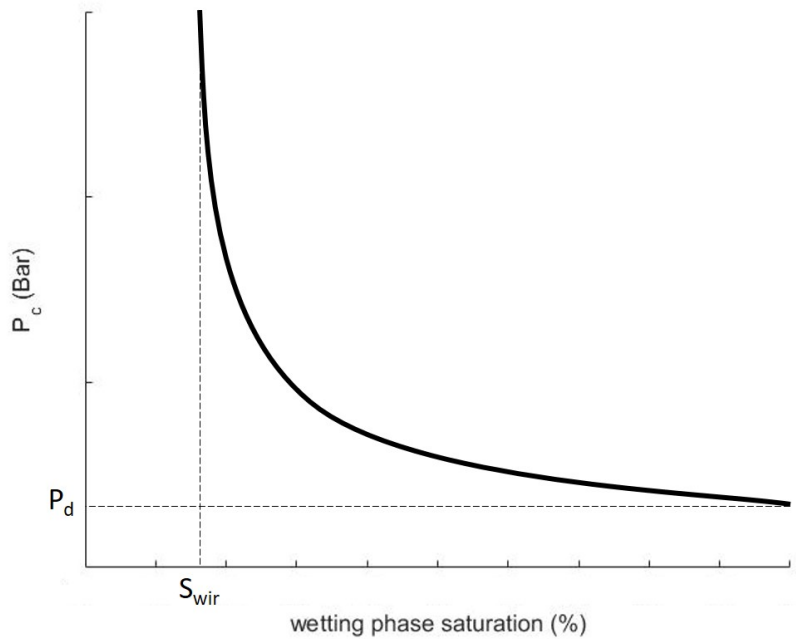


Figure 2.6: Schematic overview of a capillary pressure curve.

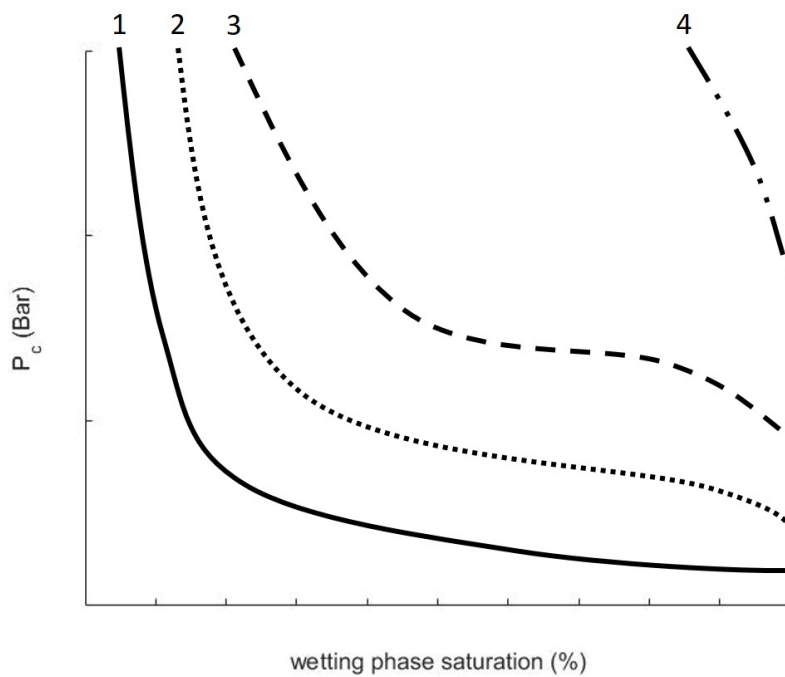


Figure 2.7: Schematic overview for capillary pressure curves for drainage processes in rocks with different pore sizes. curve 1 represents a rock with the largest pore size, and 4 with the smallest.

2.2.3. Hysteresis

Capillary pressure curves show a marked hysteresis depending on whether the curve is determined under a drainage or an imbibition process. See figure 2.8. The capillary pressure for drainage will always be higher for a drainage process than it is for an imbibition process given the same wetting phase saturation (Lake, 1989). If during spontaneous imbibition, the capillary pressure is reduced to zero, the wetting phase saturation will not fully restore to 1.00. This is due to residual nonwetting saturation. The point where the spontaneous imbibition curve ends depends on the wettability of the rock. The stronger the preference for the wetting phase is, the closer the end of the imbibition curve will be to the residual nonwetting phase saturation, which is given by $S_{o,r}$ (Peters, 2012). The end point of the spontaneous imbibition curve is given by $S_w = 1 - S_{o,r}$. This has to do with the nature of immiscible displacement. As the wetting phase imbibes into the rock, some nonwetting phase will be trapped inside pore bodies. This means that less wetting phase can enter the pores, and therefore the wetting phase saturation on the imbibition curve will be less than on the drainage curve given the same capillary pressure (Peters, 2012).

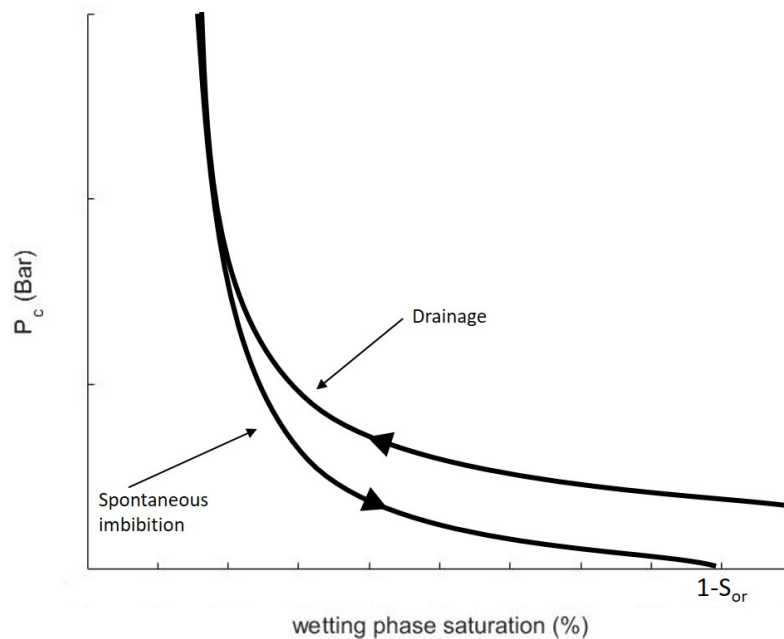


Figure 2.8: Sketch of a basic hysteresis curve.

The contact angle between the wetting and the nonwetting phase has a major effect on capillary hysteresis. In capillary hysteresis, as drainage occurs, and the nonwetting fluid forces the wetting fluid out, the contact angle θ is reduced. Conversely during imbibition, the contact angle is increased. From Laplace's equation (Equation 2.2), it becomes apparent that for a smaller contact angle, the capillary pressure is higher. This means that the capillary pressure for drainage is higher than it is for imbibition given the same wetting phase saturation (Peters, 2012).

Pore structure has a major effect on hysteresis. Consider a permeable medium idealized by an arrangement of decreasing pore sizes and pore throats. See figure 2.9. For initial drainage, a capillary pressure is required depending on pore throat radius R_{t1} .

$$P_{c,D,rt1} = \frac{2\sigma \cos(\theta)}{R_{t1}} \quad (2.3)$$

From Laplace's equation, it becomes apparent that in order to pass the next, narrower pore throat (R_{t2}), the capillary pressure must be increased. The same holds for R_{t3} and R_{t4} . If then the imbibition process is started, the capillary pressure is reduced. In order to re-saturate pore 4 with wetting fluid,

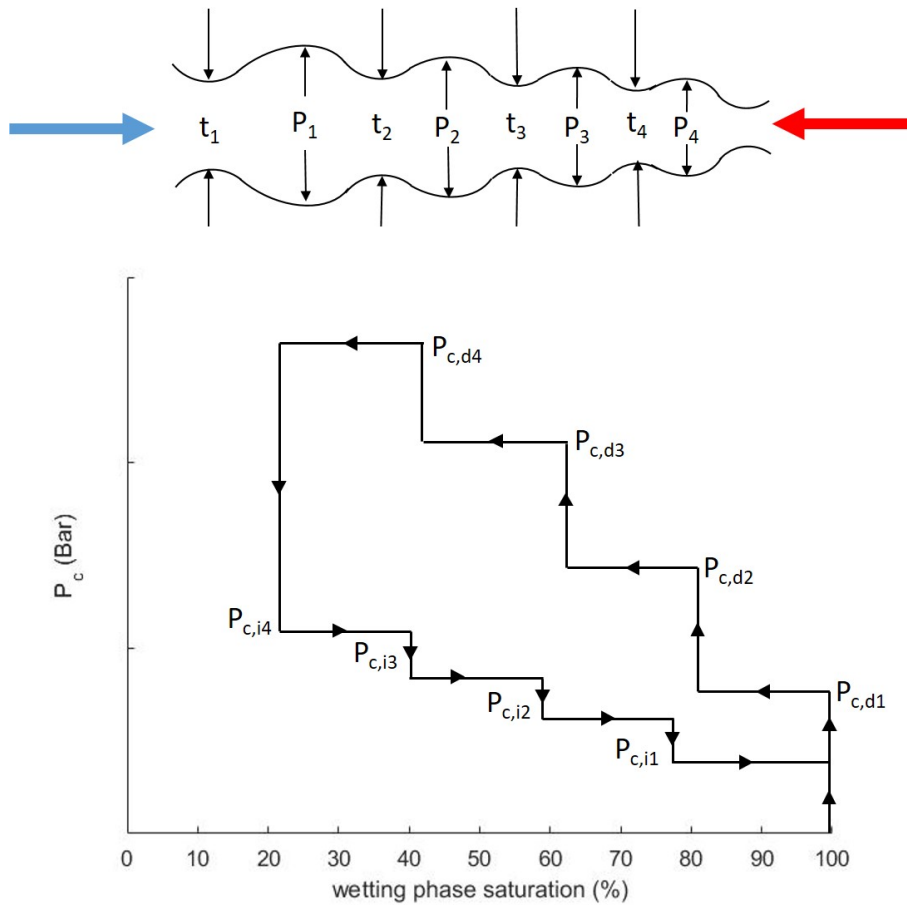


Figure 2.9: Capillary pressure hysteresis in an idealized pore structure with (a) the structure of the idealized pores and (b) the corresponding capillary pressure curve. Blue is the direction of drainage and red is the direction of imbibition.

the capillary pressure must be reduced to

$$P_{c,lrp4} = \frac{2\sigma \cos(\theta)}{R_{p4}} \quad (2.4)$$

where R_{pi} is the radius of the pore body. In order to fully saturate the remaining three pores, the capillary pressure must be further reduced to (Peters, 2012):

$$P_{c,lrp1} = \frac{2\sigma \cos(\theta)}{R_{p1}} \quad (2.5)$$

2.3. Capillary Trapping

As can be seen in figure 2.6, it is generally not observed that during immiscible displacement one phase is completely removed from the medium. There is always a residual phase that is trapped. This situation is referred to as capillary trapping. Experimentally, there are two ways capillary trapping can be explained. Lake (1989) and Peters (2012) describe the pore-doublet model and the snap-off model. The trapping of nonwetting phases in water-wet systems is described here

2.3.1. Pore-Doublet Model

A Pore doublet model consists of two tubes that represent two pores. The tubes are parallelly connected to each other at both ends and one tube has a larger radius than the other. See figure 2.10. Initially, the doublet is completely filled with nonwetting phase. A wetting phase is then injected in the doublet

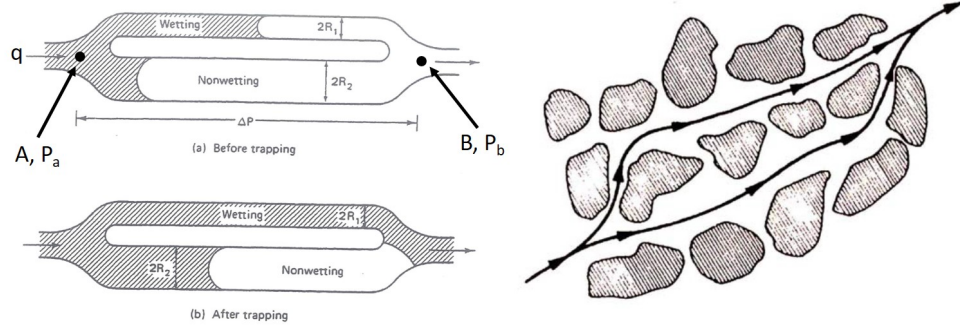


Figure 2.10: Illustration of a pore-doublet model on the left (Lake, 1989), and a schematic overview on how it works in geological rock Peters (2012).

at a rate q and displaces the nonwetting fluid. The problem that arises is that the interface in one pore moves faster than in the other. It is important to determine which interface reaches the endpoint faster. The nonwetting phase in the other pore gets trapped (Lake, 1989; Peters, 2012). To determine which interface reaches the endpoint quicker and which nonwetting phase gets trapped, expressions that describe the velocities of the two interfaces need to be derived. Peters (2012); Lake (1989) give a well described derivation for the pore-doublet model. Without going into too much detail, the most important factors determining in which pore the nonwetting fluid will be trapped will be given. Peters (2012) states that for an incompressible fluid, the flow rate across the model can be given by

$$q = q_1 + q_2 \quad (2.6)$$

where q_1 and q_2 are the flow rates in either pore, respectively. The next step is to define the interface velocities within the two capillary tubes in terms of the flow rate through them. This is easily done using equation 2.7. In Equation 2.7, the subscript i represents either one of the two capillary tubes.

$$v_i = \frac{q_i}{\pi R_i^2} \quad (2.7)$$

The next step is to introduce two terms, namely β and $N_{v, cap}$. β is the heterogeneity factor and is given by $\beta = R_2/R_1$. It is a ratio between the dimensions of both capillary tubes. The closer β is to 1, the more both tubes are alike. $N_{v, cap}$ is a capillary number and it gives the ratio of the viscous force to capillary forces at the pore scale. For this case, $N_{v, cap}$ is defined as

$$N_{v, cap} = \frac{q\mu L}{\pi R_1^3 \sigma \cos \theta} \quad (2.8)$$

The next step is to calculate the ratio of velocities. Chatzis and Dullien (1983) define this ratio as λ . See (Equation 2.9).

$$\lambda = \frac{v_2}{v_1} = \frac{4N_{v, cap} + \left(\frac{1}{\beta} - 1\right)}{\frac{4N_{v, cap}}{\beta^2} - \beta^2 \left(\frac{1}{\beta} - 1\right)} \quad (2.9)$$

The ratio between velocities can be used to determine the trapping conditions within the pore doublet model. If $\lambda > 1$, it means that the velocity in the larger pore is greater than in the smaller pore. Thus, the nonwetting phase will be trapped in the smaller pore. Conversely, if $\lambda < 1$, the nonwetting fluid will be trapped in the larger pore. The critical value of $N_{v, cap}$ that determines the trapping in either pore is given by:

$$N_{v, cap} = \frac{\beta(\beta^2 + 1)}{4(\beta + 1)} \quad (2.10)$$

If $N_{v, cap}$ is smaller than its critical value, the nonwetting phase will be trapped in the larger pores. And conversely, if $N_{v, cap}$ is larger than its critical value, the nonwetting phase will be trapped in the smaller pore (Peters, 2012). The conditions for trapping can also be determined using the flow rate q . If the flow rate of the wetting phase is low, it means that capillary forces play a more dominant role than the

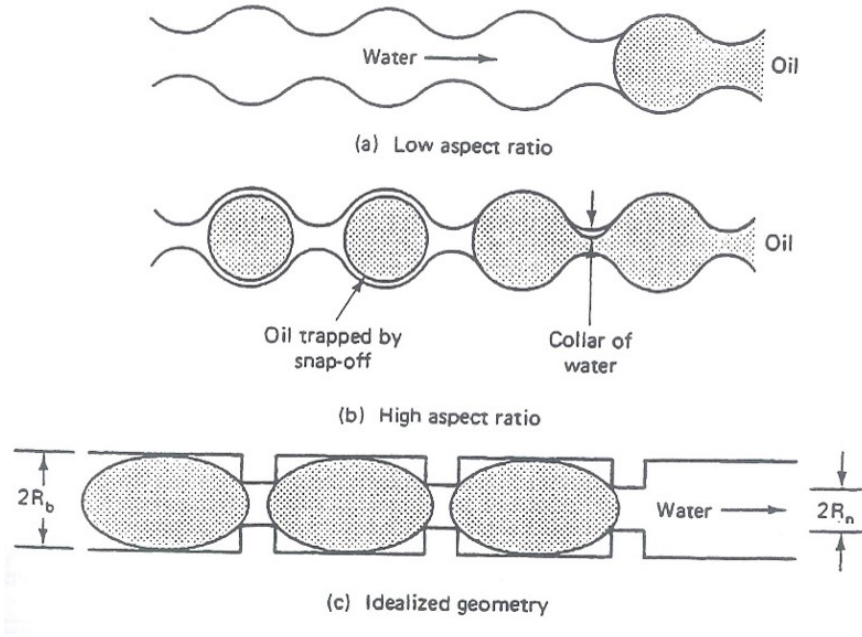


Figure 2.11: Snap-off model for capillary trapping showing 3 different aspect ratios (Chatzis and Dullien, 1983).

viscous forces in the displacement of the interface. see chapter 3.1. This means that velocity in the smaller pore is higher, and therefore the nonwetting phase in the larger pore will be trapped (Lake, 1989; Moore and Slobod, 1954).

2.3.2. Snap-Off Model

When a nonwetting phase is forced through a pore constriction, it can suffer from capillary instability and snap off at the end of the constriction (Peters, 2012). The simplest snap-off model assumes a single flow path and consists of a tube of variable radius. There is a nonwetting phase flowing through the tube whilst the sides of the tube are coated with a wetting phase in order to have a unique capillary pressure everywhere (Lake, 1989). Also, this creates more natural situations, where the wetting fluids tends to adhere to the water-wet medium, between the nonwetting fluid and the wall. The capillary pressure varies across the flow path. By Laplace's law it holds that the capillary pressure is high where the path is narrow, and low where the path gets wider. Trapping by snap-off is controlled by the ratio between the pore body and the pore throat. This is called the aspect ratio and is given by equation 2.11 The higher the aspect ratio is, the more the nonwetting phase will suffer from capillary instability and snap off (Peters, 2012). See figure 2.11.

$$AspectRatio = \eta = \frac{D_1}{D_2} = \frac{D_{body}}{D_{throat}} \quad (2.11)$$

The snap off model can also be applied to an experimental porous medium. Capillary instability and snap-off will occur if the capillary pressure at the pore throat exceed the capillary pressure at the leading edge of the nonwetting phase (Peters, 2012). See equation 2.12:

$$P_c = \sigma \left(\frac{1}{r_n} - \frac{1}{r_t} \right) > \frac{2\sigma}{r_f} \quad (2.12)$$

In equation 2.12, r_n is the radius of the pore neck, r_t is the radius of the grains and r_f is the mean radius of the pore body (Peters, 2012). Of course, in any real porous medium, local conditions will determine whether the doublet system will apply or snap-off. Chatzis *et al.* (1983) found out that approximately 80 percent of the trapped nonwetting phase occurs as a result of snap-off. The other 20 percent is caused by pore doublet or combinations of both categories. See figure 2.13.

2.4. Mobilization of the Trapped Nonwetting Phase

Once the residual nonwetting phase has been trapped, it needs to be mobilized. In order to do so, the pressure gradient needs to be increased. The required pressure gradient can often be much higher than can be obtained under normal flooding conditions (Peters, 2012). Peters (2012) calculates the required pressure gradient in order to mobilize a trapped oil blob as described below. See figure 2.12. In order for the blob to pass through the throat, the pressure drop across the leading edge must be greater than the entry pressure or the displacement pressure of the pore throat.

$$P'_b - P_B \geq \frac{2\sigma \cos \theta}{r_t} \quad (2.13)$$

In this model, the throat is assumed to have a circular cross-section. From the Laplace equation, we can calculate the capillary pressure across the trailing interface.

$$P'_a - P_A = \frac{2\sigma \cos \theta}{r_b} \quad (2.14)$$

The next step is to subtract equations 2.13 and 2.14. Rearranging the terms gives an equation for the required pressure difference in order to mobilize the oil blob. See equation 2.15 (Peters, 2012).

$$P_A - P_B \geq 2\sigma \cos \theta \left(\frac{1}{r_t} - \frac{1}{r_b} \right) \quad (2.15)$$

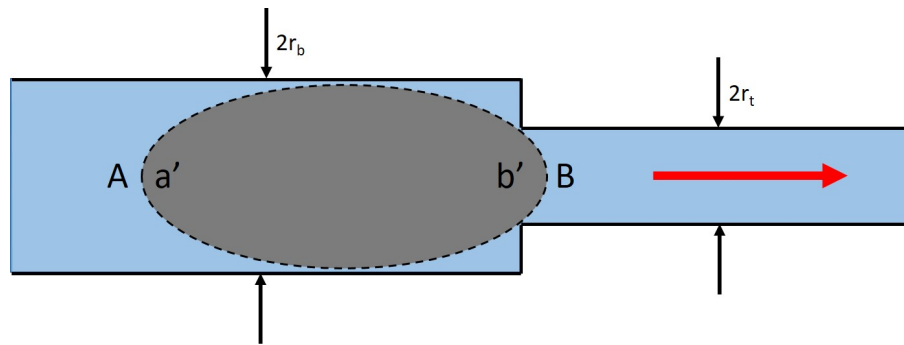


Figure 2.12: Illustration showing the mobilization of a trapped ganglion of nonwetting fluid in an idealized pore model. The red arrow shows the direction of flow.

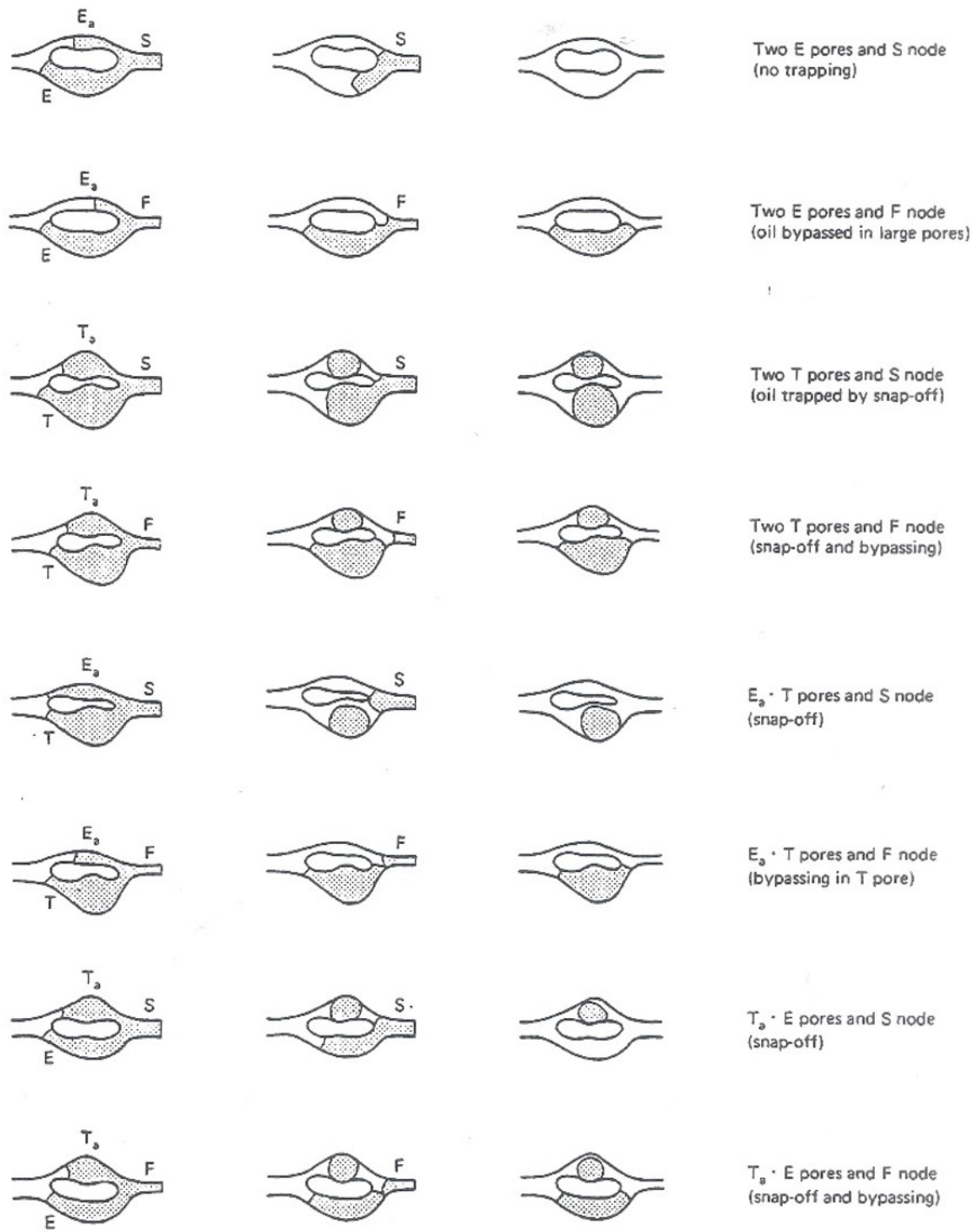


Figure 2.13: Sketches of low number trapping mechanisms and configuration of residual oil in doublets (Chatzis and Dullien, 1983). **E** is a pore with out trapping, **T** stands for trapping by Snap-off. **S** is for a stable interface downstream (no trapping). **F** means that a downstream node fills. **subscript O** means that a certain node traps first.

3

Capillary numbers and capillary desaturation curves

Now that the theory behind capillary transport, trapping of the residual phases and mobilizations is known, it is now time to introduce capillary numbers. This chapter consists of two parts. In the first part, a number of the most common conventional definitions of the capillary numbers that are used for calculating the mobilization of the trapped nonwetting phase inside porous media are described. In the second part of this chapter, I will explain how capillary numbers are used in combination with capillary desaturation curves for the analysis of the mobilization of the trapped nonwetting phase.

3.1. Capillary Numbers

When analyzing oil displacement by water in porous media, we must take into consideration the viscous forces, capillary forces and the geometry of the porous medium (Moore and Slobod, 1954). During two-phase flow in porous media, there is a strong competition between viscous and capillary forces in the rock matrix, which can be expressed by the capillary number (Al Quaimi and Rossen, 2017; Moore and Slobod, 1954). The capillary number is a dimensionless number that is characterized by the ratio of viscous forces to the capillary forces, as shown in equation 3.1 (Sheng, 2011; Jeong and Corapcioglu, 2003). In equation 3.1 the capillary number is denoted by N_{ca} , whilst the viscous forces and the capillary forces are given by F_v and F_c , respectively.

$$N_{ca} = \frac{F_v}{F_c} \quad (3.1)$$

The capillary number can be used to predict and determine the phase distribution and mobilization of the trapped nonwetting phase (Jeong and Corapcioglu, 2003). Over the years, a variety of different capillary numbers have been derived. In this chapter, I will introduce two of the most common ones and describe their defects with respect to this research. Moore and Slobod (1954) defined the capillary number as follows.

$$N_{ca} = \frac{u\mu}{\sigma \cos \theta} \quad (3.2)$$

In equation 3.2, u is the Darcy velocity and μ is the viscosity of the displacing fluid (wetting phase). σ is the interfacial tension between the wetting and nonwetting fluid, and θ is the contact angle measured through the wetting phase (Moore and Slobod, 1954). Another definition of the capillary number is given by Reed and Healy (1977). Their definition uses the pressure gradient and permeability of the porous medium. See equation 3.3.

$$N_{ca} = \frac{K\nabla P}{\sigma \cos \theta} \quad (3.3)$$

The permeability of the medium is given by K , and the pressure gradient is given by ∇P . These parameters can easily be obtained from Darcy's law for fluid flow through a porous medium. This definition follows from the fact that in order to mobilize a trapped ganglion of nonwetting fluid, the pressure

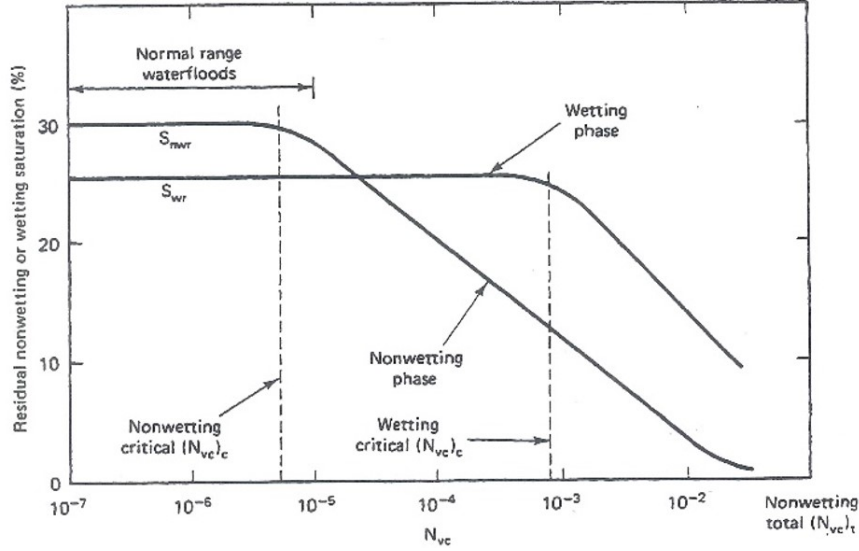


Figure 3.1: Typical capillary desaturation curve for both wetting and nonwetting residual phase saturations (Lake, 1989).

gradient across the trapped ganglion must be greater than the capillary pressure difference within the ganglion (Peters, 2012; Reed and Healy, 1977). In order to make the capillary number dimensionless, the permeability is included in the numerator of equation of the capillary number. The viscous term then becomes KVP .

The fact that this theory holds, can be derived from Darcy's law. Darcy's law is given by equation 3.4. This equation can be rewritten in such a way that $u\mu = KVP$. In this report, the effect of the relative permeability in two phase flow is ignored, see chapter 9. This means that the viscous forces in both Moore and Slobod (1954) and Reed and Healy (1977) should in theory have the same value.

$$u \cong \frac{K}{\mu} \nabla P \quad (3.4)$$

$$u\mu \cong KVP \quad (3.5)$$

Therefore, it holds that (Jeong and Corapcioglu, 2003)

$$N_{ca} = \frac{F_v}{F_c} = \frac{v\mu}{\sigma \cos \theta} \cong \frac{KVP}{\sigma \cos \theta} \quad (3.6)$$

3.2. Residual Saturations and Capillary Desaturation Curves

Now that the principles behind capillary trapping and mobilization of nonwetting phases are known, we can discuss the experimental observations of trapping in actual porous media. The most common observation is a relationship between the capillary number and the residual phase saturation. (see chapter 3.1) This relationship can then be presented in a so-called capillary desaturation curve (CDC), which plots the capillary number on a logarithmic x-axis and the residual phase saturation (S_{wr} or S_{nwr}) on the y-axis (Lake, 1989; Yeganeh *et al.*, 2016). Capillary desaturation curves are one of the most fundamental curves used for oil recovery, as it reveals the conditions for good oil displacement (Yeganeh *et al.*, 2016).

In figure 3.1, a schematic capillary desaturation curve can be seen. For low capillary numbers, the residual phase saturation remains at a constant level. Then, for a certain capillary number, the residual phase saturation starts decreasing. This point is called the critical capillary number, and is denoted by $N_{ca,c}$ (Lake, 1989). As can be seen in figure 3.1, the critical capillary number for nonwetting fluids is lower than that for wetting fluids in a water-wet system. This is due to the fact that in a water wet system, the wetting fluids tends to adhere to the grains that form the porous medium, thereby

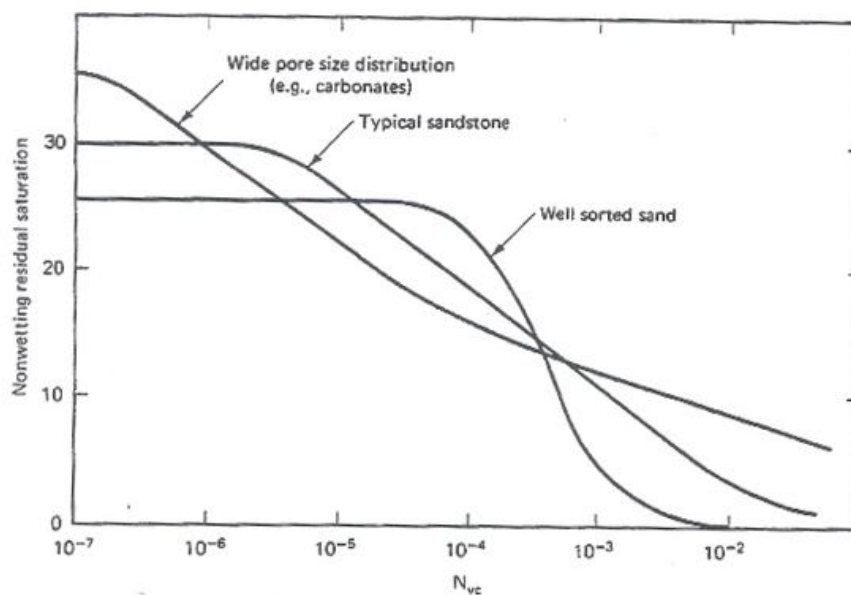


Figure 3.2: Capillary pressure curves for different geological rock types. Notice how the range between $N_{ca,c}$ and $N_{ca,t}$ increases as the pore sizes increase (Lake, 1989).

reducing the ability to be removed from the medium. Total capillary desaturation is not possible for the wetting fluid (see chapter 2.1 and figure 3.1). Complete desaturation for nonwetting fluid occurs at the total desaturation capillary number, denoted by $N_{ca,t}$.

Lake (1989) shows that there is considerable variation between parameters for different porous media. It is shown that for water-wet geological rock, the critical and total capillary number for nonwetting phases are lower (between 10^{-5} and 10^{-4} for $N_{ca,c}$, and 10^{-2} - 10^{-1} for $N_{ca,t}$) than the respective capillary numbers for the wetting phase, where the $N_{ca,c}$ lies roughly between 10^{-1} and 10^0 for the conventional capillary numbers presented by Moore and Slobod (1954) (See chapter 3.1). Based on these findings, (Lake, 1989) mentions three important factors that need to be taken into account when constructing a capillary desaturation curve:

1. Wettability is important. For a water-wet rock, the CDC curves for the nonwetting phase tends to be an order of 10^3 to the left with respect to the CDC curve of the wetting phase.
2. Pore size distribution is important. The range between $N_{ca,c}$ and $N_{ca,t}$ should increase with an increasing pore-size distribution for both the wetting and the nonwetting phases. See figure 3.2.
3. The range between the $N_{ca,c}$ and the $N_{ca,t}$ for the nonwetting phase should be greater than that for the wetting phase.

In our research, a number of capillary desaturation curves will be constructed by the use of published papers on capillary desaturation in micromodels. The way this is done is by imbibition of a wetting phase in order to mobilize and displace trapped non-wetting phase ganglions. Wetting fluids will be injected at a certain flowrate for which the capillary number can be calculated (See chapter 3.1). The wetting fluid will be injected at that particular flow rate until no further change in residual saturation can be observed. The residual saturation is determined and plotted. The next step is to increase the flow rate, thereby causing the capillary number to increase. The process is then repeated until a point close to irreducible nonwetting phase saturation has been reached.

4

New Capillary Number for Fractures

As described in chapter 1, the problem with the conventional capillary numbers is that they do not translate very well when they are applied to two-dimensional geometries. It is therefore not possible to describe the desaturation of trapped nonwetting phase by a single curve. In order to counter this problem, Al Quaimi and Rossen (2017) proposed a new definition of the capillary numbers in naturally fractured reservoirs based on a force balance across a trapped ganglion on a fracture. This project aims to find a similar capillary number describing the mobilization of trapped oil ganglions in 2D micromodels. In this chapter, the conventional capillary number for fractures is quickly described as well as the new definition of the capillary number as proposed by Al Quaimi and Rossen (2017). In the end, I show how the newly defined capillary numbers can be used to represent the desaturation of the nonwetting phase along a single curve. This is not the case for the conventional capillary number.

4.1. Conventional Capillary Number in Fractures

Hughes and Blunt (2001) analyzed multiphase flow in a single fracture using a pore network model. Based on this, they managed to generate a fracture model based on published aperture data, and they found an equation for capillary numbers for mobilization inside fractures. Their capillary number is defined as follows:

$$N_{ca} = \frac{Q\mu_w}{\hat{d}bN_y\sigma} = \frac{u\mu}{\sigma} \quad (4.1)$$

In this equation, Q is the volumetric flowrate, μ_w is the viscosity of the displacing fluid (the wetting fluid in this case.). \hat{d} represents the mean aperture of the fracture, b is the resolution (width of the pixels), N_y is the number of pixels and σ stands for the interfacial tension between the two phases (Hughes and Blunt, 2001). This definition is obtained from equation 3.2. The superficial (Darcy) velocity is replaced by the volumetric flowrate divided by the cross-sectional area (Al Quaimi, 2017). As explained in chapter 3, the main problem with the conventional equations for conventional capillary numbers is that the geometry of the porous medium is not taken into account. This means that the relationship between the capillary number and the residual nonwetting saturation cannot be expressed by a single trend (Al Quaimi and Rossen, 2017).

4.2. Derivation of New Capillary Number

In order to enable expressing the relation between capillary number and residual nonwetting saturation as a single trend, Al Quaimi and Rossen (2017) proposed to define a new capillary number based on a force balance across a trapped nonwetting ganglion. The Laplace equation for capillary pressure is given by

$$P_c = \sigma \left(\frac{1}{r_1} + \frac{1}{r_2} \right) \quad (4.2)$$

Al Quaimi and Rossen (2017) assumed that the length scale along which the aperture of the fracture varies in the fracture plane (see figure 4.1) is much greater than the variation in aperture itself. Also,

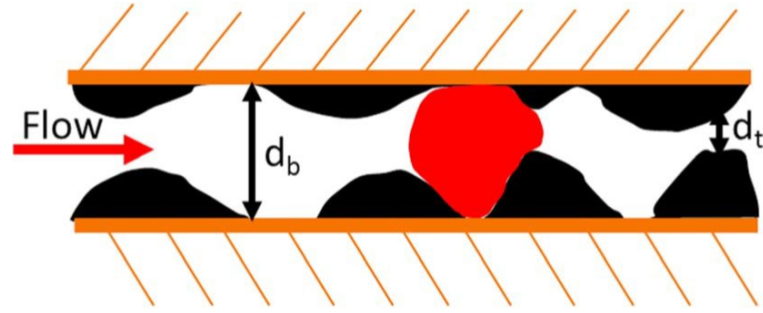


Figure 4.1: illustration of a fracture and a trapped nonwetting ganglion, greatly exaggerated in the vertical direction. d_t is the throat aperture and d_b is the body aperture (Al Quaimi and Rossen, 2017).

a fracture can be represented by a slit (Zimmermann and Bodvarsson, 1996). This means that the width in the plane of the fracture is much greater than the aperture of the fracture. This means that the interface is cylindrical rather than spherical. Therefore the principal radii of the interface within the fracture can be expressed as $r_1 = d / \cos \theta$ and $r_2 = \infty$ (Al Quaimi and Rossen, 2017). The Laplace equation for capillary pressure within a fracture can be now be expressed as

$$P_c = \sigma \left(\frac{1}{r_1} + \frac{1}{r_2} \right) = \sigma \left(\frac{1}{\frac{d}{2 \cos \theta}} + \frac{1}{\infty} \right) = \sigma \frac{1}{\frac{d}{2 \cos \theta}} = \frac{2 \sigma \cos \theta}{d} \quad (4.3)$$

where d is the aperture of the fracture. This is due to the fact that that one of the principal radii becomes infinite as the interface between the two phases within a fracture can be represented by a cylindrical geometry rather than spherical geometry. The maximum capillary pressure within a pore throat can therefore be expressed by

$$P_{c,t} = \frac{2 \sigma \cos \theta}{d_t} \quad (4.4)$$

and similarly for the pore body, the maximum capillary pressure within a pore body can be expressed by

$$P_{c,b} = \frac{2 \sigma \cos \theta}{d_b} \quad (4.5)$$

In Equations 4.4 and 4.5, d_t represents the aperture of the pore throat, and d_b the aperture of the pore body. The capillary pressure difference across a trapped ganglion can be represented by the difference between capillary pressure in the pore throat and pore body (see figure 4.1).

$$\Delta P_c = \frac{2 \sigma \cos \theta}{d_t} - \frac{2 \sigma \cos \theta}{d_b} = \left(\frac{2 \sigma}{d_t} - \frac{2 \sigma}{d_b} \right) \cos \theta \quad (4.6)$$

From chapter 2.4, it is known that in order to mobilize a trapped ganglion, the pressure gradient across the ganglion must be greater than the difference in capillary pressure within the ganglion. It therefore holds that

$$\nabla P L_g > \left(\frac{2 \sigma}{d_t} - \frac{2 \sigma}{d_b} \right) \cos \theta \quad (4.7)$$

where L_g is the length of the trapped ganglion. It is possible to regroup equation 4.7 as follows, to form a first expression for a capillary number that must be greater than one in order for mobilization to occur (Al Quaimi and Rossen, 2017).

$$\frac{\nabla P L_g d_t}{2 \sigma \left(1 - \frac{d_t}{d_b} \right) \cos \theta} \equiv N_{ca} > 1 \quad (4.8)$$

The next step is to include permeability into the equation. Al Quaimi and Rossen (2017) assumed that their fracture model can be approximated by a smooth slit geometry. In that case, the permeability of a fracture can be assumed by a function of the hydraulic aperture d_h (Tsang, 1992; Zimmermann

and Bodvarsson, 1996). More information on the relationship between permeability and the hydraulic aperture can be found in chapter 4.4.

$$K = \frac{d_h^2}{12} \quad (4.9)$$

Introducing equation 4.9 into the equation for the capillary number can be done via expanding the equation as follows:

$$\frac{L_g d_t}{1 - \frac{d_t}{d_b}} = d_h^2 \left(\frac{d_t}{d_h} \right)^2 \left(\frac{L_g}{d_t} \right) \frac{1}{1 - \frac{d_t}{d_b}} \quad (4.10)$$

And the equation for the capillary number therefore becomes

$$N_{ca} \equiv \frac{KVP}{\sigma \cos \theta} * \left(\left(\frac{12}{2} \right) \left(\frac{d_t}{d_h} \right)^2 \left(\frac{L_g}{d_t} \right) \frac{1}{1 - \frac{d_t}{d_b}} \right) \quad (4.11)$$

It can be seen that the first part of equation 4.11 is the conventional equation for the capillary number as expressed by Reed and Healy (1977). The second part of the equation accounts for the geometry of the fracture, pore bodies and pore throats. The value for the hydraulic aperture d_h can be derived from the permeability of the fracture using single phase flow experiments and Darcy's Law.

4.3. Experiments and Results

Al Quaimi and Rossen (2017) tested their capillary number by constructing five model fractures made of glass consisting of one flat smooth plate at the top and a rough plate on the bottom. First the hydraulic aperture is measured by single phase flow (Al Quaimi and Rossen, 2017). The pressure gradient was measured when steady-state had been reached, and the hydraulic aperture could be calculated using Darcy's Law.

The models were cleaned and fully saturated with air. Demineralized water (in order to prevent precipitation) is injected at a steady horizontal flow rate until a steady state situation has been reached. There should be no change in residual air saturation and the pressure gradient across the model should be stable for at least 15 minutes (Al Quaimi and Rossen, 2017). The residual air saturation is observed and measured using ImageJ software. A number of methods can be used in order to determine residual air saturation. Traditionally, area fractions were used, but Al Quaimi and Rossen (2017) developed two new methods: Image thresholding in order to determine the boundary of the ganglion, and the built in finding edges function in ImageJ. The difference between the two procedures is used as an error estimate. Furthermore, also the error in the pressure gradient was plotted, see figure A.1 in appendix A (Al Quaimi and Rossen, 2017).

Al Quaimi and Rossen (2017) used the experimental test results to calculate the capillary number using both the conventional definition (equation 3.3) and their new definition (equation 4.11). See figure A.2 and A.3 in appendix A. When comparing the results of the conventional capillary number (figure ref A.2) with the residual air saturation against the pressure gradient (figure ref A.1), it can be seen that the variation between the different models used is less in figure A.2 than that is for figure 4.2. However, the variation between the models still is an order of magnitude. If the newly defined capillary number is used, the relationship between capillary number and residual air saturation can be represented by a single curve (see figure A.3) (Al Quaimi and Rossen, 2017). These findings conclude that the new definition for capillary number based on a force balance across a trapped ganglion is better for representing the mobilization of the residual nonwetting saturation in a fracture, by using the geometric parameters of that fracture (Al Quaimi and Rossen, 2017). This report analyzes how a similar approach holds for the 2D micromodels.

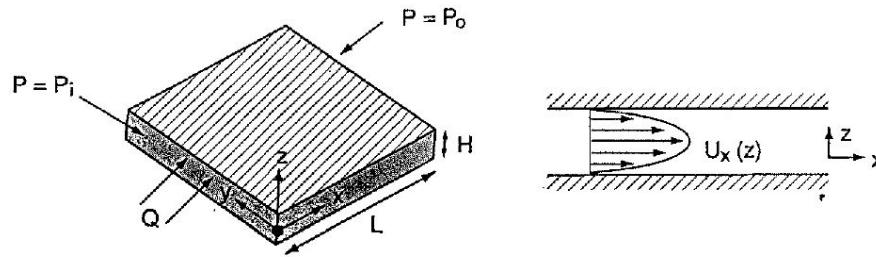


Figure 4.2: Illustration of a parallel plate model. On the left side, the dimensions and parameters of the model are shown. On the right, the parabolic velocity profile is shown (Zimmermann and Bodvarsson, 1996).

4.4. Relationship Between Permeability and Hydraulic Aperture

Al Quaimi and Rossen (2017) make the analogy that a fracture can be seen to be a smooth slit and that the relationship between permeability K and hydraulic aperture d_h is $k = d_h^2/12$. This relationship between permeability and hydraulic aperture can be found by analyzing the cubic law. The cubic law presents an analysis of flow through rock fracture by using the parallel plate model. This is the only model for which an exact calculation of the hydraulic conductivity is possible (Zimmermann and Bodvarsson, 1996). This section presents the derivation of the relationship between permeability and hydraulic aperture as presented by Zimmermann and Bodvarsson (1996) and Tsang (1992). This relationship is important because it will later be used in the derivation of the new definition of the capillary number for microfluidic devices.

Before we start we start analyzing the derivation of the cubic law, the Navier-Stokes equation is introduced. The Navier-Stokes equations are a set of equations used for describing the motion of viscous fluid substances. They arise when Newton's second law is applied to fluid flow. The flow of an incompressible Newtonian fluid is given by (Batchelor, 1967):

$$\frac{\partial \mathbf{U}}{\partial t} + (\mathbf{U} \cdot \nabla) \mathbf{U} = \mathbf{F} - \frac{1}{\rho} \nabla p + \frac{\mu}{\rho} \nabla^2 \mathbf{U} \quad (4.12)$$

\mathbf{F} is the body force vector acting on the fluid mass. \mathbf{U} is the velocity vector and p is the pressure component. On the left hand side of the equation, the first term represents the fluid acceleration. The second term is the advective acceleration term, which accounts for the fact that even in steady state flow, a particle may change its velocity. Together, these two terms represent the acceleration of a particle by following its trajectory. A complete derivation of the Navier-Stokes equation is given by Zimmermann and Bodvarsson (1996). They state that the equation for a fracture can be simplified to equation 4.13.

$$\mu \nabla^2 \mathbf{U} - \rho (\mathbf{U} \cdot \nabla) \mathbf{U} = \nabla P \quad (4.13)$$

The derivation of the cubic law starts with the assumption that the walls of a fracture can be represented by two smooth parallel plates. The plates are assumed to be infinitely large in the horizontal (x) and (y) directions. The spacing between these two plates is denoted by Zimmermann and Bodvarsson (1996) as H . The first step is to set up a Cartesian flow system, with the x direction parallel to the direction of flow, the y direction in the horizontal direction perpendicular flow and the z direction in the vertical direction. See figure 4.2. The coordinates of the top and bottom walls of the model correspond to $z = \pm H/2$.

In the derivation it is assumed that there is a uniform pressure gradient along the x direction of magnitude $(P_i - P_o)/L$, where L is the length of the model and $P_i - P_o$ is the difference in pressure across the model. This pressure gradient is also denoted by ∇P . Since the plates extend infinitely in the x and y direction, the geometry of the of the space between the plates does not vary with x or y . The flow velocity therefore only varies in the z direction (see figure 4.2) and we assume no-slip boundaries at the surfaces of the plates. Therefore, the flow velocity should be zero at the plate surfaces (Zimmermann and Bodvarsson, 1996). This means that the velocity vector of the Navier Stokes equation should necessarily vary in the z direction. The components of the vector $(\mathbf{U} \cdot \nabla) \mathbf{U}$ can

be written explicitly as

$$(\mathbf{U} \cdot \nabla)\mathbf{U} = (\mathbf{U} \cdot \nabla)(u_x, u_y, u_z) = [\mathbf{U} \cdot (\nabla u_x), \mathbf{U} \cdot (\nabla u_y), \mathbf{U} \cdot (\nabla u_z)] \quad (4.14)$$

The velocity components is constant for x and y . This means that any of the three velocity gradients that are not identically zero must be parallel to the z direction. The velocity vector however, is parallel to the x direction and perpendicular to the z direction. This means that all the components of the dot products in equation 4.14 become zero (Zimmermann and Bodvarsson, 1996). Hence the final Navier-stokes equation (equation 4.13) becomes:

$$\mu \nabla^2 \mathbf{U}(z) = \nabla P \quad (4.15)$$

As said before, ∇P lies parallel to the x axis. It can therefore be rewritten as

$$\nabla P = \left(\frac{\partial P}{\partial x}, \frac{\partial P}{\partial y}, \frac{\partial P}{\partial z} \right) = (\nabla P, 0, 0) \quad (4.16)$$

Looking at equation 4.16, it becomes evident that there are three velocity components, that must satisfy the following three equations:

$$\nabla^2 u_x(z) = \frac{\nabla P}{\mu} \quad (4.17)$$

$$\nabla^2 u_y(z) = 0 \quad (4.18)$$

$$\nabla^2 u_z(z) = 0 \quad (4.19)$$

Remember that the boundary conditions for this model are that the velocity must equal zero at the plate boundaries, thus $u_x = 0$ at $z = \pm H/2$. We can integrate equation 4.17 twice with respect to z . Keeping the boundary equations in mind, the following equation is obtained (Zimmermann and Bodvarsson, 1996):

$$u_x(z) = \frac{\nabla P}{2\mu} \left(z^2 - \left(\frac{h}{2} \right)^2 \right) \quad (4.20)$$

The next step is to determine the volumetric flux. For a fracture with width W in the y -direction, the volumetric flux is found by integrating equation 4.20 across the width of the fracture between $z = \pm H/2$ (Zimmermann and Bodvarsson, 1996).

$$Q_x = W \int_{z = -H/2}^{z = H/2} u_x(z) dz \quad (4.21)$$

$$Q_x = W \int_{z = -H/2}^{z = H/2} \frac{\nabla P}{2\mu} \left(z^2 - \left(\frac{h}{2} \right)^2 \right) dz = -\frac{\nabla P W H^3}{12\mu} \quad (4.22)$$

The volumetric flow is equal to the velocity multiplied by the cross-sectional area perpendicular to the flow direction (equation 2.7). Recall that the equation for Darcy flow velocity can be written as follows (de Marsily, 1986).

$$Q_x = u_x A = u_x * WH = -\frac{\nabla P H^2}{12\mu} * WH \quad (4.23)$$

$$Q_x = u_x * A = -\frac{K}{\mu} \nabla P * A \quad (4.24)$$

Combining equations 4.23 and 4.24, we can see that the permeability K of the fracture can be identified as $K = H^2/12$ (Zimmermann and Bodvarsson, 1996; Tsang, 1992). This approximation of the cubic law is derived for a parallel plate model. In order to use the cubic law to approximate real rock fractures, the aperture H can be replaced by the mean aperture or hydraulic aperture d_h (Zimmermann and Bodvarsson, 1996).

5

Derivation of New Capillary Number in Micromodels

From Chapter 4.3 it is known that a capillary number based on a force balance across a trapped ganglion is better for describing the mobilization of the trapped nonwetting phase in a fracture. The goal of this report is to find out whether a similar equation for the capillary number can be found that holds for 2D microfluidic devices. See chapter 6 for the description of the micromodels. In this Chapter, an equation for a capillary number in a 2D microfluidic device is derived. Similar to the equation for the capillary number derived by Al Quaimi and Rossen (2017), the equation will be based on a pressure difference across a trapped nonwetting ganglion. Also, the concept of tortuosity will be introduced, which helps to give the relationship between permeability and the depth of the model for the definition of the capillary number.

5.1. Force Balance on a Trapped Ganglion

The main difference between this new equation for microfluidic models compared to that of Al Quaimi and Rossen (2017) is the direction of variation in spacing. In their fracture model, the variation in spacing was in the z (vertical) direction, see figure 4.1. In this project, the variation in spacing will be in the y direction, and the widths of the throats and bodies will be denoted by w .

It is important to realize that when one looks at a cross-section of a microfluidic model, the pore throats and bodies can be seen as short rectangular ducts of in the plane of the micromodel having widths w_t and w_b respectively. The depth of the micromodel Z would be the depth of the duct. See figure 5.1. Lenormand *et al.* (1983) states that the capillary pressure in a duct of width w and depth z can be expressed by

$$P_c = F(\xi) * 2\sigma \left(\frac{1}{w} + \frac{1}{z} \right) \cos \theta \quad (5.1)$$

In this equation $F(\xi)$ is a correctional factor and is a function of ξ , which is the ratio between the width and the depth of the duct. Lenormand *et al.* (1983) states that $F(\xi)$ is always close to 1, regardless of the cross-sectional geometry of the duct. It is therefore assumed in this derivation that this term is 1. This means that $F(\xi)$ drops out of the equation.

Now Consider a trapped ganglion in a microfluidic model as shown in figure 5.2. The capillary pressures at both ends of a trapped ganglion, with its leading interface penetrating a pore throat of width w_t and the trailing in the pore body (width w_b) can therefore be expressed as:

$$P_{c,t} = 2\sigma \left(\frac{1}{w_t} + \frac{1}{Z} \right) \cos \theta \quad (5.2)$$

$$P_{c,b} = 2\sigma \left(\frac{1}{w_b} + \frac{1}{Z} \right) \cos \theta \quad (5.3)$$

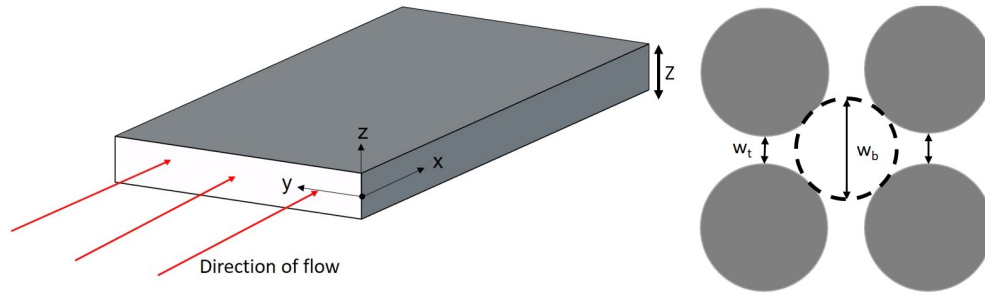


Figure 5.1: Model of a Microfluidic Device. On the left, the overview and the coordinate system. On the right, the parameters needed for the equation.

The difference in capillary pressure across the trapped nonwetting ganglion in figure 5.2 can be expressed by the difference in capillary pressure between the pore throat and the pore body.

$$\Delta P_c = 2\sigma \left(\frac{1}{w_t} + \frac{1}{Z} \right) \cos \theta - 2\sigma \left(\frac{1}{w_b} + \frac{1}{Z} \right) \cos \theta = 2\sigma \cos \theta \left(\frac{1}{w_t} - \frac{1}{w_b} \right) \quad (5.4)$$

Modern micromodels have a nearly constant depth across the entire length of the model. The assumption is made that for all the studied models (chapter 6) the depth within the model is constant. As can be seen in equation 5.4, the term Z , representing the depth of the microfluidic model, drops out. This is to be expected, since it is assumed that Z is constant across the model. From chapter 2.4, we know that in order to mobilize a trapped ganglion, the pressure gradient across the length of the ganglion L_g must be greater than the capillary pressure difference within the ganglion.

$$\nabla P L_g > 2\sigma \cos \theta \left(\frac{1}{w_t} - \frac{1}{w_b} \right) = \frac{2\sigma}{w_t} \cos \theta \left(1 - \frac{w_t}{w_b} \right) \quad (5.5)$$

The terms in equation 5.5 can be re-arranged in such a way that the criterion for mobilization can be stated as a capillary number.

$$\frac{\nabla P L_g w_t}{2\sigma \cos \theta \left(1 - \frac{w_t}{w_b} \right)} \equiv N_{ca} > 1 \quad (5.6)$$

The next step is to include the permeability into the equation. In order to do this, a relationship between the permeability and the depth of the micromodel needs to be found. In order to do so, a microfluidic device can be related to a smooth rectangular slit. Within a rectangular slit, the relationship between the permeability and the hydraulic aperture can be estimated by equation 4.9 (Al Quaimi and Rossen, 2017; Tsang, 1992; Zimmermann and Bodvarsson, 1996). However, in the case of microfluidic devices, the pillars within the model reduce the flow through the model. In order to describe this reduction in flow, a correction factor needs to be applied in the form of tortuosity (τ) (see chapter 5.2 below). The new relation between the permeability K and the aperture Z can now be expressed as

$$K = \frac{Z^2}{12} \tau \quad (5.7)$$

where τ is the tortuosity caused by the pillars in a micromodel. The equation for permeability can now be implemented into the equation of the capillary number.

$$\frac{L_g w_t}{1 - \frac{w_t}{w_b}} = Z^2 \left(\frac{w_t}{Z^2} \right)^2 \left(\frac{L_g}{w_t} \right) \frac{1}{1 - \frac{w_t}{w_b}} \quad (5.8)$$

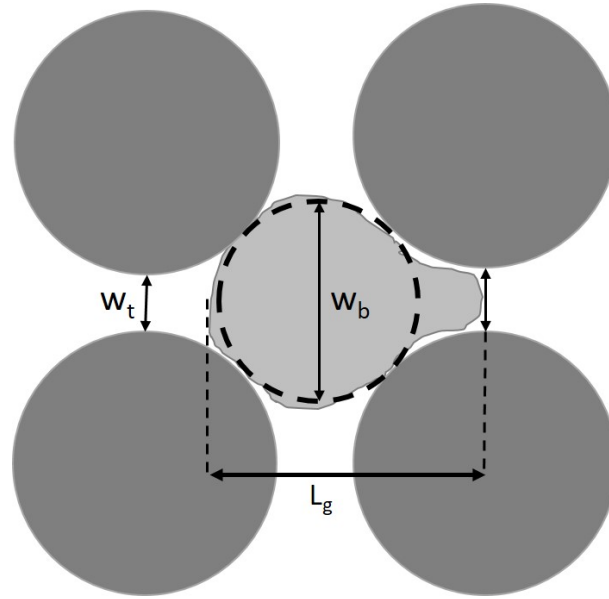


Figure 5.2: Illustration of a trapped ganglion in a simple geometry consisting of four circular, aligned pillars.

$$N_{ca} \equiv \frac{\nabla PK}{\sigma \cos \theta} * \left(\left(\frac{12}{2\tau} \right) \left(\frac{w_t}{Z} \right)^2 \left(\frac{L_g}{w_t} \right) \frac{1}{1 - \frac{w_t}{w_b}} \right) \quad (5.9)$$

The first part of equation 5.9 is the conventional capillary number as proposed by Reed and Healy (1977). The second part is the geometric term that accounts for the obstructions in the form of the pillars inside the microfluidic device, the width of the pore throats and bodies, distance between the two throats, and the ratio between the widths of the pore throats and bodies. The permeability of the microfluidic models is determined from single phase flow experiments and the Darcy equation. The fact that the permeability is approximated by relating the micromodel to an infinite slit with the same cross-sectional geometry (total width and depth) poses a contradiction. If the capillary number would be calculated for such a smooth slit, the following would happen to the capillary number. For an infinite, smooth slit, the value for w_t would become infinite and the value for τ would be 1. This means that for any pressure gradient applied to the system, the value for the capillary number would blow up to infinity.

Important is how the three geometrical parameters, w_t , w_b and L_g , are defined. The throat width is defined to be the narrowest constriction within the throat. Here, the capillary forces will have maximum effect. The pore body width is defined to be the diameter of the largest possible circle fitting within the pore body. Finally, the ganglion length is determined to be the distance between the pore throat (narrowest constriction) and the trailing edge of the pore body boundary. See figure 5.2.

5.2. Definition of Tortuosity

In the new derivation of the capillary number, we introduce the term of tortuosity (τ), in order to obtain a relationship between permeability and the aperture of the microfluidic devices. Peters (2012) describes tortuosity as a geometric property of the porous medium that reflects the length of pore flow at the pore level as fluid is forced around obstacles (grains/pillars) relative to the length of the flow path. This means that as the porosity of a porous medium decreases, the tortuosity must increase (Peters, 2012). Generally, tortuosity is a ratio that is used to characterize the convoluted pathways of fluid diffusion through porous media. Peters (2012) calculates tortuosity by taking two points on either side of a grain in a porous medium. Tortuosity is then the ratio of the tortuous path (L_e) over the shortest path (L_0) between the two points (Peters, 2012).

Tortuosity is often described by imagining the porous medium to be a bundle of capillary tubes that can give insight on the relationship between permeability and porosity (Bird *et al.*, 2014). Bird *et al.*

(2014) developed a theory where the capillary tubes are tangled. The idea is that the methods used to describe flow through straight capillary tubes can be used to describe flow behaviour in the crooked tubes as well. Bird *et al.* (2014) then state that in order to better describe the fluid diffusion inside the packed bed, and take the tortuosity of the capillary tubes into account, the equation for the friction factor (given by $f = 16/Re_n$) needs adjustments. They replace the term 16 in the equation for the friction factor by 100/3 as this value helps to better describe the fluid behaviour inside the porous medium (Bird *et al.*, 2014).

Analogous to the theory described by Bird *et al.* (2014), we can use this concept of tortuosity to our own research. We can assume that the flow through the microfluidic devices can be related to a smooth slit. We know from chapter 4 that the relationship between permeability and hydraulic aperture is $k = d_h^2/12$. However, in microfluidic devices, the pillars will make the flow path more tortuous. Therefore, we introduce the term tortuosity (τ). We define tortuosity for a micromodel to be the ratio of a cross-sectional area of a micromodel that is available for flow and the entire area of the cross-sectional area. This can be simplified into the following equation:

$$K = \frac{Z^2}{12} \tau \quad (5.10)$$

In this equation, K is the measured permeability of the microfluidic device, as can be measured using Darcy's equation. Z is the aperture of the model. If the first two parameters in the equations are known, so that the tortuosity (τ) can then be calculated.

6

Description of Various Micromodels

Now that we have defined our capillary number, its functionality must be tested. Due to time shortage, it was not possible to construct own micromodels and test them. Therefore it was decided that two-phase flow data from various sources would be analyzed. This way, the functionality of the capillary number based on a force balance across a trapped ganglion could be tested in a theoretical way. In total, nine different micro-models will be used, giving ten different experiments. They are obtained from various papers, which used them to analyze two phase flow in the micro-structures. It was preferred to analyze oil-water imbibition. In the end however, different wetting and nonwetting fluids were analyzed, because papers containing all the needed parameters were hard to come by. The used wetting fluids include water, brine and surfactant foams, and nonwetting fluids include oil and other non-aqueous phase liquids (NAPL). This chapter will start by elaborating on the background and the advantages of using micromodels in order to analyze two phase flow. Next, the obtained microfluidic models will be described including their geometry and permeability. The models used include both simple, regular geometries as well as more complicated geometries.

Over the last 30 years, micromodels have been extensively used to study the behaviour of fluid flow in microstructures. They have proven to be a valuable tool as they enable the observation the flow and transport of fluids inside the pore spaces. In this chapter, the background and advantages of micromodels are explained. Micromodels are idealized two-dimensional representations of porous media. They consist of a network of connected pores, including throats and bodies (Karadimitriou and Hassanizadeh, 2012; Jeong and Corapcioglu, 2003). They are typically made of transparent material that enables visual observation. These materials usually include quartz or glass (Karadimitriou and Hassanizadeh, 2012). The pores are usually several tens to hundreds of microns wide through which the fluid is allowed to flow. For two-phase flow studies, such in this case, it is important that the pore throats are smaller than a millimetre wide. Otherwise, the capillary effect will be irrelevant (Karadim-

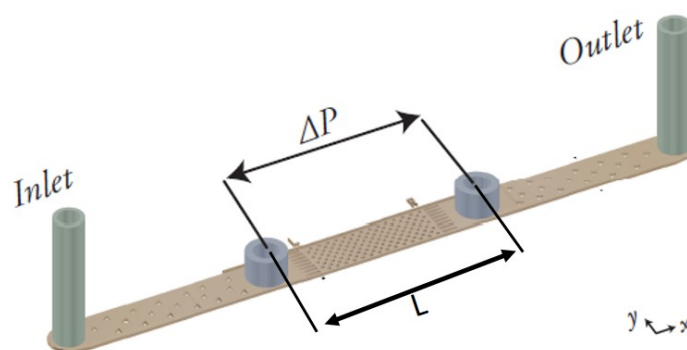


Figure 6.1: Typical set up of a micromodel (Kawale, 2017), the direction of depth is in the vertical direction.

itriou and Hassanizadeh, 2012).

See figure 6.1 for a typical micromodel setup. On either side of the micromodel, the model should be open, in order to allow the inlet and outlet of fluids. These inlets and outlets are usually combined with pressure sensors, so that the pressure drop across the model can be measured. Other models include syringes that allow for a precise flow rate through the model. Micromodels can consist of regular or irregular patterns, and anything in between. An excellent overview of the different geometric types and patterns in a micromodel is given by Karadimitriou and Hassanizadeh (2012).

The choice for a visualization method is essential to the outcome of the experiment. In a two-phase flow experiment, areas of interest include the average saturation of both the wetting and the nonwetting fluids and the specific interfacial area (Karadimitriou and Hassanizadeh, 2012). Since the micromodels are transparent, the easiest observation method is by photo or video analysis. Computer software can then be used to analyze the images and measure the saturation of wetting and nonwetting phases within the model. It is therefore important that the two fluids are distinguishable from each other. If necessary, dye needs to be applied to preferably the nonwetting fluid in order to increase the contrast (Karadimitriou and Hassanizadeh, 2012).

6.1. Simple Geometries by Kawale (2017)

Before analyzing more complicated micromodels, we will first take a look at simple geometries provided by Kawale (2017). These models all consist of regular patterns made up of either square or circular pillars. See figure 6.2. Table 6.1 summarizes the most important properties of the micromodels obtained by Kawale (2017). The length of the four devices is 8.5 millimetres and the width of the devices is 2.5 millimetres. The depth of the devices is a constant 120 microns with a variation of +/- 2 microns. The size of the pillars are constant in each of the devices, namely 262 microns with a variation of +/- 5 microns. That is the diameter of the circular pillars and the length of the square pillars. For the four models, the following four parameters are provided by Kawale (2017):

- Pore throat width (w_t);
- Number of pillars parallel (N_x) and perpendicular (N_y) to the flow direction;
- porosity (ϕ);
- Permeability given in Darcy (K).

Besides these properties, other properties that must be calculated include the pore body width (w_b) and the ganglion length (L_p). Below, each of the four micromodels is analyzed and the procedure of obtaining the geometrical parameters (w_b and L_p) is quickly summarized. Enlarged figures of the different models are available in Appendix B.1. They also include the dimensions used for calculating the model parameters that are not given by Kawale (2017).

The permeability of the devices was measured by injecting a total of three different Newtonian fluids. These three fluids were chosen such a way that the pressure drop was more than 5 percent than the operating range of the pressure sensor. If the pressure drop across the model was then determined, the permeability could then be calculated using Darcy's Law (Kawale, 2017).

$$K = \frac{\mu QL}{A\Delta P} \quad (6.1)$$

In this formula, μ is the viscosity of the fluid. Q is the flowrate, L is the length of the periodic array within the micro geometry. A is the cross-sectional area perpendicular to the flow path and ΔP is the pressure difference across the periodic array, measured by the two pressure sensors on either side of the micromodel (see figure 6.1).

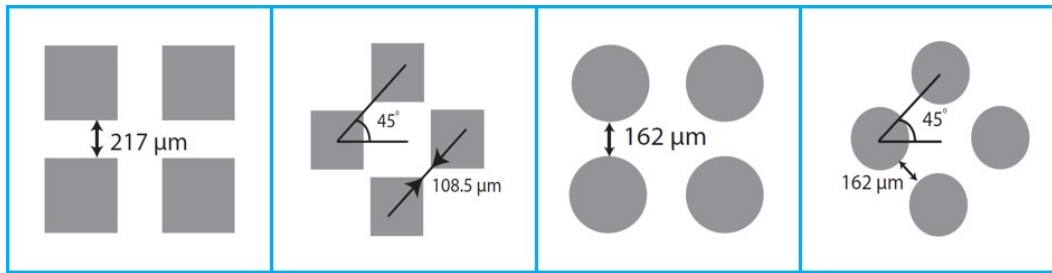


Figure 6.2: Geometries of the four models used by Kawale (2017), including a) aligned squares, b) staggered squares, c) aligned circles and d) staggered circles.

6.1.1. Squares, Aligned

The first model that will be analyzed is the aligned square model. See figure 6.2a and Table 6.1. The pore throat width (w_t) is 217.0 microns. This model contains 18 pillars in the x direction (parallel to the flow direction) and 6 in the y direction (perpendicular to flow). Furthermore, the permeability is stated to be 203.8 Darcy. See figure B.1 in Appendix B.1. The pore body width is taken by constructing the largest theoretically possible circle fitting within the pore body. The width of the pore body is simply the diameter of the imaginary circle and is equal to 307 microns. The ganglion length (L_g) defined to be from the point where the throat width is measured (narrowest point in a passage between two pores) to the trailing edge at the pore body boundary. Because the throat has a constant width in this model, the midpoint is taken for simplicity. For this model, that is 438 microns. See table 6.2.

6.1.2. Squares, Staggered

As can be seen in figure 6.2b, the staggered squares are placed at an angle of 45 degrees. The throat width is roughly half the size of the aligned squares, namely 108.5 microns. There are 17 pillars in the x direction and 10 in the y direction. The permeability is 180.0 Darcy. Due to the slightly more complicated geometry, the width of the pore body is a bit more complicated. Again, the pore body width is said to be the largest possible circle that would fit inside the pore body. After some geometrical calculations (see appendix B.2), we can find that the pore body width is 415 microns. The ganglion length for the model is defined as the distance between the pore throat and the trailing edge of the pore body boundary. For simplicity the largest possible L_g is taken by going diagonally across the pore body. See appendix B.1. The value for L_g is 447 microns.

6.1.3. Circles, Aligned

As can be seen in table 6.1, the pore throat width is 162 microns. There are 20 pillars in the flow direction and 6 in the parallel to flow direction. The permeability of the device is 214.1 Darcy. The pore body width is again the diameter of the largest possible circle that would fit inside the pore body. The pore body width is 338 microns. The length of the ganglion is determined to be the distance between the narrowest point in one pore and the trailing edge of the pore body boundary. For this model, that is 381 microns.

Table 6.1: Parameters of the microfluidic devices given by Kawale (2017).

Geometry	w_t	N_x and N_y	ϕ	K (D)
Squares, Aligned	217.0	18 & 6	0.69	203.8
Squares, Staggered	108.5	17 & 10	0.71	180.0
Circles, Aligned	162.0	20 & 6	0.71	214.1
Circles, Staggered	162.0	14 & 9	0.71	179.2

Table 6.2: The most important geometrical parameters used for the models of Kawale (2017).

Geometry	w_t (μm)	w_b (μm)	L_g (μm)	K (D)	$\phi(-)$	$\tau (-)$
Squares, Aligned	217.0	307	438	203.8	0.69	0.170
Squares, Staggered	108.5	415	447	180.0	0.71	0.150
Circles, Aligned	162.0	338	381	214.1	0.71	0.178
Circles, Staggered	162.0	338	381	179.2	0.71	0.149

6.1.4. Circles, Staggered

At last, there is the geometry of the staggered circles. For this geometry, the pore throat width is 162 microns. There are 14 pillars in the x direction and 9 in the y direction. The permeability is 179.2 Darcy. One can easily see that the geometry of the staggered circles is the same as the aligned circles, but at an angle of 45 degrees to the flow direction. This means that the pore body width is the same as for the aligned circles. The pore length is the largest distance between the pore throat and the trailing edge of the pore body, which is 381 microns.

The disadvantage of these models is that Kawale (2017) did not use them for two phase flow. Therefore, no desaturation data is available. However, the models can still be used to analyze theoretical flow rates and pressure drops across the model. The theoretical capillary numbers corresponding to each of the pressure drops can then be calculated and plotted. In order to do this, two fluids need to be selected for which the capillary number can be approximated. In this case, water is the wetting phase and kerosene is the nonwetting phase. The interfacial tensions between the two phases is 26 mN/m (Ibrahim *et al.*, 2008). For simplicity, perfect water-wet wettability is assumed for the models, so the contact angle is 0 degrees. The conventional and new capillary numbers will be plotted against an artificial pressure gradient that will be increased in a stepwise manner from 10,000 Pa/m to 270,000 Pa/m , to see how the variation between the magnitudes of the capillary numbers would differ for both the conventional and the new capillary number.

6.2. Hexagonal Geometry by Jones (2016)

A more complicated geometry was provided by Jones *et al.* (2016), see figure 6.3. The model was used for research into gas trapping in foam (Jones *et al.*, 2016). Surfactant foams (C¹⁴⁻¹⁶ Olefin Sulfonate, similar to the research conducted by Jeong and Corapcioglu (2003)) are used in this paper as the wetting phase and gas (air) represented the nonwetting phase. This model is also used by Getrouw (2016). The micromodel is a borosilicate glass model consisting of a hexagonal pattern of pore bodies. The model is made up by two glass plates. The upper plate has a thickness of 1100 microns whilst the bottom plate has a thickness of 700 microns. The hexagonal pattern of pores is etched into the lower plate using wet-etching. The inlet and outlet channels on either side of the model were created using power blasting. The plates were then sintered to each other by being heated to 600 °C Getrouw (2016).

The length of the pore channel is 60 millimetres. The width of the pore channel is 0.8 millimetres. The depth of the micromodel is only 5 microns (table 6.3). The total number of pores is estimated to be 849, with a Gaussian distribution in pore sizes. Five different pore sizes were distinguished throughout the model (Getrouw, 2016), ranging from 35 to 76 microns in diameter, with a mean diameter that is 60 microns. The mean diameter of the pore throats is 13 microns (Getrouw, 2016). The ganglion length for the model is determined using Image Analysis. The ganglion length was determined to be from halfway one pore throat across the pore body until the trailing edge of the pore body boundary directly across, see figure 6.3. From the image, a total of fifteen ganglion lengths was measured, and the average was determined to be the representative ganglion length, which is roughly 80 microns.

The porosity of the medium was determined by Getrouw (2016) by taking ten photos over the length

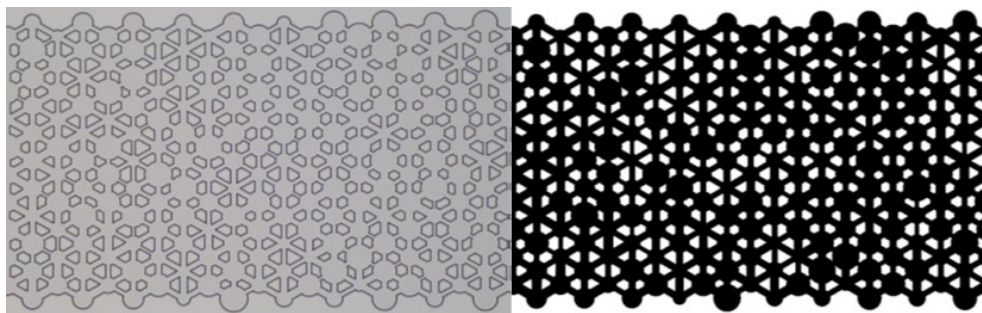


Figure 6.3: Micromodel used By Jones *et al.* (2016); Getrouw (2016). On the left, it shows the model as seen under a microscope. The figure on the right is the altered model for porosity characterization.

of the micromodel with 5 millimetre intervals. The photos were then converted to black and white images, so that the porosity could be determined using image analysis. The porosity is the fraction of black parts in figure 6.3. This was done for each of the ten images, and the average was then calculated. The porosity of the model is 0.71. The permeability was calculated by Getrouw (2016) by using single phase flow and the Darcy equation. The flowrate of water through the micromodel was increased in a step wise manner from $0.5 \mu\text{L}/\text{min}$ to $1.4 \mu\text{L}/\text{min}$. After a steady state had been reached, the pressure drop was then measured using pressure sensors on either side of the medium. The pressure drop was plotted against the flow rate, so that a trend line could be developed. Once the relationship between flowrate and pressure drop was determined, the permeability could be calculated by

$$K = \frac{Q\mu}{\nabla PA} \quad (6.2)$$

Now that the depth of the model, permeability and porosity are known, the tortuosity of the model can be calculated by equation 6.3. All parameters of the model can be found in table 6.3.

$$\tau = \frac{12K}{Z^2} \quad (6.3)$$

Jones *et al.* (2016) presents the desaturation of gas inside the model by plotting the trapped gas fraction against the superficial velocity. This plot can be found in appendix B.3 The superficial velocity has to be converted to a capillary number first. During this process, a problem is encountered because the viscosity of the surfactant is not constant. This is caused by the fact that the experiment performed by Jones *et al.* (2016) is somewhat different from the other experiments in the way the fluids work. Rather than using "conventional" wetting fluids for two phase flow, the wetting fluid is a "chain of bubbles" that show shear thinning behaviour, where the viscosity of the foam decreases for an increase in superficial velocity.

Table 6.3: Most important parameters for the model provided by Jones *et al.* (2016).

Micromodel	Jones <i>et al.</i> (2016)
Length (mm)	60
Width (mm)	0.8
Depth (μm)	5
Pore Body Width (μm)	60
Pore Throat Width (μm)	13
Ganglion Length (μm)	80
Porosity (-)	0.71
Permeability (m^2)	$7.2 \cdot 10^{-13}$
Tortuosity (-)	0.346

This means that the desaturation data presented by Jones *et al.* (2016) is not entirely fit to be used in this research. In order to still incorporate the micromodel and its geometry into this research, the micromodel is subjected to the same method as used for the methods by Kawale (2017). An artificial pressure gradient is applied to the model, to see the effect of both the conventional and the new definition of the capillary number. The fluids used are described in section 6.1

6.3. Geometries by Jeong *et al.* (2003)

Jeong and Corapcioglu (2003) used a micromodel in order to study the removal of groundwater contaminants from a porous medium with the use of surfactant foam (SF). In this study, the contaminants are the nonwetting phase and the surfactant foams are the wetting phase. Jeong and Corapcioglu (2003) used 2 models, with a similar, but not identical geometry. They will now be referred to as model A and B. A part of model A can be seen in figure 6.4. The most important physical properties of the two micromodels are listed in table 6.4.

The values for the pore throat width, pore body width and ganglion length were not directly given by (Jeong and Corapcioglu, 2003). The dimensions of the pore bodies and throats were measured by Jeong and Corapcioglu (2003) using image analysis. The pore distributions can be seen in Appendix B.3. The value for the throat radii and pore body radii were calculated as follows. First the frequencies for each pore or throat size were summed up, and then for simplicity, the mean values were calculated. The mean values are listed in table 6.4. The ganglion lengths for the models were determined using image analysis. Similar to the models of Kawale (2017), the ganglion length is defined as the length between the narrowest point in the pore throat up to the trailing edge of the pore body boundary. For this model, the throats between the pores have a near constant width. The midpoints of the throats is therefore taken. By image analysis, it was assumed that this is roughly 1.4 times the value of w_p . Since the models are very similar, the same ratio is assumed for model B.

The fluids used to represent the groundwater contaminants were trichloroethylene (TCE), a DNAPL and dodecane, a LNAPL. Proper desaturation data was only given by Jeong and Corapcioglu (2003) for the TCE. Therefore, we will focus on that fluid in this analysis. The displacement fluids used were water and surfactant foams. The used surfactant was an anionic surfactant, sodium C¹⁴⁻¹⁶ olefin sulfonate, and was diluted before use. The surfactant used in the end contained 2 percent sodium C¹⁴⁻¹⁶ olefin sulfonate on weight basis. The most important parameters of the used fluids are listed in Table 6.5.

The experiment conducted by Jeong and Corapcioglu (2003) began by fully saturating the micromodel with de-ionized water (in order to prevent precipitation). Then, dyed NAPL was injected using a syringe. The NAPL would saturate the micromodel until only residual water was left. This recreates actual porous media, since there will always be residual water left due to the wettability of the system. The

Table 6.4: Parameters of the microfluidic devices used by (Jeong and Corapcioglu, 2003).

Micromodel	Model A	Model B
length (mm)	64	59
width (mm)	40	42
Depth (μm)	130	130
Pore body width (μm)	330	270
Pore throat width (μm)	150	130
Ganglion length (μm)	456	380
Porosity (-)	0.27	0.28
Permeability (m ²)	$1.70 \cdot 10^{-11}$	$2.25 \cdot 10^{-11}$
Tortuosity (-)	0.0120	0.0159

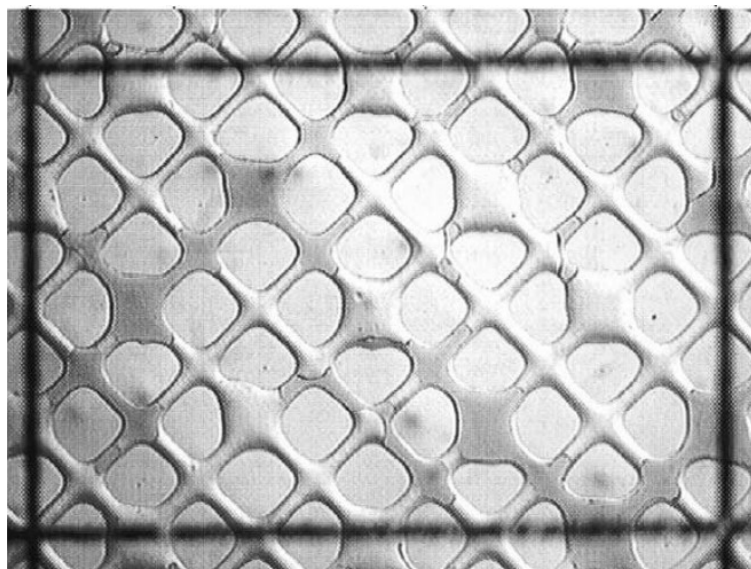


Figure 6.4: Enlarged image of Model A used by Jeong and Corapcioglu (2003). Note the example dimension of the ganglion length (L_g).

medium was then flushed with water again until only residual NAPL remained (Jeong and Corapcioglu, 2003). The residual saturations were 0.32 for TCE in model A, 0.53 for TCE in model B and 0.40 for dodecane in model A. Alternating slugs of surfactant solution and gas (air) were generated and inserted in the model in order to mobilize the residual NAPL. Jeong and Corapcioglu (2003) evaluated three different gas fractions (GF). The gas fraction is defined as the ratio of gas volume to surfactant volume. Increasing amounts of surfactant were injected and for each increment, the residual NAPL saturation was determined.

Jeong and Corapcioglu (2003) plotted the residual NAPL saturation against the conventional capillary number (see equation 3.3). We will analyze the desaturation of the TCE only, as it is the only fluid that gives results for both models. The residual gas saturation was presented as NAPL saturation ratio ($S_{tce}Ratio$). That is the ratio between TCE saturation after flooding and TCE saturation before flooding. In order to obtain the residual TCE saturation for each capillary number, the $S_{tce}Ratio$ must be converted by

$$Residual S_{TCE} = S_{TCE}Ratio * Res S_{TCE,0} \quad (6.4)$$

Where $Res S_{TCE}$ is the residual TCE saturation and $Res S_{TCE,0}$ is the residual TCE saturation after the initial water flooding, which is 0.32 for TCE desaturation in model A, and 0.53 for model B. Jeong and Corapcioglu (2003) started by analyzing the desaturation behaviour for different gas fractions, and found that the desaturation of TCE was more effective for a gas fraction of 66 percent than it was for 85 percent (Jeong and Corapcioglu, 2003). Therefore, the desaturation of the 66 percent surfactant was used in analyzing the desaturation between the two different micromodels. As said before, the

Table 6.5: Properties of chemicals used by Jeong and Corapcioglu (2003). IFT is interfacial tension. The contact angle is only measured for the TCE and is measured through the wetting phase. If the box is empty, the value is not given by Jeong and Corapcioglu (2003).

Chemical	IFT TCE (dyne/cm)	IFT dodecane (dyne/cm)	Density (g/cm ³)	viscosity (cpi)	Contact angle
TCE			1.47	0.59	
Dodecane			0.75		
Water	27.3	52.8	0.998	0.949	33
2% surfactant	4.9	2.6	1.004	1.029	50

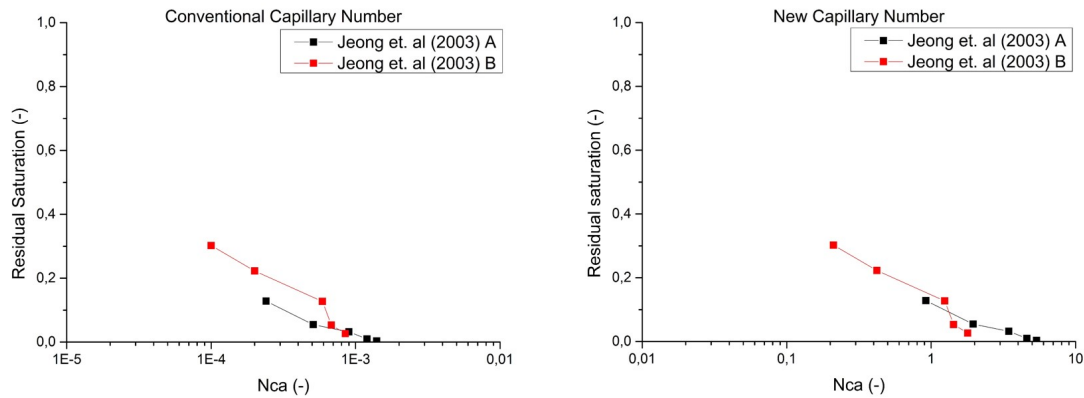


Figure 6.5: Capillary Desaturation Curves for the data obtained from Jeong and Corapcioglu (2003).

TCE saturation ratio must be converted to absolute residual saturation. The original desaturation data from the paper can be found in Appendix B.3. The corrected desaturation curves for the conventional capillary number for both models can be seen in figure 6.5. From the figures it is immediately clear that the residual TCE saturation's obtained from the experiments carried out by Jeong and Corapcioglu (2003) are very low. This means that this data is ideal for analyzing the functionality of the new capillary number for low residual saturations.

6.4. Ibrahim et al. (2008)

Ibrahim *et al.* (2008) present a paper in which they investigated the mobilization of residual oil inside microfluidic devices. The micromodel has a water-wet wettability and has varying pore throat and pore body size distribution. In the study, the attention is mainly focused on oil recovery by water flooding. De-ionized water is therefore used as a wetting fluid and dyed kerosene (red) was used to resemble the crude oil in the experiment.

Two different micromodels were studied by Ibrahim *et al.* (2008). One model will now be referred to as SRC-1, and the other model SX-4. The most important properties of the micromodels are listed in table 6.6. Proper throat sizes and pore body sizes were only given for SRC-1. Therefore, the analysis of this paper will focus on that model only. A portion of the SRC-1 model can be seen in figure 6.6. Exact values for the pore body and throat sizes were not directly given, as well as the values for the depth of the etching, ganglion length and porosity. Instead, these values were determined using image analysis of figure 6.6. We assumed that this portion of micromodel SRC-1 to be a representative sample for the entire model.

Chatzis (2011) used the same model, and stated that the pore throat size varied between 30 and 100 microns. This means that the largest pore throat should be 3.33 times wider than the narrowest in this model. Figure 6.6 was enlarged and the throat sizes were measured manually. The results of the measurements can be found in appendix B.4. It was found after measuring, that the smallest pore throat was 0.5 centimetres wide, and the widest was 1.7 centimetres wide. This gives a ratio of 3.4 which lies close enough to state that the widest pore throat in the figure resembles a throat of 100 microns, whilst the smallest throat in the figure resembles 30 microns. A linear scale was set up using the following equation:

$$Realsize = 58.333x + 0.8333 \quad (6.5)$$

Here, x is the width measured in the enlarged version of figure 6.6 in centimetres, and the actual width of the corresponding measurement is given in microns. All the throats in figure 6.6 were measured, and the average value was taken to be the pore throat width, which is 64 microns. The same scale could then be applied to the pore body sizes, since the scale holds for the entire figure. The pore bodies were measured both in the width and height direction in the figure. The average was taken to be the

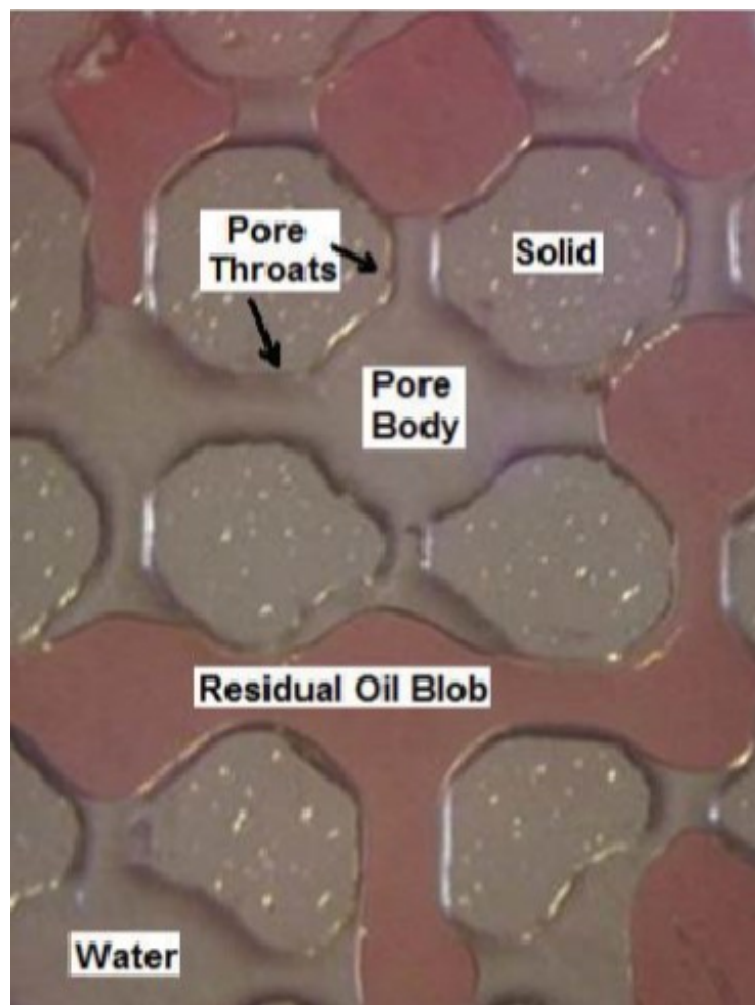


Figure 6.6: Sample from the SRC-1 model used by Ibrahim *et al.* (2008).

diameter of the pore body. The diameter of 10 pore bodies was measured, and the smallest diameter was taken to be the representing pore body width, which is 210 microns. The smallest diameter was taken since the definition of the pore body width is the diameter of the largest possible circle within the pore body. From figure 6.6, the ganglion length can also be measured and calculated using the same scale. The ganglion length for this model is determined similarly to the aligned circle model by Kawale (2017). From the narrowest point in one pore throat to the trailing edge of the pore body boundary. The measurements for all ganglion lengths can be found in Appendix B.4.

The next step is to measure the porosity of the model. We did this by calculating the surface area of each pillar in figure 6.6, and then take the sum of all the pillar areas. Also the entire surface area of figure 6.6 was calculated. The area available for flow is then the difference between the total surface area of figure 6.6 and the surface area of the pillars. The porosity is then simply calculated by:

$$\phi = \frac{A_{total} - A_{pillars}}{A_{total}} \quad (6.6)$$

In this equation, A_{total} is the total surface area of the sample and $A_{pillars}$ is the surface area taken up by the pillars. The last step in analyzing the geometry of the model is the depth. The depth is not directly given by Ibrahim *et al.* (2008). But we can approximate the depth of the model using equation 6.7. This equation is based on the relationship between permeability and depth given in equation 5.10. For this model, the depth and permeability from Jeong and Corapcioglu (2003) were taken, since the permeabilities for both models are similar. Now that the depth and permeability for the model by

Table 6.6: Most important parameters for the model provided by Ibrahim *et al.* (2008).

Micromodel	Model SRC-1	SX-4
Length (mm)	102	80
Width (mm)	44	46
Depth (μm)	140	
Number of pores	3567	
Total volume of medium (μL)	350	250
Pore Throat (μm)	64	
Pore body Width (μm)	210	
Ganglion Length (μm)	263	
Porosity (-)	0.495	
Permeability (m^2)	2.0×10^{-11}	2.3×10^{-11}
Tortuosity (-)	14.2×10^{-5}	

Ibrahim *et al.* (2008) are known, the tortuosity is easily calculated. See table 6.6.

$$\sqrt{\frac{K_1}{K_2}} = \frac{Z_1}{Z_2} \quad (6.7)$$

The fluids used by Ibrahim *et al.* (2008) are de-ionized water as the wetting phase and red-dyed kerosene as the nonwetting phase. The interfacial tension between the water and the kerosene is 26 mN/m, whilst in the case of using soap (surfactant) the interfacial tension is reduced to 3 mN/m. The porous medium is assumed to be perfectly water-wet, therefore the contact angle is 0 degrees, and $\cos \theta = 1$.

The first step in the experiment was to completely flush the model with water. The model was then oil-flooded to obtain a high initial oil saturation. Normal water flood residual oil saturation was then established by water injection at low flow rates. When equilibrium was reached, an image was taken of the model to determine the residual oil saturation. The water injection was then subsequently increased in a step wise manner, until at each flow rate, the equilibrium had been reached and the residual oil saturation had been determined.

The injected flow rates were converted to Darcy velocity by Ibrahim *et al.* (2008). The capillary numbers were calculated using the Moore and Slobod (1954) equation (see equation 3.2). The desaturation values were plotted against the capillary numbers. The pressures gradient across the model can be calculated by using equation 3.3. Also, the newly defined capillary number was calculated. The capillary desaturation curves for Ibrahim *et al.* (2008) can be seen in figure 6.7. The capillary desaturation curve has a large range and starts near complete nonwetting saturation and has its end at a residual saturation of 0.12. This means that the desaturation data by Ibrahim *et al.* (2008) is ideal for analyzing the functionality of the new capillary number for the complete desaturation progress.

6.5. Yeganeh *et al.* (2016)

As explained in chapter 1, Yeganeh *et al.* (2016) analyzed the desaturation of nonwetting phases in rock matrix using a similar approach by redefining the capillary number based on a force balance on a trapped ganglion. In order to test the functionality of this capillary number, Yeganeh *et al.* (2016) performed two experiments on a single micromodel using two different fluid combinations. The first being a de-mineralized water and hexadecane combination, the other a brine and crude oil combination.

The micromodel (figure 6.8) has total dimensions of 60 millimetres in length and 10 millimetres in

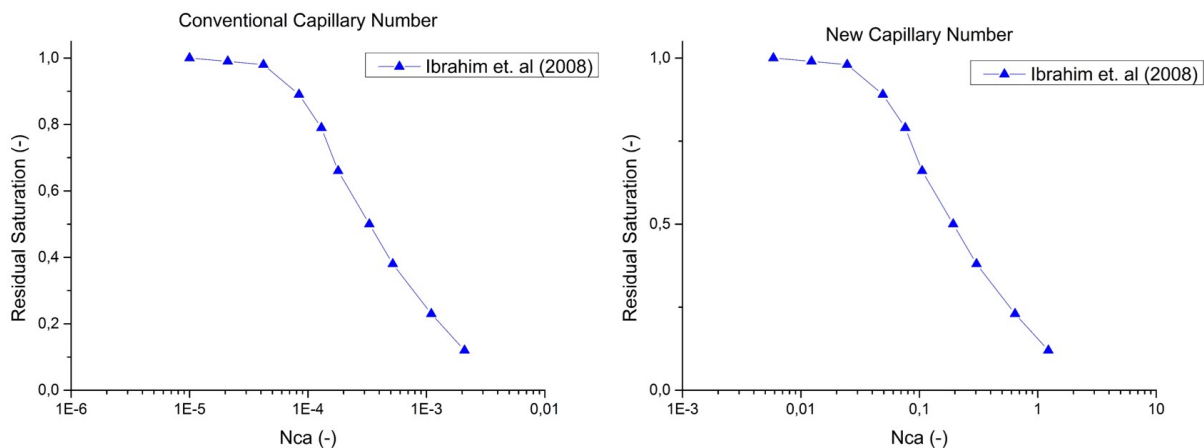


Figure 6.7: Capillary Desaturation Curves for Ibrahim *et al.* (2008) for both the conventional and the new capillary number.

width. The model consists of a total of 150 sub-cells, each having a dimension of 2×2 squares having 8×8 pillars per square (Yeganeh *et al.*, 2016). The pillars have a square shape, and have a width of 196 microns each (determined by image analysis of figure 6.8). The distance between the pillars is 110 microns. The spaces between the pillars have three different shapes (either straight, or with a constriction) resulting in a varying throat width of 63, 85 or a 110 microns. Yeganeh *et al.* (2016) state that the throat widths are randomly distributed across the model. By image analysis of figure 6.8, it was determined that the average throat width is 86 microns. Since the distances between the pillars is known, the pore body size can be calculated using the Pythagorean theorem (similar to the aligned squares model by Kawale (2017)). This way, the value for the pore body size was determined to be 156 microns. The ganglion length was determined to be the distance between the point of tightest constriction and the trailing edge of the pore body. This turned out to be 230 microns. See table 6.7. The depth of the model was not directly given by Yeganeh *et al.* (2016), however the cross-sectional area (A) was given, and the width of the model is known. The depth of the model is then equal to $Z = A/W$, where W is the width of the model.

The permeability of the model was not directly given by Yeganeh *et al.* (2016). It was possible to approximate the permeability of the model by using the relationship between the permeability and the depth of the model described in equation 5.10. The value for tortuosity is changed to be the ratio between the width available for flow in a throat and the total width of a pillar and a throat, so that it

Table 6.7: Properties of the micromodel used by Yeganeh *et al.* (2016).

Micromodel	Yeganeh <i>et al.</i> (2016)
Length (mm)	60
Width (mm)	10
Depth (μm)	110
Pore body width (μm)	156
Pore throat width (μm)	86
Ganglion length (μm)	230
Porosity (-)	0.585
Permeability	3.662×10^{-10}
Tortuosity (-)	0.359

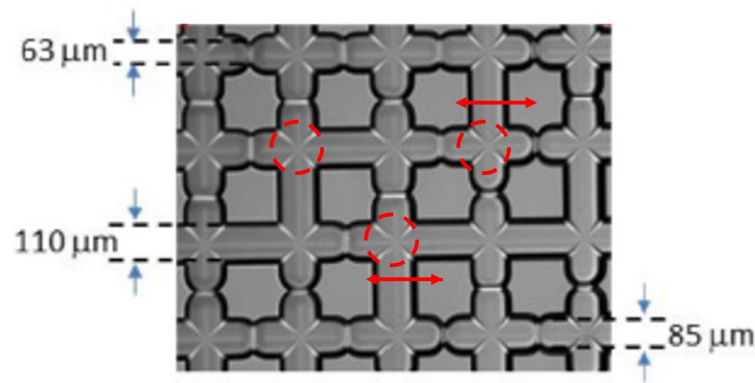


Figure 6.8: Micromodel used by Yeganeh *et al.* (2016). Dimensions of the three different throat widths are given. The dimensions of the pore bodies and ganglion lengths are given in red.

in a sense gives the fraction available for flow in the model. This gives the following equation:

$$K = \frac{Z^2}{12} * \frac{w_t}{w_t + w_{pillar}} \quad (6.8)$$

This approximation does not account for the fact that there is less drag by the walls in the pore bodies, and that there is more drag in the constrictions. In the end, this approximation gives an overestimation of the permeability of the model. In reality, the permeability will be lower.

As stated before, there are two combinations of fluids used in the experiment by Yeganeh *et al.* (2016). For the first experiment (referred to as experiment 1 in the figures), they used a demineralized water and hexadecane combination, with an interfacial tension of 1.7 mN/m . For the second experiment (referred to as experiment 2 in the figures), they used a brine and crude oil combination with a interfacial tension of 7.1 mN/m . In the appendix of the report, the contact angle between hexadecane and demineralized water is given to be 47 degrees (Yeganeh *et al.*, 2016). The contact angle between the crude oil and the brine is not directly given. The contact angle can vary greatly depending on the types of crude oil and brine (for example the different types of and concentration of the minerals present in the brine (Xie *et al.*, N D)). In this research, the contact angle for experiment 2 is assumed to be at least equal to that of experiment 1. See chapter 7 for more explanation on this subject.

The experiments begin by cleaning the model by flushing the model with water. The nonwetting phases are then injected until the model is fully saturated and only irreducible water remains, creating situations that are as natural as possible. The model is then flushed with the respective wetting phase

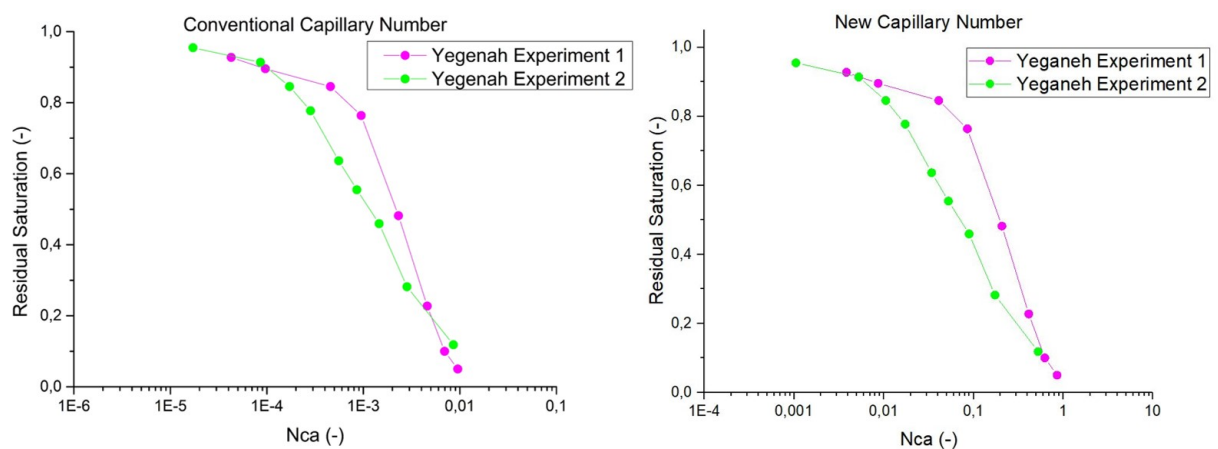


Figure 6.9: Desaturation curves for the data provided by Yeganeh *et al.* (2016).

at a certain flow rate until residual nonwetting phase saturations remain. The residual saturation is determined by image analysis. The flow rate is then increased in a stepwise manner, until irreducible nonwetting saturations are reached. The capillary desaturation plots are made for both experiments (see appendix B.5).

Yeganeh *et al.* (2016) use a different definition for the capillary number than the previously analyzed papers do. Their definition is given in equation 6.9.

$$N_{ca} = \frac{\mu_w Q}{\sigma A \phi} \quad (6.9)$$

It is possible to determine the flow rate since the values for the capillary number can be read from the capillary desaturation curves. Using Darcy's law, the flow rate can be converted to the corresponding pressure gradient across the model. It is then possible to calculate both the conventional capillary number as defined by equation 3.3 as well as the new capillary number. The capillary desaturation curves for the converted calculated capillary numbers for both experiments can be seen in figure 6.9.

Author	geometry	$L(mm)$	$W(mm)$	$Z(\mu m)$	$w_t(\mu m)$	$w_b(\mu m)$	$L_g(\mu m)$	$K(m^2)$	$\phi(-)$	$\tau(-)$
Kawale (2017)	Squares, Aligned				217	307	438	$2.04 \cdot 10^{-10}$	0.69	0.170
	Squares, Staggered	8.5	2.5	120	108.5	415	447	$1.80 \cdot 10^{-10}$	0.71	0.15
	Circles, Aligned				162	338	381	$2.14 \cdot 10^{-10}$	0.71	0.178
	Circles, Staggered				162	338	381	$1.79 \cdot 10^{-10}$	0.71	0.149
Jeong (2003)	Model A	64	40	130	152	326	456	$1.70 \cdot 10^{-11}$	0.27	0.012
	Model B	59	42	130	130	272	380	$2.25 \cdot 10^{-11}$	0.28	0.016
Jones (2016)		60	0.8	5	13	60	78	$7.20 \cdot 10^{-13}$	0.708	0.346
Ibrahim (2008)		102	44	150	64	210	263	$2.0 \cdot 10^{-11}$	0.495	0.011
Yeganeh (2016)		60	10	110	86	156	231	$3.62 \cdot 10^{-10}$	0.585	0.359

Table 6.8: An overview of all the properties of the micromodels presented in chapter 6. Author references are shortened in order to fit on the page (Kawale, 2017; Jeong and Corapcioglu, 2003; Jones *et al.*, 2016; Ibrahim *et al.*, 2008; Yeganeh *et al.*, 2016).

7

Analysis of Microfluidic Flow Data

Now that the selected micromodels are described (chapter 6), their desaturation data can be analyzed in order to test the functionality of the new definition of the capillary number. This chapter consists of four sections. In the first section, the models by Kawale (2017) and Jones *et al.* (2016) is tested for an artificial pressure gradient. Then, the presented desaturaton data will be analyzed for both the conventional and the new definition of the capillary number. At last, the role of permeability in the new definition of the capillary number will be analyzed.

7.1. Artificial Pressure Gradient for models by Kawale and Jones

In the first part of this chapter, the effect of the geometric term in the new definition of the capillary number will be tested for the models provided by Kawale (2017) and Jones *et al.* (2016). As explained in chapter 6, there is no (useful) desaturation data available for these models. However, it is possible to analyze how the variation between the different values for the capillary number changes if the conventional and the new capillary number are used. The assumed fluid properties are described in chapter 6.1. The different plots can be seen in figure 7.1. For the plot of the conventional capillary number, the plots of the staggered squares model and the staggered circle model are on one line, as they have nearly equal permeability (table 6.1). For the plot of the new capillary number, the aligned circle model and the staggered circle model share the same plot, as they have the same geometrical parameters (table 6.2).

As can be seen in figure 7.1, the variation between the capillary numbers for the four of Kawale (2017) models increases significantly if we change between the conventional and new capillary number. This is because the conventional capillary number does not take the geometry of the porous media into account. Therefore, the only varying parameter between the four models is the permeability. Regarding the model by Jones *et al.* (2016), the effect is the other way round. For the same artificial pressure gradient applied to the model, the conventional capillary number is a factor 250-280 smaller than for the models by Kawale (2017). This corresponds to the fact that the permeability for Jones

Table 7.1: Aspect ratios of the different micromodels.

Micromodel	Aspect Ratio (η)
Squares, Aligned	1.41
Squares, Staggered	3.82
Circles, Aligned	2.08
Circles, Staggered	2.08
Jones <i>et al.</i> (2016)	4.62

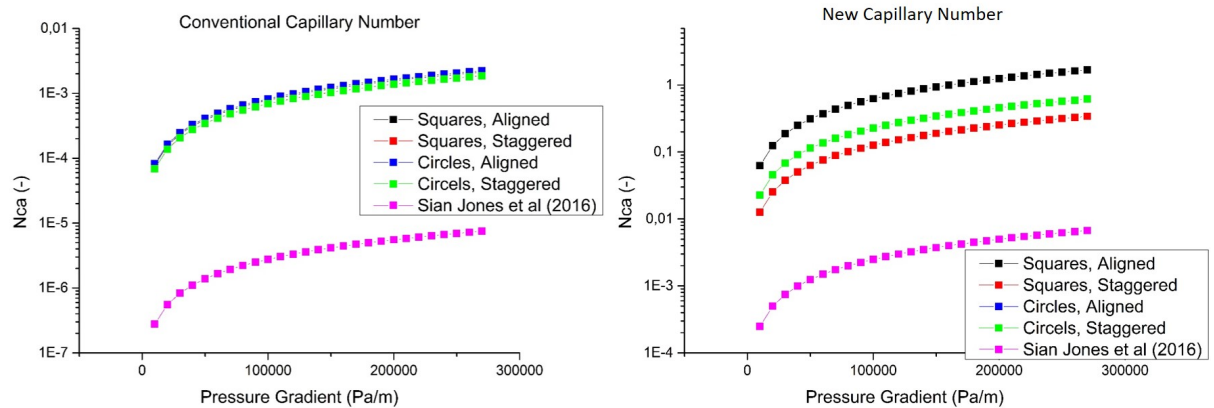


Figure 7.1: Pressure gradient against both the conventional and the new capillary number for each of the four models by Kawale (2017).

et al. (2016) is 250-280 times smaller than for the models of Kawale (2017). The new capillary number does account for the geometry of the porous media, meaning that it better describes the mobilization of trapped nonwetting fluids in more detail. This causes the variation for the models by Kawale (2017) to increase. The effect is the opposite for Jones *et al.* (2016). The variation between that model and those of Kawale (2017) decreases as the capillary number accounts for the geometry of the pores.

There seems to be a relationship between the aspect ratio (η) and the new capillary number. The aspect ratios of the five models are listed in table 7.1. When comparing the aspect ratios and the capillary number plot of the respective model, it becomes evident that the models with a lower aspect ratio have a higher capillary number, and the other way round. This suggests that the ratio between w_b and w_t has a significant effect on the mobilization efficiency. Mobilization efficiency would be greater for porous media with a low aspect ratio, as their capillary number is greater than it is for media with a high aspect ratio. However, desaturation data should be obtained in order to confirm this statement.

7.2. Desaturation Data for Conventional Capillary Number

From analyzing the data obtained using an artificial pressure gradient for the models provided by Kawale (2017) and Jones *et al.* (2016), there are indications that the new capillary number can actually better describe the desaturation process in microfluidic devices. To back this theory, some actual desaturation data has been analyzed. The data is obtained from papers written by Jeong and Corapcioglu (2003) (models A and B), Ibrahim *et al.* (2008) and Yeganeh *et al.* (2016) (experiments 1 and 2). First the desaturation data will be analyzed using the conventional definition of the capillary number, so that later the difference between the two definitions can be properly described. The desaturation curves for the conventional capillary number can be seen in figure 7.2.

If we compare the capillary desaturation curves using the conventional capillary number with the desaturation curve using the pressure gradient (appendix C.1), it can be seen that the variation between the curves becomes significantly less. Especially the curve for Ibrahim *et al.* (2008) shifts towards the other curves. If we compare the points of lowest saturation measured in each of the five models, we find that for figure C.1, the difference in pressure gradient between the outer most desaturation curves (Ibrahim *et al.* (2008) and Yeganeh *et al.* (2016) experiment 1) is almost two orders of magnitude. For figure 7.2, this is reduced to one order of magnitude (Yeganeh *et al.* (2016) experiment 1 and Jeong and Corapcioglu (2003) model B). Still the variation between the different trends is quite significant and it can be seen that five distinct desaturation curves develop for using the conventional definition of the capillary number. This is caused by the fact that the conventional capillary number takes differences in permeability into account, as well as differences in fluid types. Since these are all significantly different for each of the five analyzed experiments, one would expect five different curves to develop.

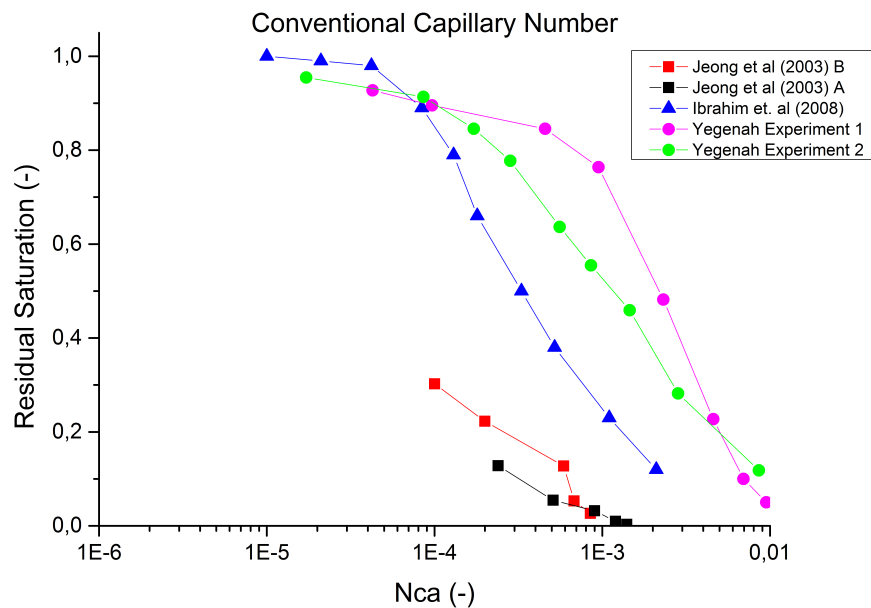


Figure 7.2: Capillary desaturation curves using the conventional capillary number for the five analyzed desaturation experiments by (Jeong and Corapcioglu, 2003; Ibrahim *et al.*, 2008; Yeganeh *et al.*, 2016).

From figure 7.2, it can be seen that desaturation processes for micromodels are significantly different than they are for geological rock. In chapter 3 it is explained that for most geological rock, the critical capillary number ($N_{ca,c}$) lies between 10^{-5} and 10^{-4} . In figure 7.2, it can be seen that the critical values lies near 10^{-3} . Continuing the lines for Jeong and Corapcioglu (2003) models A and B, suggests that their value for the critical capillary number lies around or even below 10^{-5} . Hence a larger variation for micromodels than for rock. This suggests that mobilization for micromodels differs from that for rock.

There seems to be a relationship between the permeability of the model and the magnitude of the capillary number. Models with a relatively higher permeability, generally also show a higher capillary number. This is easily explained by looking at equation 3.3, because N_{ca} is linearly dependent on K . This suggests that the conventional capillary number is dependent on the permeability. But also between the curves for the experiments conducted by Yeganeh *et al.* (2016), there is quite some variation, even though both experiments shared the same permeability. This suggests that the fluid properties also have a big influence on the magnitude of the conventional capillary number. Because the contact angle for the brine/crude oil combination is not directly given by Yeganeh *et al.* (2016), the contact angle was assumed to be at least the value of that for the hexadecane/water combination.

7.3. Desaturation for New Definition of Capillary Number

As explained in the previous section, even though the capillary number reduces the scatter between the five desaturation curves quite significantly, the difference between the lowest and highest capillary number at lowest saturation is still an order of magnitude. This is because the geometry of the micromodels is not taken into account. The capillary desaturation curves for the new definition are shown in figure 7.3. As can be seen, there is still some variation, for example the curve of Yeganeh *et al.* (2016) experiment 2 does not line up perfectly with the rest of the model. But overall, the plot is much cleaner than it is for the conventional capillary number. The capillary desaturation plot for Yeganeh *et al.* (2016) differs from the rest of the trend by much less than an order of magnitude. This further supports the claim that a capillary number that account for the geometry of porous media describes the mobilization of trapped residual nonwetting phases better than the conventional capillary number does.

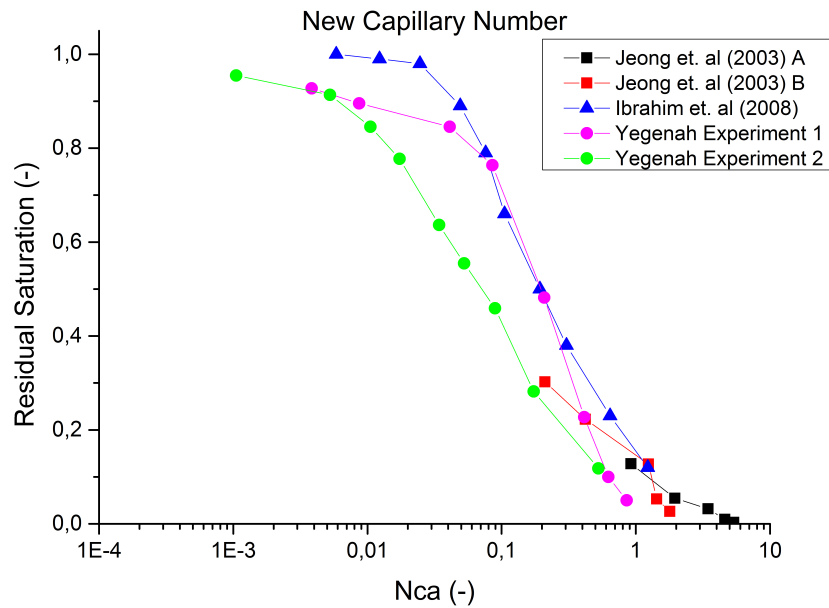


Figure 7.3: Capillary Desaturation curves for the newly defined capillary number for the models by (Jeong and Corapcioglu, 2003; Ibrahim *et al.*, 2008; Yeganeh *et al.*, 2016).

The desaturation of any micromodel can now be approximated by a single trend. The critical Capillary Number for the new capillary desaturation curve lies somewhere between 0.03 and 0.06, as can be seen in figure 7.3. The total capillary number lays somewhere between 5 and 6, where it can be seen that the curve of Jeong and Corapcioglu (2003) model A approaches zero nonwetting phase saturation.

7.3.1. Fluid Properties and the New Capillary Number

The interfacial properties of the wetting and nonwetting fluids play a significant role in the conventional capillary number. However, for the new capillary number, it does not appear to be so significant. As can be seen in figure 7.3, the desaturation curves of the four of the five analyzed experiment form a single trend regardless of the types of fluids or the wettability of the system. For example, Jeong and Corapcioglu (2003) analyzed two phase flow using a TCE/surfactant combination, which has an interfacial tension of 0.0049 mN/m , whilst the water/kerosene combination used by Ibrahim *et al.* (2008) has a interfacial tension 0.026 mN/m . That is a factor of 5.3 difference. The only curve that deviates from the rest of the main trend is experiment 2 by Yeganeh *et al.* (2016). As stated in chapter 6, the contact angle is not given for the brine/crude oil combination used in this experiment. It was assumed that the contact angle between the brine and crude oil was at least that of the hexadecane/water combination. In reality, the contact angle for crude oil/brine combinations can be as high as 60-70 degrees (Xie *et al.*, N D; Dos Santos *et al.*, 2006). See figure C.2 in Appendix C. The contact angle for experiment 2 is increased artificially from 47 to 70 degrees. This causes the magnitude for the capillary factor to decrease, resulting in a higher capillary number for a given pressure gradient. The desaturation curve shifts towards the right, where eventually it will align with the other desaturation curves. We now get five curves each having a different fluid combinations and interfacial properties that align to form one trend. This suggests that for describing the desaturation of micromodels, the geometry of the micromodel is more important than the interfacial properties of the wetting and nonwetting fluids for describing the recovery of trapped nonwetting phases. However, further experiments must be conducted to verify this statement. These experiments would include multiple two phase experiments performed on uniform micromodels using different fluid combinations.

7.4. Relationship Between Permeability and the Geometric Term

One of the key aspects of the new capillary number is the relevance of the permeability in the equation. Figure C.3 in Appendix C shows the permeability of the models plotted against the geometric terms (G). Also see table 7.2. One can see that there is a trend that shows that the higher the permeability of a model gets, the lower the geometric term becomes. The way this trend develops is explained as follows. During the derivation of the capillary number in chapter 5, equation 5.6 was expanded mathematically in order to introduce the permeability into the equation for the new capillary number. This way, the new capillary number could be expressed as a combination of the conventional capillary number (equation 3.3) and a geometric term (G) that accounts for the geometry of the micromodel. Since the permeability is introduced mathematically by expanding equation 5.6, it holds that

$$N_{ca} = \frac{\nabla PL_g w_t}{2\sigma \cos \theta \left(1 - \frac{w_t}{w_b}\right)} = \frac{KVP}{\sigma \cos \theta} * \left(\left(\frac{12}{2\tau\phi} \right) \left(\frac{w_t}{Z} \right)^2 \left(\frac{L_g}{w_t} \right) \frac{1}{1 - \frac{w_t}{w_b}} \right) \quad (7.1)$$

This suggests that for describing the mobilization of the nonwetting fluid, the parameters describing the geometry of the pores are more important than the permeability of the system. Also, it suggests that a simplified version of the new definition of the capillary number exists in the form of

$$N_{ca} \equiv \frac{\nabla PL_g w_t}{2\sigma \cos \theta \left(1 - \frac{w_t}{w_b}\right)} \quad (7.2)$$

Also, a relationship between the permeability and the depth of the micromodel was given by equation 5.10, where we introduced the concept of tortuosity. The tortuosity was defined as the ratio of the permeability of a micromodel and a smooth slit having the same horizontal cross-section. The tortuosity term was then included in the equation for the new capillary number. However, the tortuosity is introduced to account for the obstruction caused by the pillars inside the micromodels, and thereby correct the relationship between the permeability and the depth of the micromodel. The values for the tortuosity are listed in table 7.2. As can be seen, the values for the tortuosity vary greatly between the models, because the permeability is different by a order of 10 between the models by Kawale (2017) and Jeong and Corapcioglu (2003); Ibrahim *et al.* (2008).

Ideally, a better relationship between the permeability and the dimensions of the micromodel is derived. As explained in chapter 4, the relationship between permeability of a slit and its depth is based on the derivation of the Navier-Stokes equation. In this derivation, no-slip boundaries are assumed for the top and bottom plate for the slit, making depth the most important factor to determine the permeability. This works for well for infinitely wide slits, where there is no drag from walls in the y direction. For micromodels, the permeability is not only dependent on the spacing in the z direction.

Table 7.2: Tortuosity and the geometric (G) term for each micromodel.

Micromodel	G (-)	τ (-)	K (m ²)	Z (μ m)
Squares, Aligned	795.4	0.170	2.038*10 ⁻¹⁰	120
Squares, Staggered	182.4	0.150	1.800*10 ⁻¹⁰	120
Circles, Aligned	276.8	0.169	2.141*10 ⁻¹⁰	120
Circles, Staggered	330.7	0.149	1.792*10 ⁻¹⁰	120
Jeong and Corapcioglu (2003) A	3837.0	0.012	1.7*10 ⁻¹¹	130
Jeong and Corapcioglu (2003) B	2107	0.016	2.25*10 ⁻¹¹	130
Jones <i>et al.</i> (2016)	898.9	0.345	7.2*10 ⁻¹³	5
Ibrahim <i>et al.</i> (2008)	585.1	0.011	2.0*10 ⁻¹¹	150
Yeganeh <i>et al.</i> (2016)	61.3	0.359	3.622*10 ⁻¹⁰	110

The spacing in the bodies and between the pillars (throats) have a large impact as well. Therefore the vertical sides of the pillars also need to be assumed to be no-slip boundaries. This needs to be taken into account for whilst solving the Navier-Stokes equation. A better relationship for the permeability and the dimensions of the micromodels is obtained this way. This relation can then be taken up into the equation for the capillary number, such that the geometric term only accounts for the dimensions of the widths of the pore throats and bodies, and the lengths of the trapped ganglions.

8

Conclusion

A new definition for a capillary number for micromodels was derived based on a force balance on a trapped ganglion of nonwetting inside a micromodel. The new definition of the capillary number is a combination of the conventional capillary number as presented by Reed and Healy (1977) and a geometric term accounting for the geometry of the micromodel (G):

$$N_{ca} \equiv \frac{KVP}{\sigma \cos \theta} * G = \frac{KVP}{\sigma \cos \theta} * \left(\left(\frac{12}{2\tau\phi} \right) \left(\frac{w_t}{Z} \right)^2 \left(\frac{L_g}{w_t} \right) \frac{1}{1 - \frac{w_t}{w_b}} \right)$$

The geometric term is made up of six geometrical parameter of the model. Three terms are introduced via the force balance on the ganglion and describe the geometry of a single pore:

- w_b is the pore body width, and is defined as the diameter of the largest "circle" that would fit in the body of a pore.
- w_t is the pore throat width, and is defined as the narrowest part of the throat between two pore bodies.
- L_g is the length of the trapped ganglion, and is defined as the distance between the pore throat (narrowest part of the passage) and the trailing edge of the pore body boundary.

For simplicity, the average value for each of the above described parameters was taken over a number of measurements. Two other parameters are introduced using a relationship between the permeability and the depth of the model. This relationship was derived so that the permeability could be included into the new definition of the capillary number as part of the conventional capillary number. The geometric parameters introduced here are the depth of the model (Z) and the tortuosity (τ). The tortuosity is defined as the ratio between the permeability of a micromodel and the permeability of a smooth slit with the same cross-sectional area.

$$K = \frac{Z^2\tau}{12}$$

The new definition of the capillary number was then tested on a number of microfluidic desaturation data presented in different papers. The analyzed data were presented by Kawale (2017), Jeong and Corapcioglu (2003), Ibrahim *et al.* (2008) and Marchand *et al.* (2017). Since no proper desaturation data was available for the models of Kawale (2017) and Jones *et al.* (2016), the change in capillary number was projected using an artificial pressure gradient across the models. It was found that the difference in behaviour between the trends of the different models increased under the new capillary number. This is because the geometry of the model was taken into account. This already suggested that the new definition of the capillary number better describes the desaturation of nonwetting fluids inside micromodels. Also, it is suggested that there exists a relationship between the aspect ratio of the pores and the new definition of the capillary number. Models that have a higher aspect ratio (pores much wider than the respective throats) to have a lower capillary number for the same artificial

pressure gradient. It is expected that these models show less mobilization of the nonwetting phase. However, this will have to be verified by experimentation in the future.

Next, the desaturation data was analyzed and the pressure gradient was plotted against the capillary number and the capillary number was plotted against the residual saturation for both the conventional capillary numbers. It became apparent that the mobilization works differently for micromodels than it works for geological rock. The variation for the critical capillary numbers ($N_{ca,c}$) was much greater for the analyzed micromodels than it is for most geological rock (see chapter 3). The new definition of the capillary number does a better job describing the desaturation of the micromodels than the conventional definition. Where the conventional capillary number showed five different trends for each experiment, the new capillary number caused the different plots to form a near single trend, thereby proving its suitability to describe the mobilization of the trapped nonwetting phase, regardless of the geometry of the micromodel.

Also, the obtained plots suggested that the new definition of the capillary number works regardless of which fluids are used as the wetting and non-wetting phases. The analyzed data used various types of both wetting and nonwetting fluid. Nevertheless, the different desaturation plots still lined up. This suggests that the geometry of the porous media has a more significance in describing the mobilization of nonwetting fluids than the interfacial properties of the fluid have. However, further experiments will need to be conducted in order to support this statement.

The relationship between permeability and depth was introduced into the new definition by mathematical expansion. This way, The permeability can be included, and the new definition of the capillary number consists of a combination of the conventional capillary number and the geometry of the micromodel. Effectively, the value for the permeability is cancelled out in the geometric term. This suggests that the geometry of a single pore plays a bigger role in describing the mobilization than the permeability of the whole medium does. Despite the permeability being cancelled out in the geometric term, it is desired to have a better relationship between the permeability and the dimensions of the microfluidic model. This is because the permeability of a slit is dependent on spacing in the z direction, whilst in micromodels, the geometry of the pillars have an important effect on the permeability. Using a better relationship, the geometric term of the new capillary number can be better described and determine which parameters influence the mobilization progress. This includes deriving the Navier-Stokes equation for no-slip boundaries in both the y and the z direction.

9

Discussion

For the calculations of the capillary number in this report, several assumptions needed to be made. Especially during the process of analyzing the published desaturation data, several assumption needed to be made in order to properly use the data. In this chapter, the most significant assumptions made during the analysis and their effect on the capillary number will be discussed. Also, how these factors can be improved in order to improve the result of the report will be explained.

The biggest assumption made in this report in the definition of the geometrical parameters. The definition of the pore throat is uncomplicated by being the tightest constriction between two pore bodies. The body width is a bit more complicated by being the diameter of the largest possible circle that fits within the model. For most analyzed models, this does not pose a problem, as the sizes of the body are nearly equal in all directions. It will become more complicated however if the span of a pore body perpendicular to the flow direction is much greater than in the parallel direction. The ganglion length was determined to be the distance between the pore throat and the trailing edge of the pore body boundary. The value of this parameter can be determined much better by obtaining own desaturation data and measuring the ganglion length by image analysis.

For the models where the magnitudes of the pore bodies, throats and ganglion length were not directly stated (Ibrahim *et al.*, 2008), they were determined using image analysis of the enlarged figures of the models presented in the papers. It was assumed that the figures of the model were representative for the whole model. The average values were taken for the calculation of the capillary numbers. Performing own experiments would enable the possibility measure the geometrical parameters accurately and thereby increase the validity of the results.

Another assumption that was often made was the wettability of the models. Often, the capillary number was defined as $v\mu/\sigma$, and the contact angle was either not specified, or assumed to be zero 0 degrees by the authors. If the contact angle was not specified, two options were considered. The first option is to take a contact angle from other literature (for example the brine/crude oil combination in chapter 7). Or the contact angle was assumed to be zero, in order to obtain a maximum possible capillary factor in the equation for the capillary number. If the contact angle is increased, the magnitude of the capillary factor decreases, and therefore the capillary number would increase. This would cause the desaturation curves to shift to the right on the desaturation figures. Performing own experiments allow for precise measurement of the interfacial properties, thereby increasing the validity of the results. This can also help to verify the suggestions that the new capillary number gives a single trend regardless of the fluids used, as the geometrical parameters are more important than the interfacial properties.

Also, the depth of the model by Ibrahim *et al.* (2008) was not directly given. There were two ways that the depth could be approximated for the model. The first way was by using image analysis and the total pore volume. By image analysis, the fraction of pore body volume per total volume could be estimated (subtracting the pore throat volumes). Using the total number of pore bodies, the pore volume per pore body could be calculated. By image analysis, the pore body width was known, so the

average pore body surface area can be calculated. Using the volume per body and the body area, the depth of the body was calculated. However, this gave depth of well over a millimetre, which seemed very unlikely given the magnitudes of the pore-bodies and throats. A different approach was taken by comparing the model to another model. It was found that the parameters for permeability and porosity were very similar to model A by (Jeong and Corapcioglu, 2003). The relationship established between permeability and model depth was used to approximate the depth of the model (see equation 5.10) assuming the same tortuosity.

For the model by Yeganeh *et al.* (2016), the permeability was not given by the authors. Therefore, it was approximated using the relationship between depth and permeability, and using the tortuosity, the permeability could be estimated. The estimated permeability was an overestimate, meaning that the actual permeability of the medium is lower. Also, the viscosity of the displacement brine is not given. Therefore, the viscosity was assumed to be a low grade brine at room temperature was assumed giving a viscosity of 1.9 *cpi*. However, knowing the viscosity of the brine would not have made a significant difference as the pressure gradient will not change, and thus the magnitude of the capillary number will not change.

In the process of this research, also the effect of relative permeability was neglected, for simplicity purposes. Relative permeability is the ratio of effective permeability of one the two fluids at a particular saturation to absolute permeability if the model is fully saturated. Calculating the relative permeability of the wetting and nonwetting phases in the micromodels allows for better calculations of the capillary number, as the presence of more than one fluid inhibits the ability to flow. Higher pressure gradients may therefore be needed to reach similar desaturation levels, which results in higher magnitudes of the capillary number.

10

Recommendations for Future Study

Despite having obtained positive results regarding the suitability of the new definition of the capillary number for describing the mobilization progress, there are still a number of points where this research can be improved upon. They will be described here.

First of all, no new experiments were performed during this research. This meant that there was no control over the gathering of the desaturation data. Preferably, a number of micromodels with various geometries would have been produced and desaturation of a nonwetting fluid would have been done experimentally. This way, the properties of the new capillary number, such as the influence of the aspect ratio, could have been verified. Also, the experiments could have included multiple applications of the same model using various wetting and nonwetting fluid combinations in order to verify the earlier statements that the new definition of the capillary number is more dependent on the geometry of the porous media than it is on the types of fluids used in the experiment.

It was already mentioned in chapter 7, a better relationship between the permeability and the dimensions of the porous medium needs to be derived in order to improve the equation for the new definition of the new capillary number. In this report, a relationship between the permeability and the depth of a model is based on the relationship for a smooth slit. The term of tortuosity was introduced in order to account for the obstruction caused by the pillars in the model. The tortuosity was then also included in the definition for the new capillary number as part of the geometric term. In order to obtain a geometric term that is only determined by the dimensions of the pore structure, a new relationship for permeability and the dimensions of the model must be derived. This can be done by deriving the Navier-Stokes Equation (Chapter 4). During the derivation of the smooth slit, no-slip boundaries were assumed for the top and bottom plate of the slit (z direction). In the case of a microfluidic model, there are also no-slip direction in the y direction of the model. These must be taken into account when deriving the Navier-Stokes equation, and the equation can be derived by partial integration. If the obtained parameters are then included in the geometric term, it becomes possible to better analyze which parameters have a significant influence in the mobilization of the trapped nonwetting phase.

A similar condition for mobilization based on a trapped ganglion is derived by Ibrahim *et al.* (2008). They mention the concept that the contact angle at the front of the ganglion (advancing contact angle) is different from the contact angle at the rear of the ganglion (receding contact angle). In order to perfection the equation, this difference could be taken into account whilst deriving the equation of the capillary number. However, the equation for the capillary number could become unnecessarily complicated.

Two theories that are not included in this research are the percolation threshold and relative permeability. In this research, the average pore-body, throat and ganglion sizes were taken to be the geometrical parameters for simplicity reasons. Also, the intrinsic permeability of the medium was used. Including the percolation threshold and relative permeability, could allow for a better description of the mobilization of the nonwetting fluid. The percolation threshold is a measurement for describing the distribution

of pore sizes for complicated geometries. In abstract form, the percolation theory describes the morphology and conductivity of random structures (Larson *et al.*, 1980). Applying the percolation threshold could help to better describe more complicated geometries, as there is a useful measure for the geometrical factors of the micromodels. Also, Larson *et al.* (1980) found that the percolation theory was applicable to describe the saturation of nonwetting fluid inside porous structures. Larson *et al.* (1980) describe that there exists a critical value (percolation threshold) for which there exists a continuous conductive path across a porous medium, and that the residual saturation of nonwetting phases depends on this threshold. Relative permeability can be included in the Darcy equation to better describe the behaviour of two phase flow. Relative permeability is the ratio of effective permeability of one the two fluids at a particular saturation to absolute permeability if the model is fully saturated. Calculating the relative permeability of the wetting and nonwetting phases in the micromodels, allows for better calculations of the capillary number, as the presence of more than one fluid inhibits the ability to flow. Higher pressure gradients may therefore be needed to reach similar desaturation levels.

Bibliography

- B. I. Al Quaimi and W. R. Rossen, *New capillary number definition for displacement of residual non-wetting phase in natural fractures*, *Geophysical research letters* **44** (2017), 10.1002/2017GL073211.
- E. J. Peters, *Advanced petrophysics*, Vol. 2 (Live Oak Book Company, 2012).
- L. W. Lake, *Enhanced Oil Recovery* (Society of Petroleum Engineers, Austin, Texas, USA, 1989).
- I. Chatzis and F. A. L. Dullien, *Dynamic immiscible displacement mechanisms in pore doublets: Theory vs. experiment*, *Journal of Colloid and Interface science* **91**, 199 (1983).
- R. W. Zimmermann and G. S. Bodvarsson, *Hydraulic conductivity of rock fractures*, *Transport in Porous Media* **23**, 1 (1996).
- D. Kawale, *Elastic Instabilities in Polymer-Solution Flow Through Porous Media*, Ph.D. thesis, Faculty of Civil Engineering and Geosciences, Technical University Delft, Delft, Netherlands (2017).
- S. A. Jones, N. Getrouw, and S. Vincent-Bonnieu, *Foam flow in a model porous medium: Ii. the effect of trapped gas*, (2016).
- N. A. S. Getrouw, *The Static and Dynamic Behaviour of Foam in a Model Porous Media*, Ph.D. thesis, Delft University of Technology (2016).
- S. W. Jeong and M. Y. Corapcioglu, *A micromodel analysis of factors influencing npl removal by surfactant foam flooding*, *Journal of contaminant hydrology* **60**, 77 (2003).
- A. S. Ibrahim, N. S. Abdelfattah, and I. Chatzis, *Investigation of the mobilization of residual oil using micromodels*, (The Petroleum Institute, Petroleum Engineering Program, Abu Dhabi, U.A.E., 2008).
- M. Yeganeh, J. Hegner, E. Lewandowski, A. Mohan, L. W. Lake, D. Cherney, A. Jusufi, and A. Jaishankar, *Capillary desaturation curve fundamentals*, (Society of Petroleum Engineers, Tulsa, Oklahoma, USA, 2016).
- J. Sheng, *Modern Chemical Enhanced Oil Recovery* (Elsevier, Burlington, Massachusetts, USA, 2011).
- T. F. Moore and R. L. Slobod, *Displacement of oil by water-effect of wettability, rate, and viscosity on recovery*, (Society of Petroleum Engineers, Dallas, Texas, USA, 1954).
- R. L. Reed and R. N. Healy, *Some physico-chemical aspects of micro-emulsion flooding: A review*, *Improved Oil recovery by surfactant and polymer flooding* (1977).
- R. G. Hughes and M. J. Blunt, *Network modeling of multiphase flow in fractures*, *Advanced in Water Resources* **24**, 409 (2001).
- S. Datta, T. Ramakrishnan, and D. Weitz, *Mobilization of a trapped non-wetting fluid from a three dimensional medium*, *Physics of fluids* **26** (2014).
- W. Abdallah, J. S. Buckley, A. Carnegie, J. Edwards, B. Herold, E. Fordham, A. Graue, T. Habashy, C. Seleznev, N. Signer, H. Hussain, B. Montaron, and M. Ziauddin, *Fundamentals of wettability*, in *Oilfield Review*, Vol. Summer 2007 (Schlumberger, Houston, Texas, USA, 2007) Chap. 4, pp. 44–61.
- A. M. El Gendy, *Determination of Determination of irreducible water saturation*, Ph.D. thesis, Geophysics department, Faculty of Science, Ain Shams University, Cairo, Cairo, Egypt (2016).
- I. Chatzis, N. R. Morrow, and H. T. Lim, *Magnitude and detailed structure of residual oil saturation*, *Society of Petroleum Engineers Journal* **23** (1983).

- B. I. Al Quaimi, *Investigation of foam generation, propagation and rheology in fractures*, Ph.D. thesis, Technische Universiteit, Delft, Delft, Zuid-Holland, Netherlands (2017).
- Y. W. Tsang, *Usage of equivalent apertures for rock fractures as derived from hydraulic and tracer tests*, *Water Resources Research* **28**, 1451 (1992).
- G. K. Batchelor, *An introduction to fluid mechanics* (Cambridge University Press, New York, New York, USA, 1967).
- G. de Marsily, *Quantitative Hydrogeology* (Academic Press, San Diego, California, USA, 1986).
- R. Lenormand, C. Zarcone, and A. Sarr, *Mechanisms of the displacement of one fluid by another in a network of capillary ducts*, *J. Fluid Mech* **135**, 337 (1983).
- R. B. Bird, W. E. Stewart, E. N. Lightfoot, and D. J. Klingenberg, *Introductory Transport Phenomena* (Wiley, 2014).
- N. K. Karadimitriou and S. M. Hassanizadeh, *A review of micromodels and their use in two-phase flow studies*, *Vadose Zone Journal* (2012), 10.2136/vzj2011.0072.
- I. Chatzis, *Mobilization of residual oil mechanisms seen in micromodels*, (2011).
- X. Xie, N. R. Morrow, and J. S. Buckley, *Crude oil/brine contact angles on quartz glass*, (N. D.).
- R. G. Dos Santos, R. S. Mohamed, A. C. Bannwart, and W. Loh, *Contact angle measurements and wetting behaviour of inner surfaces of pipelines exposed to heavy crude oil and water*, *Journal of Petroleum Sciences and Engineering* **51**, 9 (2006).
- S. Marchand, I. Bondino, A. Ktari, and E. Santanach-Carreras, *Consideration on data dispersion for two-phase flow micromodel experiments*, *Transport in Porous Media* **117**, 169 (2017).
- R. G. Larson, L. E. Scriven, and H. T. Davis, *Percolation theory of two phase flow in porous media*, *Chemical Engineering Science* **36**, 57 (1980).



Results for Alquaimi and Rossen (2017)

This appendix contains the figures corresponding to the results obtained during the testing of the functionality of the new definition of the capillary number by Al Quaimi and Rossen (2017).

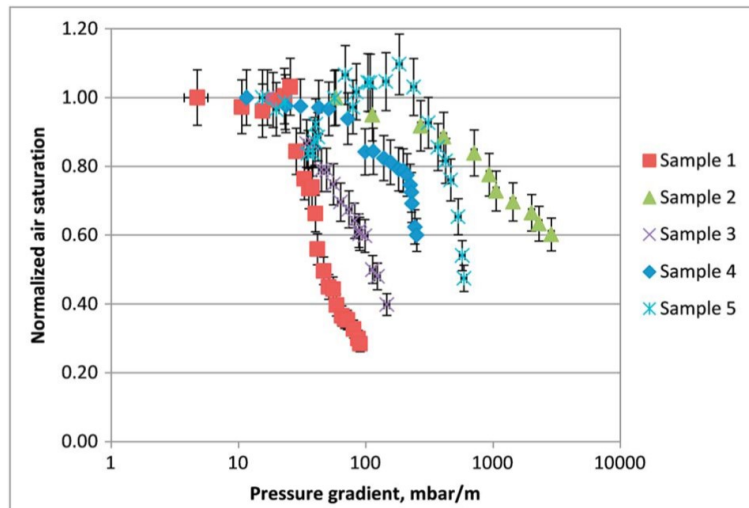


Figure A.1: Graph showing the relationship between pressure gradient and residual air saturation for the five models used in the research by Al Quaimi and Rossen (2017).

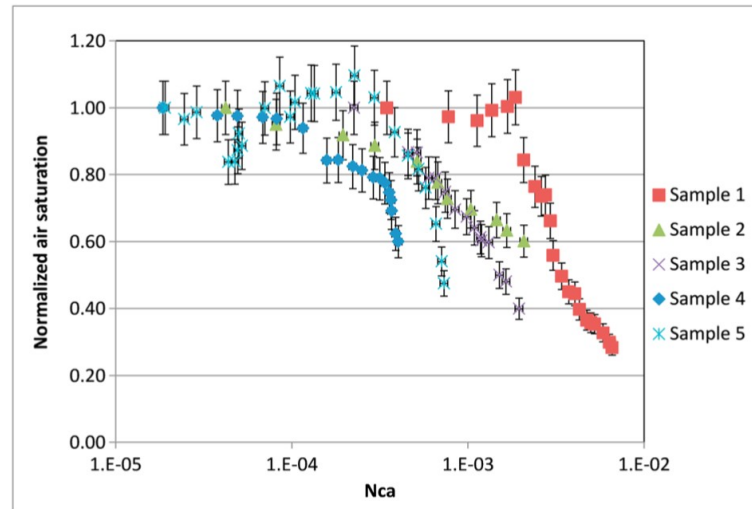


Figure A.2: capillary desaturation curves using the conventional capillary number (equation 3.3) for the five fracture models used by Al Quaimi and Rossen (2017). Notice how the curves do not follow a single trend (Al Quaimi and Rossen, 2017).

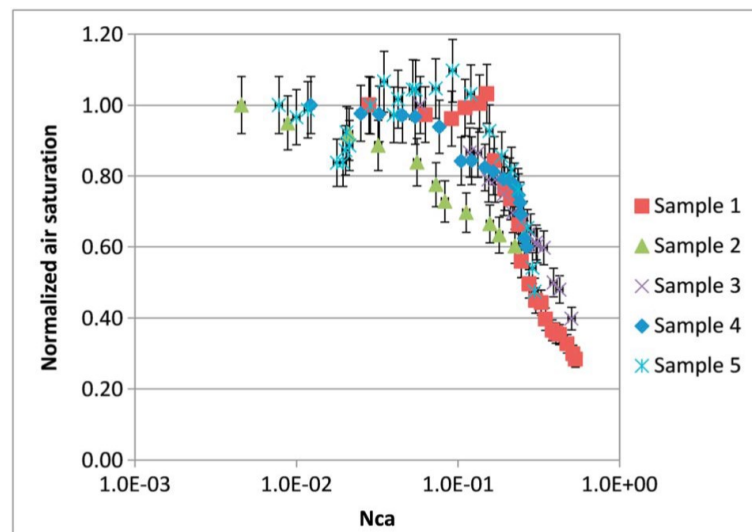


Figure A.3: Capillary desaturation curves for the newly defined capillary number based on a force balance across a trapped ganglion. Notice how the curves now follow a single trend (Al Quaimi and Rossen, 2017).

B

Additional Figures for Micromodels

This appendix contains the additional figures for chapter 6

B.1. Simple Geometries by Kawale

This appendix contains extra information on how the parameters for w_t , w_b and L_g were calculated for each of the four models provided by Kawale (2017). The figures are not to scale.

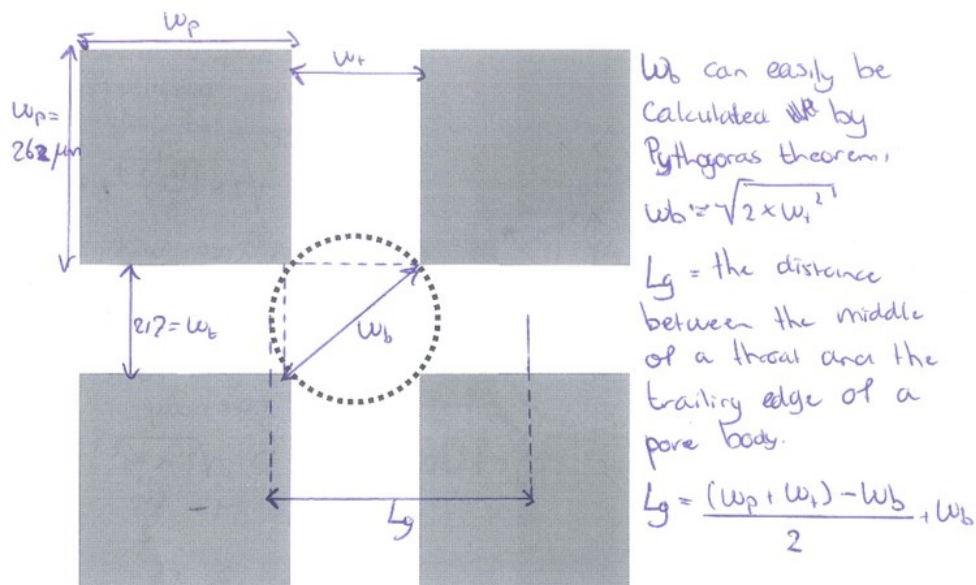


Figure B.1: Parameters of the Aligned Squares model.

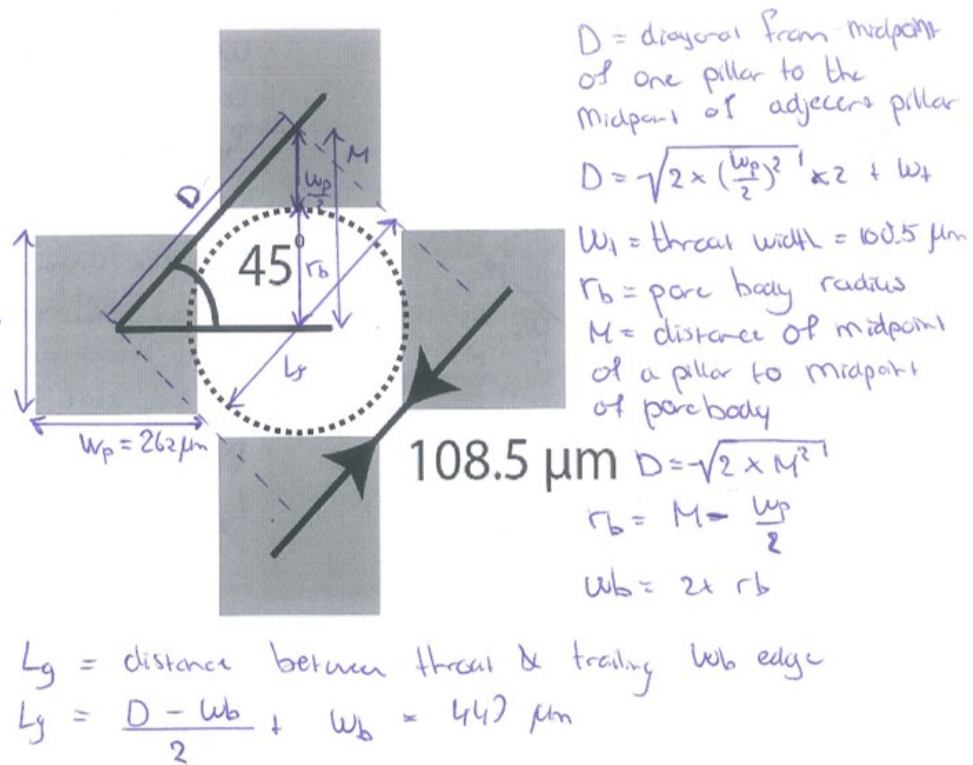


Figure B.2: Parameters of the Staggered Squares model.

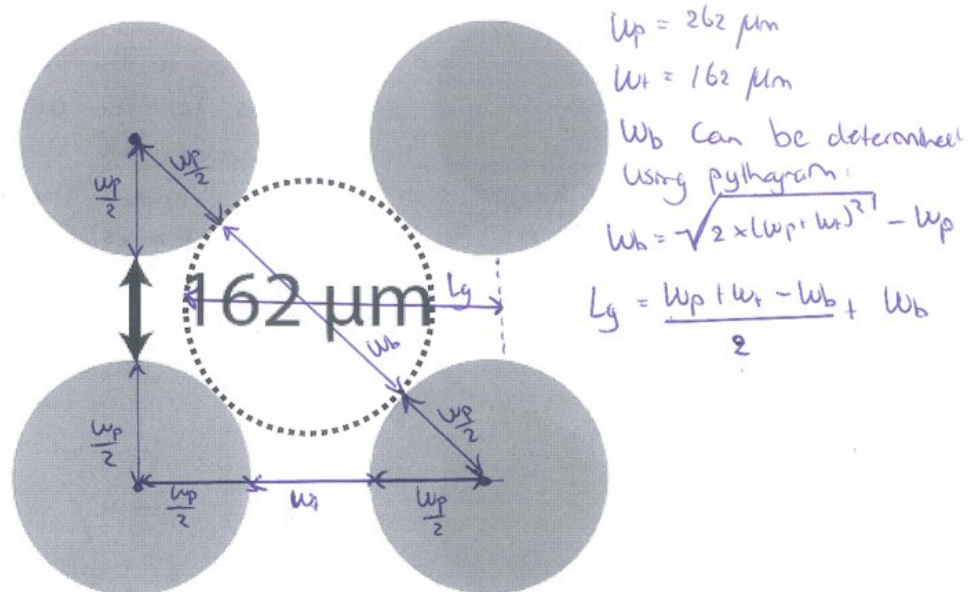


Figure B.3: Parameters of the Aligned Squares Model.

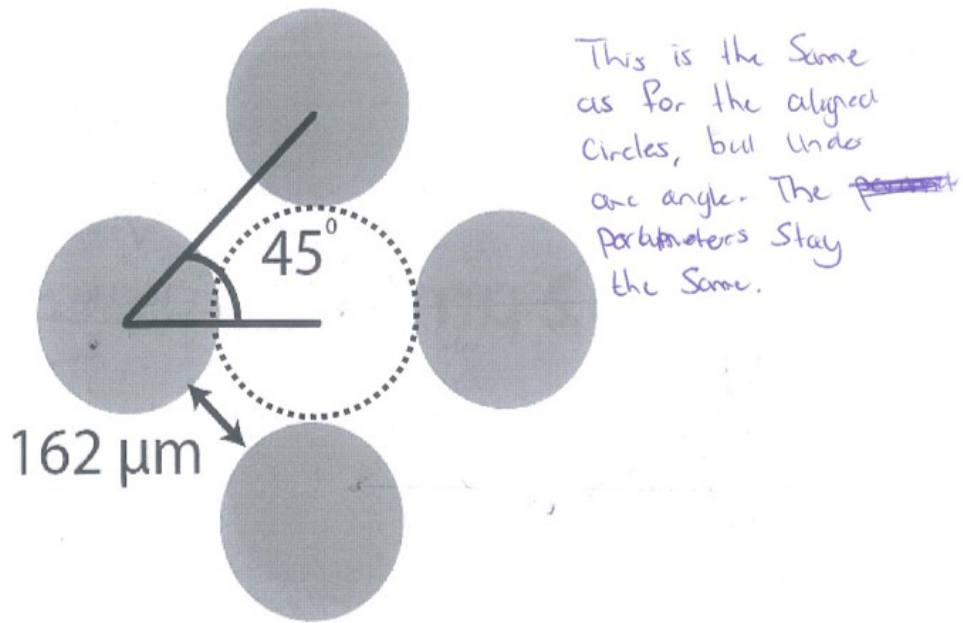


Figure B.4: Parameters of the Staggered Circles Model.

B.2. Hexagonal Geometry by Jones (2016)

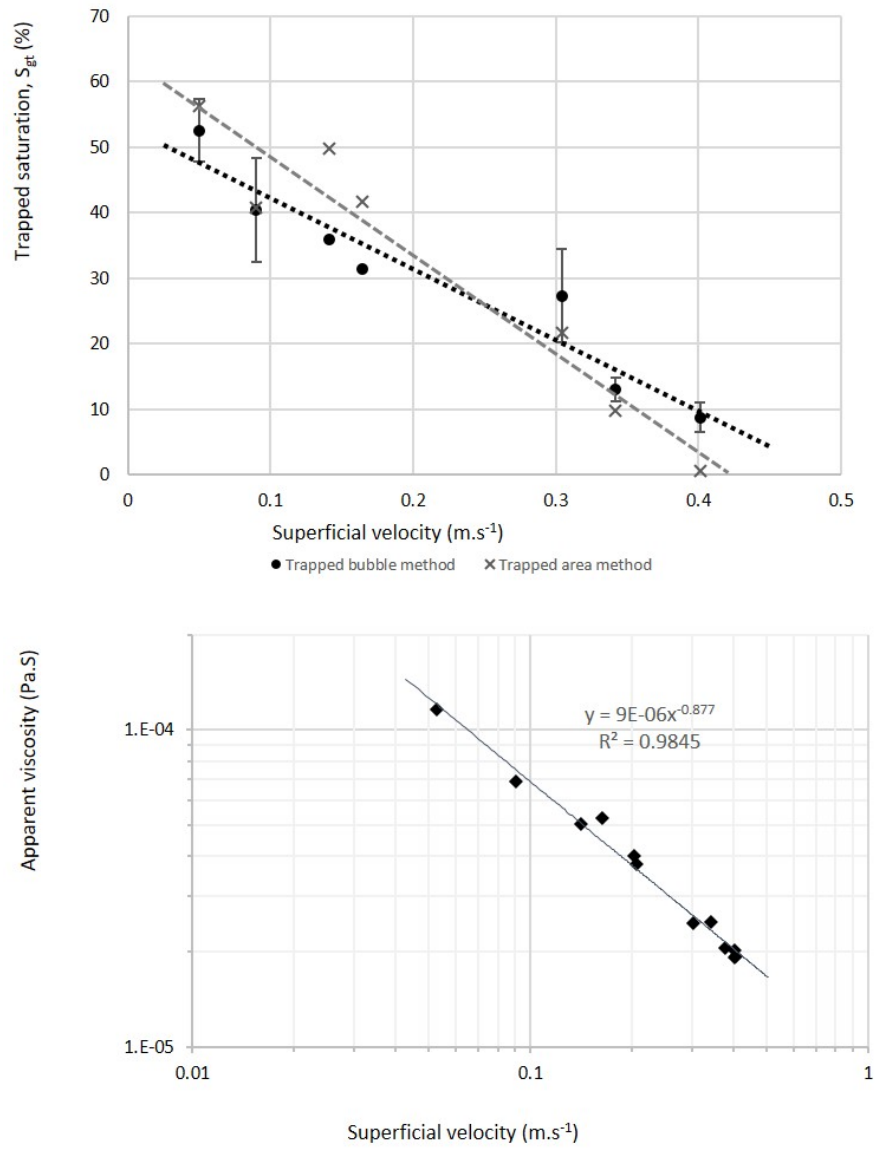


Figure B.5: Desaturation data by Jones *et al.* (2016). Above shows the measured desaturation, and below shows the viscosity as a function of the superficial velocity.

B.3. Micromodels of Jeong and Corapcioglu (2003)

The two figures below show the two figures used for analyzing the pore and throat widths of both models.

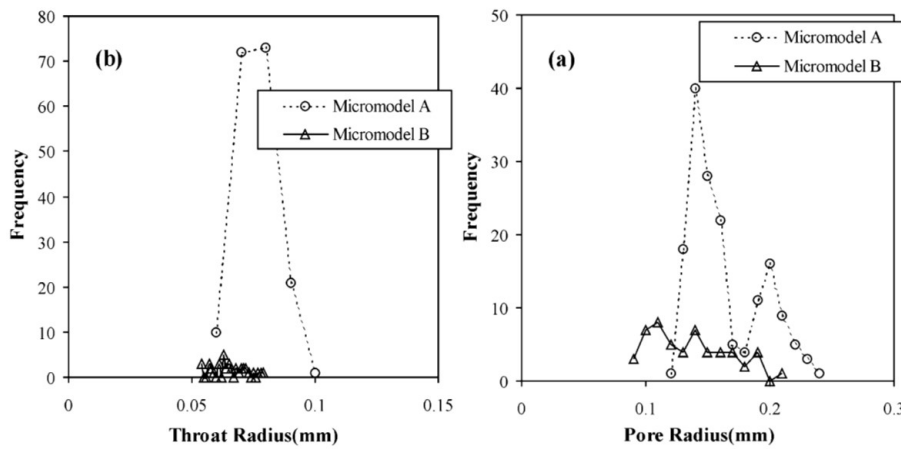


Figure B.6: Distribution graphs showing the pore throat and pore body sizes for the models provided by Jeong and Corapcioglu (2003)

The Desaturation curves presented by Jeong and Corapcioglu (2003). Note that the residual saturation is given as the ratio of the initial residual saturation after initial waterflooding.

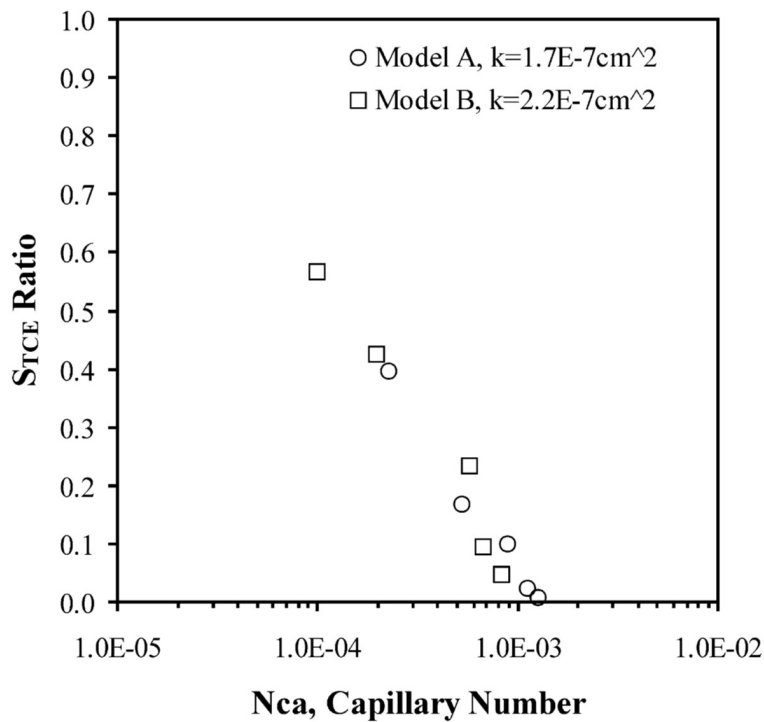


Figure B.7: Desaturation curves presented by Jeong and Corapcioglu (2003)

Table B.1: Desaturation data for the data of model A from Jeong and Corapcioglu (2003), both original and converted data for proper use.

∇P (Pa/m)	$N_{ca,c}$	$N_{ca,n}$	$S_{res}ratio$	S_{res}
44466	0.00024	1.183	0.4	0.128
94490	0.00051	2.515	0.17	0.0544
166747	0.0009	4.439	0.1	0.032
222329	0.0012	5.919	0.03	0.0096
259384	0.0014	6.906	0.01	0.0032

Table B.2: Desaturation data for the data of model B from Jeong and Corapcioglu (2003), both original and converted data for proper use.

∇P (Pa/m)	$N_{ca,c}$	$N_{ca,n}$	$S_{res}ratio$	S_{res}
13998	0.0001	0.270902193	0.57	0.3021
27997	0.0002	0.541804387	0.42	0.2226
82591	0.00059	1.59832294	0.24	0.1272
95190	0.00068	1.842134914	0.1	0.053
118987	0.00085	2.302668643	0.05	0.0265

B.4. Ibrahim et al. (2008)

These are the table and figures used to determine the parameters w_t and w_b for the model SRC-1 provided by Ibrahim *et al.* (2008). The measurements were done on a print out. The scale to convert the measured body and throat widths to real widths can be found in equation ??.

Table B.3: Measurements for the pore body sizes of the model SRC-1 by Ibrahim *et al.* (2008)

#	width (cm)	height (cm)	min (cm)	true (μm)
1	4.2	4.5	4.2	245.8
2	3.2	3.3	3.2	187.5
3	-	4.5	4.5	263.3
4	3.2	3.3	3.2	187.5
5	4.1	4.0	4.0	234.2
6	3.3	3.0	3.0	175.8
7	3.3	3.1	3.1	181.7
8	2.8	3.1	2.80	164.2
9	-	3.5	3.5	205.0
10	4.4	-	4.4	257.5

Table B.4: Measurements for the pore throat sizes of the model SRC-1 by Ibrahim *et al.* (2008)

#	measurement (cm)	true (μm)
1	0.8	47.5
2	1.4	82.5
3	1.4	82.5
4	0.9	53.3
5	0.7	41.7
6	1.7	100
7	1.1	65.0
8	1.0	59.2
9	0.9	53.3
10	0.9	53.3
11	1.2	70.8
12	0.5	30.0
13	1.3	76.7
14	1.2	70.8
15	1.2	70.8
16	1.0	59.2

Table B.5: Ganglion length measurements for the model by Ibrahim *et al.* (2008).

#	measurement (cm)	true (μm)
1	5.0	290.2
2	4.7	276.2
3	4.2	243.5
4	4.9	285.5
5	4.1	238.8
6	4.9	285.5
7	3.6	210.8
8	5.2	304.2
9	5.0	290.2
10	3.6	210.8

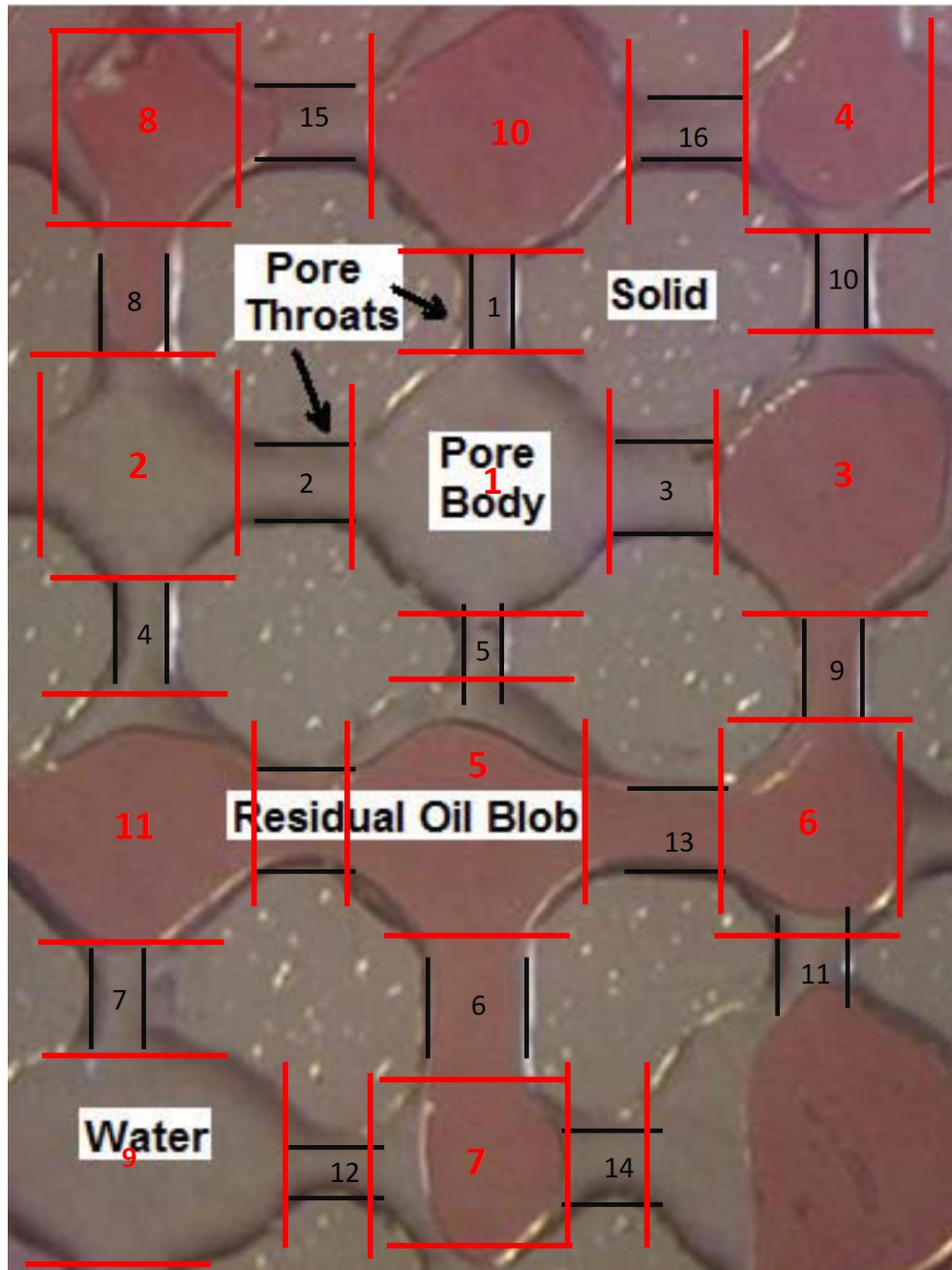


Figure B.8: Model of the measurements of the sizes of the throats and bodies.

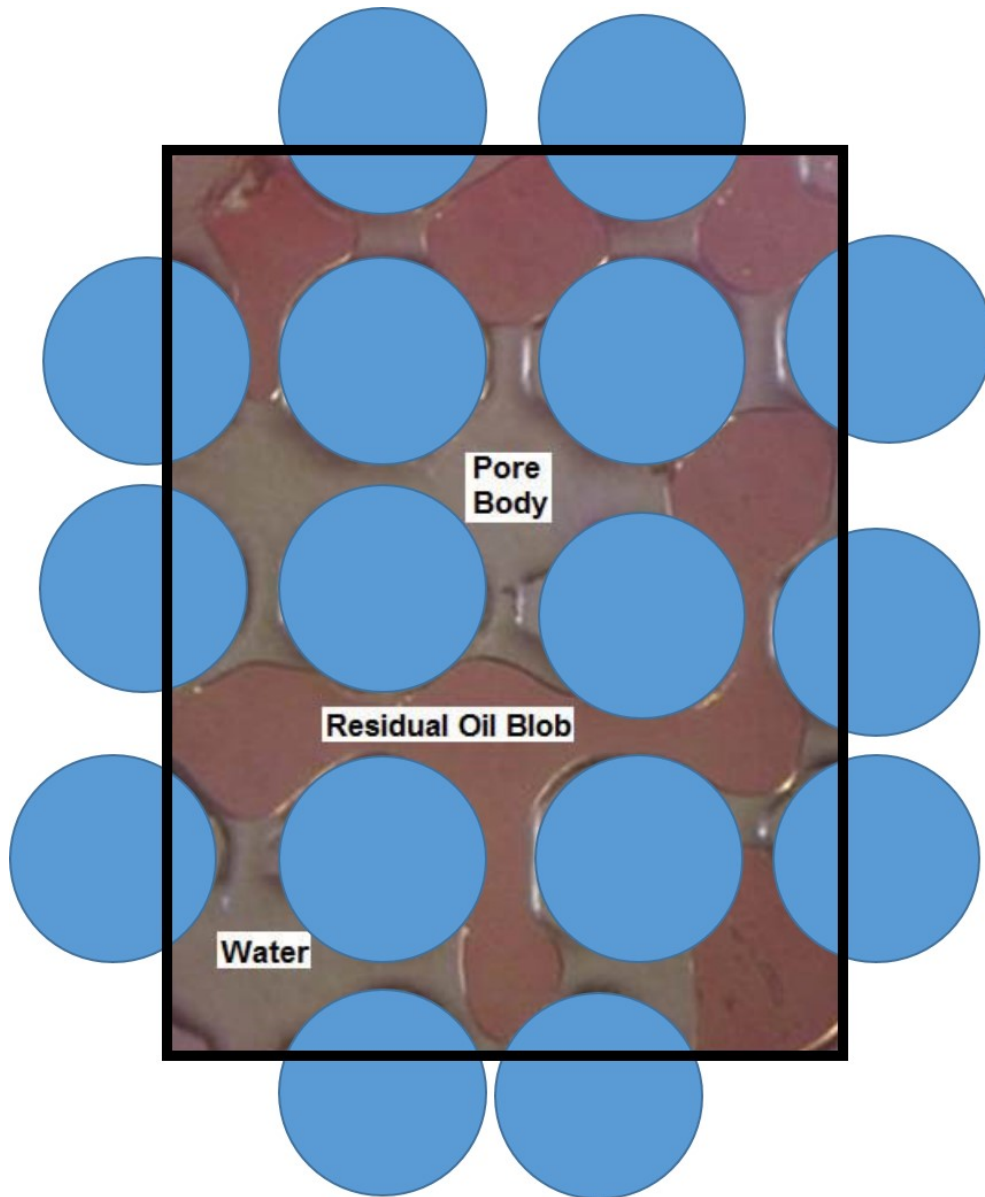


Figure B.9: Image used for determining the porosity of the model.

B.5. Yeganeh et al. (2016)

This appendix contains the additional figures used for analyzing the micromodel provided by Yeganeh *et al.* (2016). The capillary number given is the capillary number as defined in Yeganeh *et al.* (2016). See equation 6.9. Also, the table presents the desaturation data for each of the three definitions of the capillary number.

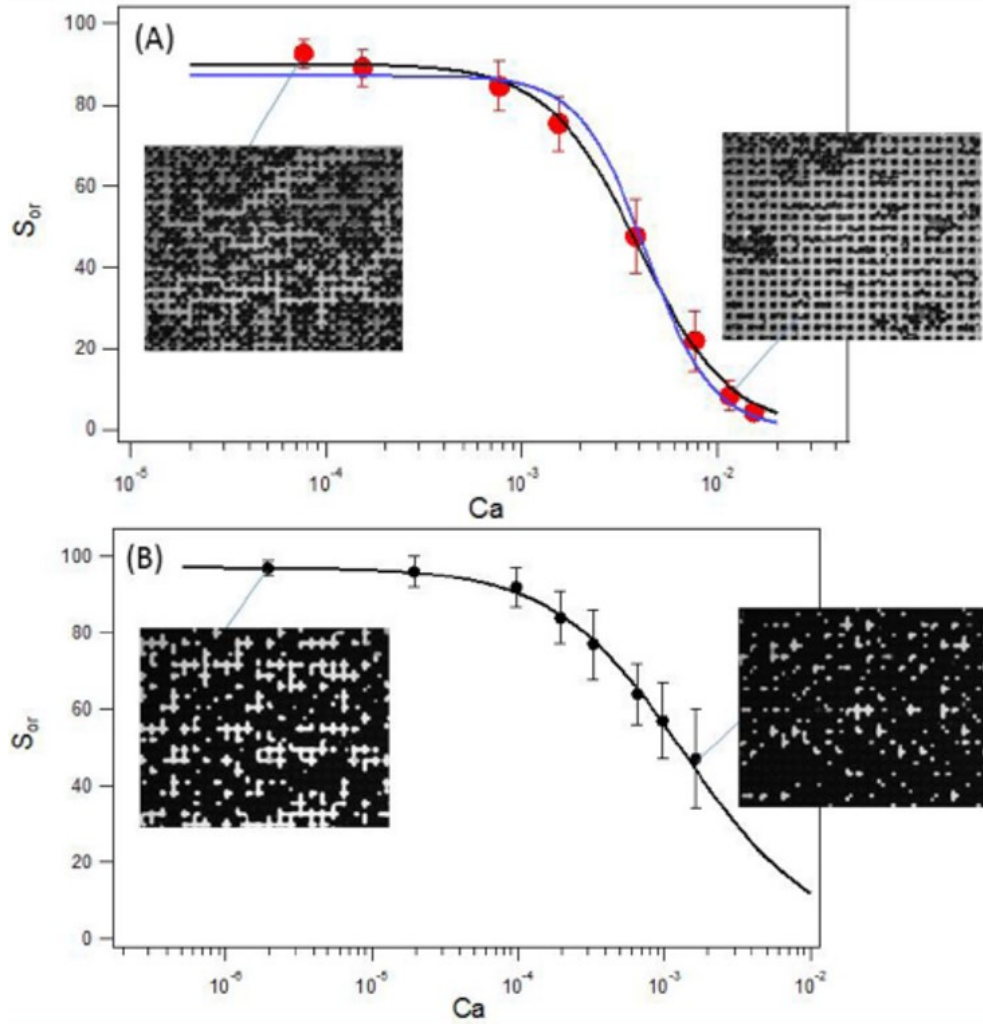


Figure B.10: Capillary Desaturation Curves for the two experiments carried out by Yeganeh *et al.* (2016). The top model is for experiment 1 (hexadecane/water). The bottom figure is for experiment 2 (crude oil/water).

C

Additional Figures for the Analysis of the Microfluidic Data

C.1. Pressure gradient and Residual Saturation

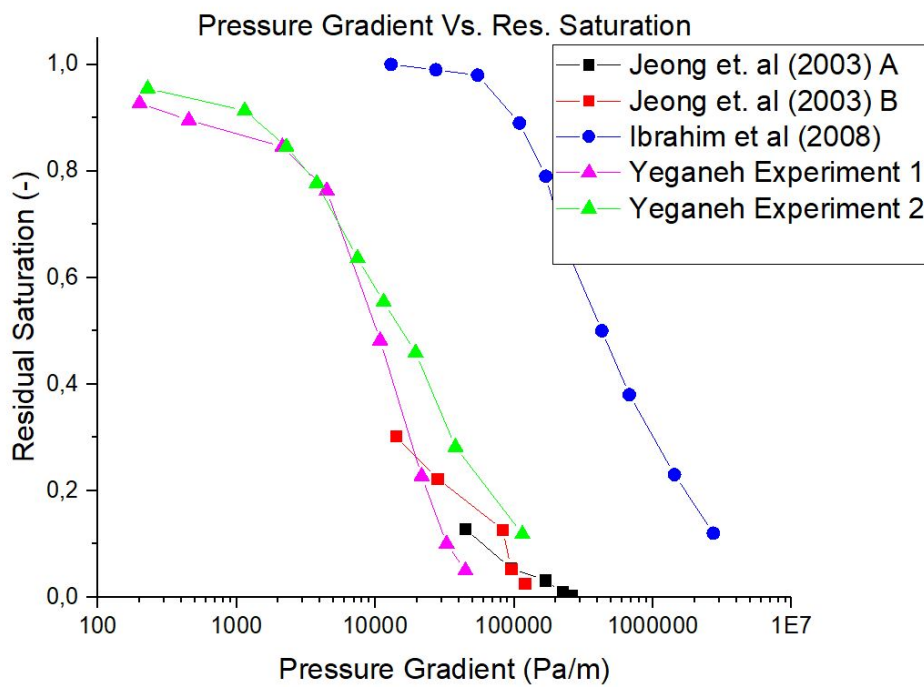


Figure C.1: Pressure gradient and residual saturation data for the models by (Jeong and Corapcioglu, 2003; Ibrahim *et al.*, 2008).

C.2. Changing Contact Angle Between Crude Oil and Brine

The following figures show how the capillary desaturation curves change, and come closer together if the contact angle between the crude oil and the brine increases.

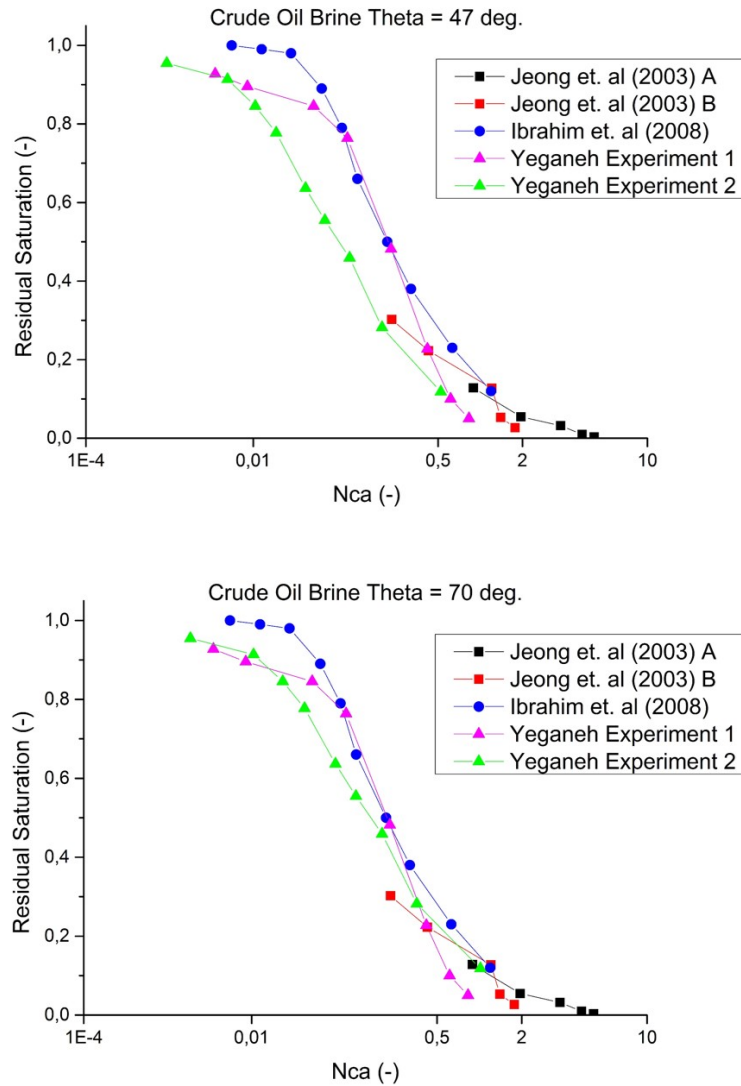


Figure C.2: Capillary Desaturation curves for Yeganeh Experiment 2 if the contact angle between the Brine and the Crude oil is increased from 47 to 70 degrees.

C.3. Permeability and Geometric Terms

The following plot shows the geometric term of each of the models against the pressure gradient. As can be seen, there is a trend that shows that higher permeabilities tend to have lower geometric terms.

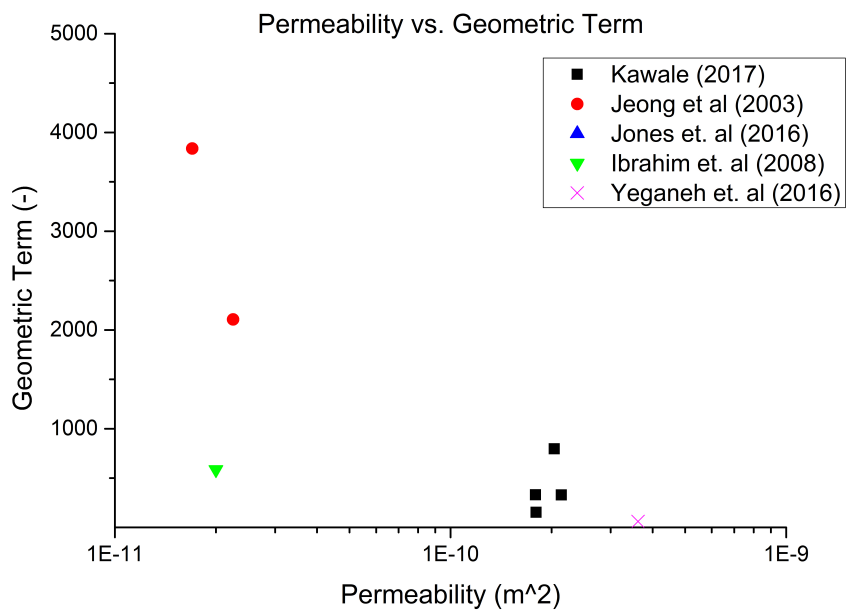


Figure C.3: The geometric terms plotted against the permeability for the 9 analyzed models.